

**STUDY OF NOVEL REDOX FLOW BATTERIES BASED ON
DOUBLE-MEMBRANE, SINGLE-MEMBRANE, AND MEMBRANE-LESS
CELL CONFIGURATIONS**

by

Ke Gong

A dissertation submitted to the Faculty of the University of Delaware in partial fulfillment of the requirements for the degree of Doctor of Philosophy in Chemical Engineering

Winter 2016

© 2016 Ke Gong
All Rights Reserved

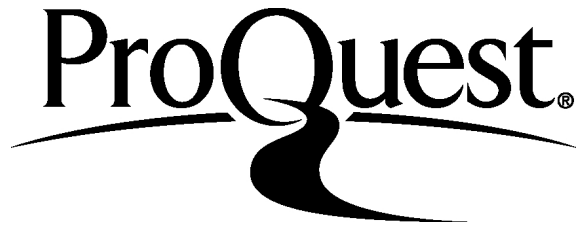
ProQuest Number: 10055795

All rights reserved

INFORMATION TO ALL USERS

The quality of this reproduction is dependent upon the quality of the copy submitted.

In the unlikely event that the author did not send a complete manuscript and there are missing pages, these will be noted. Also, if material had to be removed, a note will indicate the deletion.



ProQuest 10055795

Published by ProQuest LLC (2016). Copyright of the Dissertation is held by the Author.

All rights reserved.

This work is protected against unauthorized copying under Title 17, United States Code
Microform Edition © ProQuest LLC.

ProQuest LLC.
789 East Eisenhower Parkway
P.O. Box 1346
Ann Arbor, MI 48106 - 1346

**STUDY OF NOVEL REDOX FLOW BATTERIES BASED ON
DOUBLE-MEMBRANE, SINGLE-MEMBRANE, AND MEMBRANE-LESS
CELL CONFIGURATIONS**

by

Ke Gong

Approved: _____
Abraham M. Lenhoff, Ph.D.
Chair of the Department of Chemical and Biomolecular Engineering

Approved: _____
Babatunde A. Ogunnaike, Ph.D.
Dean of the College of Engineering

Approved: _____
Ann L. Ardis, Ph.D.
Interim Vice Provost for Graduate and Professional Education

I certify that I have read this dissertation and that in my opinion it meets the academic and professional standard required by the University as a dissertation for the degree of Doctor of Philosophy.

Signed:

Yushan Yan, Ph.D.
Professor in charge of dissertation

I certify that I have read this dissertation and that in my opinion it meets the academic and professional standard required by the University as a dissertation for the degree of Doctor of Philosophy.

Signed:

Feng Jiao, Ph.D.
Member of dissertation committee

I certify that I have read this dissertation and that in my opinion it meets the academic and professional standard required by the University as a dissertation for the degree of Doctor of Philosophy.

Signed:

Raul F. Lobo, Ph.D.
Member of dissertation committee

I certify that I have read this dissertation and that in my opinion it meets the academic and professional standard required by the University as a dissertation for the degree of Doctor of Philosophy.

Signed:

Ajay K. Prasad, Ph.D.
Member of dissertation committee

ACKNOWLEDGMENTS

I would like to express my deepest gratitude to my adviser, Dr. Yushan Yan, without whom this dissertation would never have been possible. He has set a great model to me with his diligence to work, passion to science, and open-mindedness to people. I'll always remember the first time I met Dr. Yan, when he shared his philosophy and perspective of research and PhD degree to me — the acronym “VISA to PhD”. Already impressing me then, this teaching has struck me more and more deeply over the past several years, in a way that I regarded it as not only a visa to scientific research, but also a ticket to successful career and positive and meaningful life. I thank Dr. Yan for the excellent guidance, continuous caring and firm support. The past four years are the most enjoyable time to me as a student.

I am also very grateful to Dr. Shuang Gu, as my adviser, mentor and friend, for his advice on research, help in life and willingness to share his experience and professional knowledge with me. My PhD work would be much more circuitous without his insightful suggestions and direction.

I would also like to thank Dr. Feng Jiao, Dr. Raul Lobo, and Dr. Ajay Prasad, for being on my dissertation committee and providing me with useful feedback on my research.

I thank my lab members, research colleagues, and roommates, for their company in my study, and encouragement and useful discussions on research in my journey of graduate student. My graduate life would be much less rich and colorful without them. In particular, I would like to thank my group fellows: Jianyu Cao,

Marco Dunwell, Qianrong Fang, Minrui Gao, Hongxia Guo, Stephen Giles, Jun Jiang, Robert Kaspar, Yancai Li, Mingchuan Luo, Xiaoya Ma, Wenchao Sheng, Andrew Tibbits, Junhua Wang, Hao Wang, Yan Wang, Jared Nash, Jarrid Wittkopf, Mariah Woodroof, Bingzi Zhang, Yanqi Zhang, Yun Zhao, Jie Zheng, Shuyuan Zhou, and Zhongbin Zhuang. I thank the undergraduate students who worked with me, Kevin Kuttler, Jonathan Grunewald, Kelsey Yeager, Fei Xu, Michael Lehrich, for their diligence and hard work on the research.

I would like to thank my family members, who have always unwaveringly supported me, and patiently listened to my complaints of failed experiments and research hardships. Encouragement from them has continuously been the greatest power to make me progress.

I would like to acknowledge the Advanced Research Projects Agency - Energy (ARPA-E) of the Department of Energy for funding support, and the Royal Society of Chemistry for permitting the reprint of the following publications for this dissertation.

- K. Gong, Q. Fang, S. Gu, S. F. Y. Li, and Y. S. Yan, *Energy & Environmental Science*, **2015**, DOI: 10.1039/C5EE02341F
- K. Gong, X. Ma, K. M. Conforti, K. J. Kuttler, J. B. Grunewald, K. L. Yeager, M. Z. Bazant, S. Gu, and Y. S. Yan, *Energy & Environmental Science*, **2015**, DOI: 10.1039/C5EE02315G
- S. Gu, K. Gong, E. Z. Yan and Y. S. Yan, *Energy & Environmental Science*, **2014**, 7, 2986-2998

TABLE OF CONTENTS

LIST OF TABLES	ix
LIST OF FIGURES	xi
ABSTRACT	xx

Chapter

1	INTRODUCTION	1
1.1	Energy Storage System and Redox Flow Battery	1
1.2	Aqueous Redox Flow Batteries	5
1.2.1	Chromium-Iron RFB	9
1.2.2	Zinc-Bromine RFB	10
1.2.3	Sulfur-Bromine RFB	11
1.2.4	All-Vanadium RFB	12
1.3	Nonaqueous Redox Flow Batteries	14
1.3.1	Metal-based Redox Pairs	15
1.3.2	Metal-free Redox Pairs	18
1.4	Challenges for State-of-the-art RFBs	22
1.5	Outline of Dissertation	26
2	DOUBLE ION-EXCHANGE MEMBRANE DESIGN FOR REDOX FLOW BATTERIES	28
2.1	Introduction	28
2.2	Working Principle of Multiple-membrane RFB	30
2.3	Zinc-Cerium RFB	33
2.3.1	Experiment and Method	35
2.3.2	Result and Discussion	37
2.3.3	Summary of Zn-Ce RFB	40
2.4	Sulfur-Iron RFB	41
2.4.1	Experiment and Method	43

2.4.2	Result and Discussion.....	44
2.4.3	Summary of S-Fe RFB	48
2.5	Zinc-Iron RFB	48
2.5.1	Experiment and Method	50
2.5.2	Result and Discussion.....	53
2.5.3	Summary of Zn-Fe RFB	66
2.6	Remaining Challenge — Crossover of Acid and Base	67
2.6.1	Experiment and Methods.....	67
2.6.2	Results and Discussion	71
2.6.2.1	Permeation Coefficient of H ⁺ Through AEMs.....	71
2.6.2.2	Permeation Coefficient of OH ⁻ Through CEMs.....	73
2.7	Concluding Remarks	75
3	AN ALL-SOLUBLE ALL-IRON RFB BASED ON COORDINATION CHEMISTRY OF IRON	77
3.1	Introduction	77
3.2	Experiment and Method	81
3.3	Results and Discussion	85
3.3.1	Redox Electrochemistry	85
3.3.2	Cell Performance and Preliminary Durability.....	88
3.4	Challenges	91
3.4.1	Relatively Low Coulombic Efficiency	91
3.4.2	High Cell Resistance	102
3.5	Concluding Remarks	103
4	A MEMBRANE-LESS ZINC-FERROCENE REDOX FLOW BATTERY BASED ON IMMISCIBLE ORGANIC-INORGANIC ELECTROLYTES .	105
4.1	Introduction	105
4.2	Experiment and Method	108
4.3	Results and Discussion	109
4.4	Concluding Remarks	115
5	CONCLUSIONS AND PERSPECTIVES	116

5.1	Summary of Conclusions	116
5.2	Perspectives and Future Work.....	120
REFERENCES		122
Appendix		
A	CALCULATION METHODS	138
	A.1 Theoretical calculation of R_{cp}	138
	A.2 Development of cost model.....	141
B	SUPPLEMENTARY TABLES.....	144
C	REPRINT PERMISSIONS	147

LIST OF TABLES

Table 1.1	Anion-based, cation-based and anion-cation hybrid redox pairs in RFBs.....	7
Table 1.2	Metal-based redox pairs proposed in nonaqueous RFBs	20
Table 1.3	Metal-free redox pairs proposed in nonaqueous RFBs	22
Table 2.1	Parameters used to calculate t_{lifetime} for Zn-Fe RFB.....	70
Table 2.2	Thickness, permeation coefficient, conductivity, σ/P and t_{lifetime} of different AEMs.....	73
Table 2.3	Thickness, permeation coefficient, conductivity, σ/P and t_{lifetime} of different CEMs.....	74
Table 3.1	Electrode potentials, kinetic constants and pHs of test conditions of iron(III)/iron(II)-ligand redox pairs.....	80
Table 3.2	Diffusion coefficients of $[\text{Fe}(\text{TEOA})\text{OH}]^-$ (D_{O}), $[\text{Fe}(\text{TEOA})\text{OH}]^{2-}$ (D_{R}), and standard rate constant (k^0) of the $[\text{Fe}(\text{TEOA})\text{OH}]^-/[\text{Fe}(\text{TEOA})\text{OH}]^{2-}$ redox pair.....	87
Table 3.3	Diffusion coefficients of $\text{Fe}(\text{CN})_6^{3-}$ (D_{O}), $[\text{Fe}(\text{CN})_6]^{4-}$ (D_{R}), and standard rate constant (k^0) of the $\text{Fe}(\text{CN})_6^{3-}/\text{Fe}(\text{CN})_6^{4-}$ redox pair.....	88
Table 3.4	Permeation coefficient of $[\text{Fe}(\text{TEOA})\text{OH}]^-$, $[\text{Fe}(\text{TEOA})\text{OH}]^{2-}$, and free TEOA.....	97
Table 4.1	Diffusion coefficients of ferrocenium (D_{O}) and ferrocene (D_{R}), and the kinetic constant (k^0) of Fc^+/Fc redox pair. The kinetic constant is calculated based on the method of Nicholson ^[175]	112
Table B1	Results of electrolyte cost for both Zn-Fe RFB and all-V RFB.....	144
Table B2	Results of stack cost for both Zn-Fe RFB and all-V RFB.....	144
Table B3	Prices of redox compounds	144

Table B4	Prices of supporting salt/acid/base	145
Table B5	Prices of electrode materials.....	145
Table B6	Prices of membrane materials	146
Table B7	Prices of other materials/handling	146

LIST OF FIGURES

Figure 1.1	A typical redox flow battery structure: the Cr-Fe redox flow battery, the first redox flow battery, developed in 1974.....	4
Figure 1.2	Redox pairs used in aqueous RFBs classified as cation and anion redox pairs, and RFBs built based on different redox pairs. The standard redox potentials of redox pairs are from the references in Table 1.1. The single-CEM cell is preferred for one anion-anion redox pair vs. another anion-anion redox pair (left region); the single-AEM cell is preferred for one cation-cation redox pair vs. another cation-cation redox pair (right region).	8
Figure 2.1	(a) Concept schematic. Double-IEM RFB. It consists of two types of IEMs (one CEM and one AEM) and three separate electrolytes (negative, middle, and positive). (b) Working principles of double-IEM RFB cell configuration. NE and PE represent the negative electrode and positive electrode, respectively. Combination of an anion-anion (negative) redox pair (A_N^-/A_N^{2-}) and a cation-cation (positive) redox pair (C_P^{2+}/C_P^+).....	32
Figure 2.2	Schematic of Zn-Ce RFB. The negative electrolyte is comprised of $Zn(OH)_4^{2-}/Zn$ as the negative redox pair and a NaOH solution; The middle electrolyte is a $NaClO_4$ solution; The positive electrolyte is comprised of Ce^{4+}/Ce^{3+} as the positive redox pair and an $HClO_4$ solution. A cation-exchange membrane (CEM) separates the negative electrolyte and middle electrolyte while an anion-exchange membrane (AEM) separates the middle electrolyte and positive electrolyte. The working principles are as follows. When the cell is being charged, $Zn(OH)_4^{2-}$ anions are reduced to form Zn metal deposits in the negative electrolyte, and Na^+ cations move from middle electrolyte, passing through the CEM, to the negative electrolyte. At the same time, Ce^{3+} cations are oxidized to form Ce^{4+} cations, and ClO_4^- anions move from the middle electrolyte, passing through AEM, to the positive electrolyte. As a result, the $NaClO_4$ concentration in the middle electrolyte decreases in the charging process. The discharging process is the reverse of the charging process.....	34

Figure 2.3	Cell configuration of Zn-Ce RFB. The electrolyte flow pathways are shown with red arrows. The electrolytes enter and exit the system through the side holes on the electrolyte frames (thick red arrows). Once into the electrolyte frames, the positive and negative electrolytes flow sideways and through the small holes on the electrolyte frame, conductor, and current collector into the chamber encompassed by gasket and membrane and then return to the electrolyte frames (thin red arrows). The middle electrolyte enters the middle electrolyte frame and then through the tiny hole on the recessed portion of the middle electrolyte frame (not shown in figure) into the open area in the middle electrolyte chamber defined by the two membranes. N, M, and P in parentheses stand for negative, middle, and positive, respectively.	36
Figure 2.4	(a) Open-circuit voltage (OCV) of Zn-Ce RFB at 90% State of charge (SOC). (b) A full charge-discharge test of Zn-Ce RFB at 20 mA/cm ² showed 96% coulombic efficiency, 86% voltage efficiency and 83% energy efficiency.	38
Figure 2.5	(a) 20-cycle test of Zn-Ce RFB at 20 mA/cm ² . (b) Coulombic efficiency (CE), voltage efficiency (VE) and energy efficiency (EE) for each cycle in 20-cycle test.	39
Figure 2.6	Weight remaining of three different AEMs after soaked in Ce(IV) solution (0.5 M Ce(ClO ₄) ₄ , 1 M HClO ₄). FAA-2 membrane broke into several pieces during the transfer of membrane and therefore its remaining weight might be inaccurate.	40
Figure 2.7	Schematic of S-Fe RFB. The negative electrolyte is comprised of S ₄ ²⁻ /S ₂ ²⁻ as the negative redox pair and a NaOH solution; The middle electrolyte is a NaCl solution; The positive electrolyte is comprised of Fe ³⁺ /Fe ²⁺ as the positive redox pair and an HCl solution. The cell configuration and working principle are similar to those of Zn-Ce RFB described in Figure 2.2.	42
Figure 2.8	(a) Open-circuit voltage (OCV) of S-Fe RFB at 70% State of Charge (SOC). (b) Charge-discharge test of S-Fe RFB with 70% SOC swing at different current densities.	45
Figure 2.9	(a) Polarization curve of the S-Fe RFB at 50% SOC. (b) Analysis of cell voltage loss during discharging process. The orange part represents voltage loss from ohmic resistance.	46

- Figure 2.10 (a) 100-cycle test of S-Fe RFB at 30 mA/cm². During the cycle process, certain amounts of acid and base was added into positive and negative electrolytes to sustain the appropriate pH for each electrolyte. (b) Coulombic efficiency (CE), voltage efficiency (VE) and energy efficiency (EE) for each cycle in 100-cycle test..... 47
- Figure 2.11 Schematic of the Zn-Fe RFB. The negative electrolyte is comprised of Zn(OH)₄²⁻/Zn as the negative redox pair and a NaOH solution; The middle electrolyte is a NaCl solution; The positive electrolyte is comprised of Fe³⁺/Fe²⁺ as the positive redox pair and an HCl solution. The cell configuration and working principle are similar to those of the Zn-Ce RFB described in Figure 2.2. 49
- Figure 2.12 Overpotential measured at the zinc electrode (copper mesh) and iron electrode (carbon felt). The charge/discharge electrode overpotential is smaller than 10 mV and 40 mV for Fe³⁺/Fe²⁺ redox pair (carbon felt electrode) and Zn(OH)₄²⁻/Zn redox pair (copper mesh electrode), respectively, at a current density of 200 mA/cm². Overpotential was measured in cell at 50% SOC..... 54
- Figure 2.13 Schematics of middle electrolyte in between two membranes (a) Schematic illustrating velocity, concentration, and potential profiles of middle electrolytes during charging process. Φ , C , V and δ_N represent potential, concentration, velocity and Nernstian boundary layer of electrolyte. (b) Schematic illustrating middle electrolyte and three key parameters (thickness, current density and flow rate) that influence the cell resistance. 56
- Figure 2.14 The impact of middle electrolyte (thickness and salt concentration) on ohmic resistance. (a) The NaCl concentration vs. ohmic resistance at a middle electrolyte thickness of 0.5 mm. The ohmic resistance firstly decreases with raising NaCl concentration (increasing ionic conductivity of middle electrolyte), and after reaching the minima around 2.5 mol/L it slowly increases with raising NaCl concentration (decreasing ionic conductivity of membranes). The water content in membrane decreases when in contact with highly concentrated salt solution, resulting in lowered ionic conductivity. (b) The thickness of middle electrolyte vs. ohmic resistance at a middle electrolyte NaCl concentration of 2.5 mol/L. Note: in both cases, a low current density of 10 mA/cm² and a high flow rate of 400 ml/min were used to minimize concentration polarization. 56

Figure 2.15	The impact of flow rate and current density on measured internal resistance at different middle electrolyte thicknesses. (a) $d_{\text{middle}} = 3.5$ mm. (b) $d_{\text{middle}} = 2.0$ mm. (c) $d_{\text{middle}} = 0.5$ mm.	57
Figure 2.16	Experimentally measured and theoretically calculated R_{cp} as a function of dimensionless number X . (a) Experimentally measured R_{cp} as a function of dimensionless number X and linear fitting on log-log scale. Linear fitting of $\log X$ vs. $\log R_{\text{cp}}$ shows a slope of -0.7 , <i>i.e.</i> , as $R_{\text{cp}} \propto X^{-0.7}$. (b) Theoretically calculated R_{cp} as a function of dimensionless number X . We calculated R_{cp} considering contributions from 1) the potential difference through the Nernst boundary layer in electrolyte adjacent to ion-exchange membrane and 2) the potential difference from the Donnan equilibrium across ion-exchange membranes (detailed in Appendix A, Calculation Method). (c). Comparison between theoretically calculated R_{cp} (empty symbols) and experimentally measured R_{cp} (filled symbols) with respect with the dimensionless number X	59
Figure 2.17	Cell performance and cycle test. (a) Discharge polarization curve of Zn-Fe RFB at 70% SOC. (b) Charge-discharge test with a 75% SOC swing at 50, 100, and 150 mA/cm ² current density. (c) 20-cycle test voltage curve at 80 mA/cm ² with a 75% SOC swing. (d) Coulombic efficiency (CE), voltage efficiency (VE) and capacity of each cycle.	61
Figure 2.18	Validation of electrochemical model for Zn-Fe RFB. (a) Charge and discharge curves at current density of 50 mA/cm ² . (b) Polarization and power curves at a SOC of 50%. Note: the polarization curve was obtained by using Nafion 212 and FAA membranes which have larger resistances compared with Nafion 211 and Tokuyama A901.	62
Figure 2.19	Zn-Fe RFB cost analysis and comparison with other notable RFBs.....	63
Figure 2.20	Capital cost and round-trip efficiency of the whole system. (a) Power capital cost (mostly from stack cost). (b) Energy capital cost (mostly from electrolyte cost). (c) Round-trip efficiency of the whole system. ..	65
Figure 2.21	System capital cost of a 1 MW Zn-Fe RFB system as a function of discharge duration at a current density of 80 mA/cm ²	66

Figure 2.22	(a) Crossover measurement of H^+ across the FAA, PTFE-PPO, PPO and FAB membranes. The slope obtained from linear fitting of $\ln[C_A/(C_A-C_B)]$ vs. time is used to calculate the permeation coefficient. (b) Position of different AEMs in terms of conductivity of the balancing ion and $1/\text{permeation coefficient of the proton}$. The contour lines of 10, 100 and 1000 h lifetimes are shown as red, blue, and green lines, respectively. Positions closer to the upper righthand corner represent longer lifetimes.	72
Figure 2.23	(a) Crossover measurement of OH^- across the Nafion 212, FKS, and FKE membranes. The slope obtained from linear fitting of $\ln[C_A/(C_A-C_B)]$ vs. time is used to calculate permeation coefficient. (b) Position of different CEMs in terms of their conductivity of balancing ion and $1/\text{permeation coefficient of hydroxide ion}$. The contour lines of 100, 1000 and 5000 h lifetimes are shown in red, blue and green lines, respectively. Positions closer to the upper right corner represent longer lifetimes.	74
Figure 3.1	Redox pairs of iron complexes that have been tested for RFB applications. Each redox pair is represented by its formal potential vs. standard hydrogen electrode (SHE) potential at the corresponding pH of its test conditions. The full names of any abbreviations are listed in Table 3.1. The highlighted $[Fe(TEOA)OH]^- / Fe(TEOA)(OH)]^{2-}$ and $Fe(CN)_6^{3-} / Fe(CN)_6^{4-}$ redox pairs constitute the all-Fe RFB in this work.	79
Figure 3.2	Cell configuration for the all-Fe RFB. The electrolyte flows into the system through the side inlet of electrolyte frame. The positive and negative electrolytes flow through the small holes on electrolyte frame, conductor, and current collector into the chamber encompassed by gasket and membrane.	83
Figure 3.3	Cyclic voltammetry of $[Fe(TEOA)OH]^- / [Fe(TEOA)OH]^{2-}$ and $Fe(CN)_6^{3-} / Fe(CN)_6^{4-}$ in sodium hydroxide solution. The Fe-TEOA solution contains 0.2 M $FeCl_2$, 0.2 M $FeCl_3$, 2 M TEOA and 3 M NaOH. The Fe-CN solution contains 0.2 M $Na_4Fe(CN)_6$, 0.2 M $Na_3Fe(CN)_6$ and 3 M NaOH. The working electrode is glassy carbon and scan rate is 40 mV/s for both cases.	86

Figure 3.4	(a) Cyclic voltammetry of $[\text{Fe}(\text{TEOA})\text{OH}]^-/[\text{Fe}(\text{TEOA})\text{OH}]^{2-}$ at different scan rates on glassy carbon electrode. The electrolyte contains 0.2 M FeCl_2 , 0.2 M FeCl_3 , 2 M TEOA and 3 M NaOH. (b) Cyclic voltammetry of $\text{Fe}(\text{CN})_6^{4-}/\text{Fe}(\text{CN})_6^{3-}$ at different scan rates on glassy carbon electrode. The electrolyte contains 0.1 M $\text{Na}_4\text{Fe}(\text{CN})_6$, 0.1 M $\text{K}_3\text{Fe}(\text{CN})_6$, and 3 M NaOH.	87
Figure 3.5	Cell voltage curve of a charge-discharge test of the all-Fe RFB at 40 mA/cm^2	89
Figure 3.6	Polarization curve of the all-Fe RFB at 70% state of charge (SOC) with peak power density at 160 mW/cm^2 . The polarization curve shows strong ohmic relationship between voltage and current density, indicating the system is limited by internal resistance.	90
Figure 3.7	(a) Cell voltage of 110-cycle test of the all-Fe RFB at 40 mA/cm^2 . (b) Coulombic efficiency (CE), voltage efficiency (VE), energy efficiency (EE) and discharge capacity of each cycle in the same 110-cycle test of the all-Fe RFB.	91
Figure 3.8	(a) Cell voltage curve of a charge-discharge test of all-Fe RFB at 40 mA/cm^2 , and (b) zoomed-in cell voltage, positive and negative potential vs. Ag/AgCl reference electrode during the end of the discharge process, as indicated in the green rectangle in Figure 3.8 (a). The decrease of positive potential indicates the positive side is the dominating cause for the cell voltage drop and therefore the coulombic efficiency loss.....	92
Figure 3.9	Cell voltage curve of the Fe-CN symmetrical cell. CE remains at 100%, indicating no oxygen evolution side reaction or crossover.....	93
Figure 3.10	^{13}C NMR spectra of positive (a) and negative (b) electrolytes before and after cycle testing of an all-soluble all-Fe RFB. A number of new peaks showed up in the positive electrolyte after 20 cycles, as enclosed in the red circle, whereas no new peaks were observed for negative electrolyte after testing.....	94
Figure 3.11	^{13}C NMR spectra of electrolyte of the deficient side of a permeation cell with the enriched side being (a) $\text{Fe}(\text{CN})_6^{4-}$ and (b) $\text{Fe}(\text{CN})_6^{3-}$. No $\text{Fe}(\text{CN})_6^{4-}$ or $\text{Fe}(\text{CN})_6^{3-}$ was detected over five days. No peaks were detected during 5 days of testing. Since the lowest possible concentration that could be detected by NMR spectroscopy is 0.01 M, the permeation coefficient was then estimated to less than $1 \times 10^{-11} \text{ cm}^2/\text{s}$, by assuming the concentration after 5-day test is below 0.01 M.	95

- Figure 3.12 ^{13}C NMR spectra of electrolyte of the deficient side of a permeation cell with the enriched side being (a) $[\text{Fe}(\text{TEOA})(\text{OH})]^{2-}$ and (b) $[\text{Fe}(\text{TEOA})(\text{OH})]^-$. The concentration of TEOA is converted by comparing the peak integral with that of the spectrum of standard TEOA solution, having known TEOA concentration. (c) Linear fitting of total TEOA and $[\text{Fe}(\text{TEOA})(\text{OH})]^{2-}$ concentration vs. test time. (d) Linear fitting of total TEOA and $[\text{Fe}(\text{TEOA})(\text{OH})]^-$ concentration vs. test time. 97
- Figure 3.13 (a) CV scan on glassy carbon electrode at 5 mV/s from 0 V to 0.5 V vs. Ag/AgCl of 0.01 M $\text{Na}_4\text{Fe}(\text{CN})_6$ (blue curve), 0.2 M TEOA (green curve), 0.01 M $\text{Na}_4\text{Fe}(\text{CN})_6$ and 0.2 M TEOA (red curve). All electrolytes are supported with 1 M NaOH. The rising current at $E_w > 0.4$ V vs. Ag/AgCl confirms the electrochemical oxidation of TEOA on electrode surface (green curve). (b) CV scan of on glassy carbon electrode at 5 mV/s from 0 to 0.5 V vs. Ag/AgCl of 0.01 M $\text{Na}_4\text{Fe}(\text{CN})_6$ with different TEOA concentrations from 0.1 M to 0.6 M. The current density at 0.4 V vs. Ag/AgCl of forward scan was chosen as limiting current density. Inset: linear fitting of limiting current density vs. TEOA concentration. 99
- Figure 3.14 (a) ^1H NMR spectra of solutions containing 0.5 M $\text{K}_3\text{Fe}(\text{CN})_6$, 0.2 M TEOA and 0.5 M KOH with test time. Inset: zoomed-in figure of ^1H NMR between chemical shifts of 4.0 and 3.2 ppm. Peaks a and b are attributed to α and β hydrogen in TEOA. Peaks c, d and e are possibly due to the oxidation at α -carbon and the formation of 1-(bis(2-hydroxyethyl)amino)ethane-1,2-diol and 2-hydroxy-N,N-bis(2-hydroxyethyl)acetamide. (b) Predicted ^1H NMR spectrum of 1-(bis(2-hydroxyethyl)amino)ethane-1,2-diol (upper) and 2-hydroxy-N,N-bis(2-hydroxyethyl)acetamide (lower). It is possible that the oxidation takes place at α -carbon and generates 1-(bis(2-hydroxyethyl)amino)ethane-1,2-diol. Diol can be further oxidized by $\text{Fe}(\text{CN})_6^{3-}$ and produces 2-hydroxy-N,N-bis(2-hydroxyethyl)acetamide. The shape and relative peak position of the obtained degradation product matches the predictions for the proposed product. 101
- Figure 3.15 (a) Impedance of all-Fe RFB showing ohmic resistance (R_{ohm} , depicted in blue color) and charge transfer resistance (R_c , red). The ohmic resistance accounts for the major part of total resistance. (b) Experimental (solid) and predicted iR -free (dashed) polarization curve of all-Fe RFB at 70% State of Charge (SOC). 103

Figure 3.16	Impedance test of a symmetrical cell with three different electrolytes: 3 M NaOH (dark blue), 2 M TEOA in 3 M NaOH (blue), and 0.4 M FeCl ₃ , 2 M TEOA in 3 M NaOH(green).....	103
Figure 4.1	(a) Schematic of a membrane-less RFB based on immiscible organic-inorganic electrolytes. (b) Design of the membrane-less zinc-ferrocene RFB.	108
Figure 4.2	(a) Schematic of a cylindrical cell=. From top to bottom: PTFE block, gold plate electrode, copper plate electrode, EPDM rubber gasket, polypropylene cylinder, EPDM rubber gasket, carbon foam electrode, fluorosilicone rubber gasket, carbon paper electrode, carbon block, gold plate electrode, and PTFE block. (b) Schematic of an assembled cylindrical cell.	109
Figure 4.3	(a). Solubility of ferrocene along with mole percentage of butyl acetate in organic electrolyte. (b). Conductivity of organic electrolyte versus mole ratio of butyl acetate.....	111
Figure 4.4	(a) Cyclic voltammogram of blank electrolyte (70 mol% Butyl Acetate, 30 mol% Aliquat [®] 336) and ferrocene solution (0.05 M Fc in 70 mol% Butyl Acetate, 30 mol% Aliquat [®] 336) on a glassy carbon electrode. (b) CV of ferrocene electrolyte (0.05 M Fc, 0.05 M FcBF ₄ in 70 mol% Butyl Acetate, 30 mol% Aliquat [®] 336) at different scan rates on glassy carbon electrode.	112
Figure 4.5	(a) A 20-cycle test of Zn-Fc membrane-less RFB. The cut-off voltage was set at 1.35 V for charge and 0 V for discharge. (b) Coulombic, voltage, and energy efficiencies and capacity for each cycle in 20-cycle test.	113
Figure 4.6	Nyquist plot of Zn-Fc RFB in an impedance test. Ohmic resistance is measured to be 810 Ω·cm ² . /Large internal resistance is due to the large thickness and low conductivity of the organic electrolyte.	114

Figure 5.1	<p>(a) Cycling test of NASICON-membrane-based Zn-Ce RFB. An initial SOC of 50% and a current density of 0.2 mA/cm^2 were used for both charging and discharging. Every cycle included the same time of 10 min for both charging and discharge operation. Energy efficiency of each cycle in the 100-cycle test is 90% on average. Coulombic efficiency was constant at 100%, due to the fixed time and current for both charging and discharging operation. Voltage efficiency is therefore equal to energy efficiency. (b) Polarization curve of Zn-Ce RFB during the initial state. Detailed experimental conditions are the same as those for (a).....</p>	121
Figure A1	<p>Flow chart of simulation model algorithm. Reprinted from <i>J Power Sources</i> 247, 1040-1051, with permission from Elsevier.</p>	142

ABSTRACT

Wide deployment of intermittent energy generation (*e.g.*, wind and solar) calls for low-cost energy storage system for smooth and reliable power output. Redox flow batteries (RFBs) have been identified as one of the most suitable systems for large-scale energy storage. Different from conventional batteries that store energy in solid electrode, RFBs take advantage of flowable electrolytes as energy-storage media and therefore bring unprecedented freedom in independent tuning of energy and power of RFB. The method to separate two chemically reactive electrolytes plays a key role in RFB. Current RFBs adopt a single ion-exchange membrane (IEM) as separator, which can physically separate two electrolytes but ionically conduct them with commuting ions. Ever since the invention in 1974, the single-membrane configuration has enabled a tremendous amount of new combinations of elements from periodic table for battery application. However, single IEM configuration remains imperfect: 1) IEM is designed to either conduct cation while excluding anion (cation-exchange membrane, CEM), or conduct anion while excluding cation (anion-exchange membrane, AEM). This property only allows the combination of redox pairs in the same type of charge, leaving a lot of promising redox pair combinations useless; 2) IEM cannot reach 100% selectivity of commuting ion, which results in an inevitable crossover of redox pairs, causing electrolyte imbalance, coulombic efficiency and capacity loss; 3) IEM contributes the biggest voltage loss due to its large internal resistance in many RFBs, and is usually one of the most expensive components in the stack, both indirectly or directly increasing the cost of RFBs.

Aiming at solving the problems in single-membrane RFBs, this work explored three possible routes that provide alternative configurations to current RFBs: 1) a double-membrane RFB that could combine redox pairs with different types of charge, and of different supporting pHs; 2) a single-membrane all-iron (all-Fe) flow battery that adopts the same elements on both sides, which is immune to the crossover of metal ions; 3) a membrane-less RFB that utilizes immiscible organic and inorganic electrolytes, which thermodynamically separate two redox species and eliminate the usage of membrane in RFB.

In the double-membrane RFB design, both AEM and CEM are incorporated in cell to isolate cation and anion redox pairs respectively. A middle electrolyte is used to ionically conduct two membranes. Three examples have been successfully demonstrated: Zn-Ce ($\text{Zn(OH)}_4^{2-}/\text{Zn}$ vs. $\text{Ce}^{4+}/\text{Ce}^{3+}$), S-Fe ($\text{S}_4^{2-}/\text{S}_2^{2-}$ vs. $\text{Fe}^{3+}/\text{Fe}^{2+}$) and Zn-Fe ($\text{Zn(OH)}_4^{2-}/\text{Zn}$ vs. $\text{Fe}^{3+}/\text{Fe}^{2+}$) RFBs. Zn-Ce RFB provides the highest cell voltage among all aqueous RFBs as 3.08 V. S-Fe RFB combines very inexpensive anion redox pair ($\text{S}_4^{2-}/\text{S}_2^{2-}$) and cation redox pair ($\text{Fe}^{3+}/\text{Fe}^{2+}$) together (1.22 V) and brings low electrolyte cost. Zn-Fe RFB has the best balance between high voltage (2.0 V) and low electrolyte cost, thus bringing high performance and low capital cost. Middle electrolyte was found to be an important role in controlling total cell resistance. With optimally engineered middle electrolyte, Zn-Fe RFB shows high power density (676 mW/cm^2) and the lowest system cost so far among several notable RFBs, under $\$100/\text{kWh}$, which is below the cost target for energy storage system set by Department of Energy of U.S. in the 2023 term. Such a low cost puts Zn-Fe RFB in a very promising position for future development and commercialization.

In the single-membrane all-Fe RFB, the same element, iron, is used in redox pairs in both positive and negative electrolytes with different coordination chemistries. The adoption of the same element fundamentally eliminates the cross-contamination in RFBs that uses two different elements. All-Fe RFB shows good durability and stability over cycle test. The slow diffusion of coordinate agent, however, was identified as a prominent concern in capacity retention in long-term. Nonetheless, all-Fe RFB remains as a good attempt in combining redox pairs of the same element with different coordination chemistries to extend the spectrum of redox pairs for RFB application.

In the membrane-less RFB design, a new separation method of redox pairs is introduced by employing immiscible organic and inorganic electrolytes. Redox pairs are thus thermodynamically separated and require no membrane. A zinc-ferrocene RFB was demonstrated as an example for this membrane-less design and good durability and stability were proved in cycle test. This concept broadens the method to construct flow battery and brings more possible combinations between organic and inorganic redox pairs in RFB application.

The new designs and concepts studied in this work successfully demonstrated that invention of new cell structure could greatly enrich and diversify the category of RFBs, expanding new redox chemistries and enabling new redox pair combinations for RFB. Setting those three cell designs as frame work, we are expecting and looking forward to more exciting redox chemistries being explored.

Chapter 1

INTRODUCTION

1.1 Energy Storage System and Redox Flow Battery

With growing concerns over the over use of fossil fuels, renewable energy received great attention for electricity generation in recent years^[1, 2]. Solar and wind are among the most abundant renewable energy resources and have gone through a rapid growth over the last decade world-widely^[3, 4]. However, solar and wind are both intermittent sources: solar power mostly peaks during noon time and vanishes at night; wind power can vary greatly over minutes, hours and days. Their variability brings great challenges to the electric grid if the contribution of intermittent electricity generation exceeds a certain portion, as on-demand and reliable power output is required by customers. Electrical energy storage (EES) is essential to cope with the intermittence nature of wind and solar: the excess electrical energy produced during low demand period can be stored temporarily in EES, and released to the grid when demand peaks^[5, 6]. The development of EES could further boost the wide deployment of wind and solar energy and, fundamentally, facilitate the transition to a clean and renewables-based society^[7].

Various EES technologies are available for grid storage^[8]. Among them, pumped hydro currently has the biggest share, more than 99% worldwide^[9]. Pumped

Part of Chapter 1 is reprinted from *Energy & Environmental Science*, **2015**, DOI: 10.1039/C5EE02341F. See Appendix C for permission.

hydro utilizes the gravitational potential energy of water by pumping water from lower place to higher place to store energy, and generates electricity through turbine when the water flows back down. The low cost of pumped hydro system (around \$100/kWh) stands out as its biggest advantage^[10]. However, it is limited by geographical conditions and site selection. Alternatively, electrochemical devices emerge as a flexible storage system that can be deployed in most places.

The electric battery is one of the most common electrochemical devices. It relies on the indirect electrochemical reaction between two redox pairs of different electric potentials. In traditional batteries, two solid redox pairs, which also serve as positive and negative electrodes, are separated by a liquid electrolyte. In the meanwhile, the electrolyte allows the commutation of supporting ions across positive and negative electrodes to balance the charge and finish the circuit. The use of solid electrode materials limits the cyclability of battery to mostly under 5000 cycles because of repeated solid deposition/dissolution^[5]. Grid energy storage calls for service life as long as more than 10 years, and a low system cost comparable to pumped hydro (\$100/kWh). Unfortunately, most conventional batteries cannot meet both requirements. In an aim to solve the issues of grid-energy storage, redox flow batteries (RFBs) received a renaissance, and were brought into the center of arena of various electrochemical devices in the late 2000s. RFBs have been identified as one of the most suitable systems for wind and solar energy storage due to their flexibility of design, extended discharge duration, and potential for long-term durability^[11-17].

Figure 1.1 shows the diagram of a typical redox flow battery. The redox flow battery concept employs two soluble redox pairs dissolved in flowable electrolytes as energy-storing material. As such, electrolytes can be stored in separate tanks and

pumped through the stack of flow cells for energy conversion, whereas the inside of the cell contains only inert electrodes and separator. The redox flipping of soluble redox ions, specifically metal ions, theoretically provides unlimited cyclability, as most metal ions would hardly degrade into other species. The long service life is then expected given the stability of other components in RFB.

The concept of RFB was enabled largely thanks to the successful development of ion-exchange membrane, which is positioned in the middle of a battery and isolates negative electrode redox pairs from positive electrode redox pair even when all of the four redox ions are freely dissolved in electrolytes ^[5, 6]. Equally importantly, the IEM also allowed the passage of non-electroactive counter ions to balance the charge between negative and positive electrolytes. The liberation of redox pairs from the solid electrodes transferred energy storage functionality from the electrodes to liquid electrolytes in external tanks, and this decoupling of energy storage from power delivery provided RFBs with unprecedented design flexibility and scalability. The storage capacity (which depends on the amount and concentration of electrolyte) and the power (which depends on stack area) can thus be tuned independently for various storage scenarios.

RFBs can be categorized in to two groups: aqueous and nonaqueous RFBs, depending on the supporting solvent. Due to their superior performance and low cost, aqueous RFBs has experienced more extensive research and development. Some of the most successful RFBs today are aqueous systems. On the other hand, nonaqueous RFBs have advantages such as larger electrochemical windows, extended temperature ranges of operation, and potentially low costs on an element basis. However,

nonaqueous RFBs are still in the very early stages of research, and great challenges still need to be addressed before successful implementation.

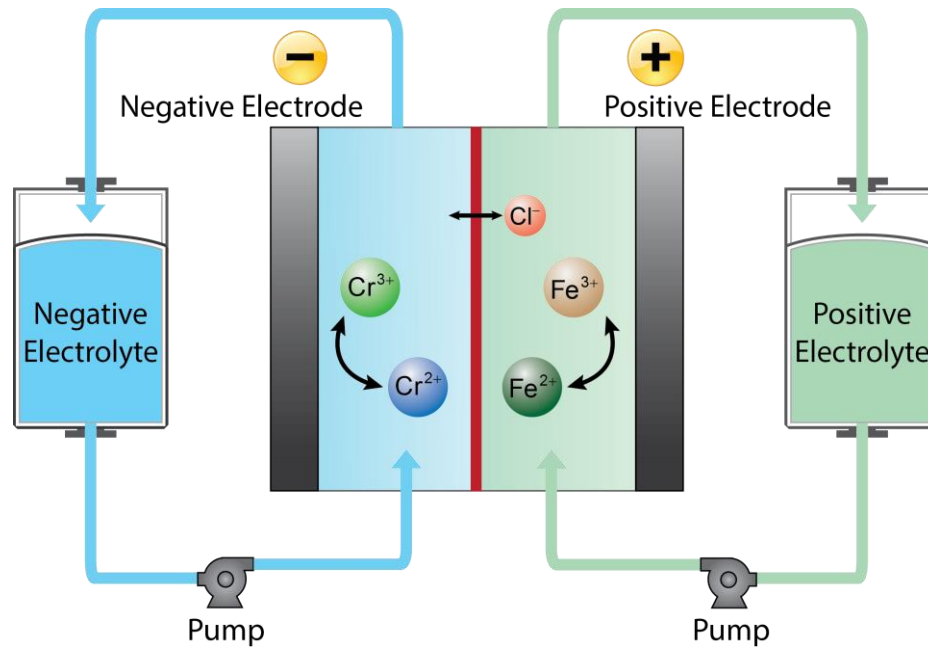


Figure 1.1 A typical redox flow battery structure: the Cr-Fe redox flow battery, the first redox flow battery, developed in 1974.

An RFB system could be characterized by several metrics for evaluation and comparison between different systems. The coulombic efficiency, voltage efficiency and energy efficiency are defined in Eq. 1.1, 1.2, 1.3.

$$CE = \frac{Q_{\text{discharge}}}{Q_{\text{charge}}} \quad (\text{Equation 1.1})$$

$$VE = \frac{V_{\text{discharge}}}{V_{\text{charge}}} \quad (\text{Equation 1.2})$$

$$EE = \frac{E_{\text{discharge}}}{E_{\text{charge}}} \quad (\text{Equation 1.3})$$

where $Q_{\text{discharge}}$, Q_{charge} are the capacities of discharge and charge, $V_{\text{discharge}}$, V_{charge} are the average cell voltages of discharge and charge, and $E_{\text{discharge}}$, E_{charge} are the energies of discharge and charge.

The capacity retention after a specific number of cycles is calculated by dividing the discharge capacity in the last cycle (Q_{last}) by the discharge capacity in the first cycle (Q_{first}), as shown in Eq. 1.4.

$$\text{Capacity retention} = \frac{Q_{\text{last}}}{Q_{\text{first}}} \quad (\text{Equation 1.4})$$

The State of Charge, or SOC, is defined as a percentage of available capacity for discharge to total capacity of the battery, as shown in Eq. 1.5.

$$\text{SOC} = \frac{Q_{\text{remaining}}}{Q_{\text{total}}} \times 100\% \quad (\text{Equation 1.5})$$

1.2 Aqueous Redox Flow Batteries

The first aqueous RFB was conceived by Lawrence H. Thaller in 1974 under the background of rising interest for means of storing bulk electrical power^[18]. The core part of an RFB system is the selection of two redox pairs, as redox pairs directly determine the standard cell voltage, kinetic constant and solubility. Figure 1.2 and Table 1.1 summarize those that have been used in RFB based on the charge type (cation or anion).

In theory, any two redox pairs with different electrode potentials can be picked to construct an RFB. However in practice, their choice and combination should be carefully considered to maximize the economy of the RFB in a specific application. An ideal RFB should incorporate two redox pairs that have facile kinetics, high solubilities, and a sufficiently large difference in electric potentials to create a high standard cell voltage.

In the single-membrane configuration, the two redox pairs should also be stable in the same pH environment, and have the same sign on their formal charges, i.e., either both cation redox pairs or both anion redox pairs. Over the past 40 years, a lot of different RFBs have been developed^[19], as summarized in Figure 1.2 by redox pairs. Some RFBs have received more attention and development, and are already on the edge of commercialization.

Table 1.1 Anion-based, cation-based and anion-cation hybrid redox pairs in RFBs

Flow battery redox pair		Standard redox potential (V)	Typical electrolyte
Anion-based redox pair	$\text{ClBr}_2^-/\text{Br}^-$ [20, 21]	+1.07*	HCl, ZnBr_2
	$\text{Br}_3^-/\text{Br}^-$ [22-25]	+1.05*	NaBr, H_2SO_4
	$\text{Fe}(\text{CN})_6^{3-}/\text{Fe}(\text{CN})_6^{4-}$ [26]	+0.36†	NaOH
	$\text{Fe}(\text{C}_6\text{H}_4\text{O})^-/\text{Fe}(\text{C}_6\text{H}_4\text{O})^{2-}$ [25]	+0.21†,‡	NaBr
	$\text{Fe}(\text{edta})^-/\text{Fe}(\text{edta})^{2-}$ [27]	+0.18†	NaAc
	$\text{Fe}(\text{C}_2\text{O}_4)_3^{3-}/\text{Fe}(\text{C}_2\text{O}_4)_3^{4-}$ [25]	-0.12†	NaAc
	$\text{S}_4^{2-}/\text{S}_2^{2-}$ [23]	-0.45	NaBr, NaOH
	$\text{Cr}(\text{edta})^-/\text{Cr}(\text{edta})^{2-}$ [27]	-0.96	NaAc
	$\text{Zn}(\text{OH})_4^{2-}/\text{Zn}$ [26]	-1.21 [28]	NaOH
Cation-based redox pair	$\text{Co}^{3+}/\text{Co}^{2+}$ [29]	+1.95	$\text{CH}_3\text{SO}_3\text{H}$
	$\text{Ce}_2\text{O}_6^{6+}/\text{Ce}^{3+}$	+1.87 [30]	HClO_4
	$\text{Ce}^{4+}/\text{Ce}^{3+}$ [31, 32]	+1.74	$\text{CH}_3\text{SO}_3\text{H}$, H_2SO_4
	$\text{Mn}^{3+}/\text{Mn}^{2+}$ [33]	+1.54	H_2SO_4
	$\text{NpO}_2^{2+}/\text{NpO}_2^+$ [34]	+1.14	HNO_3
	$\text{VO}_2^+/\text{VO}^{2+}$ [35-37]	+0.99	H_2SO_4 , $\text{CH}_3\text{SO}_3\text{H}$
	$\text{Fe}^{3+}/\text{Fe}^{2+}$ [18, 37-39]	+0.77	HCl
	Cu^{2+}/Cu [37]	+0.34	H_2SO_4
	$\text{Np}^{4+}/\text{Np}^{3+}$ [34]	+0.15	HNO_3
	$\text{Sn}^{4+}/\text{Sn}^{2+}$ [37]	+0.15	H_2SO_4
	$\text{Ti}^{4+}/\text{Ti}^{3+}$ [18, 24]	-0.06	HCl
	$\text{V}^{3+}/\text{V}^{2+}$ [20, 35, 39]	-0.26	H_2SO_4 , HCl
	$\text{Cr}^{3+}/\text{Cr}^{2+}$ [18, 24, 40]	-0.41	H_2SO_4 , HCl
	Fe^{2+}/Fe [38]	-0.45	HCl
	Zn^{2+}/Zn [21, 22, 29, 31, 36]	-0.76	NaBr, ZnCl_2 , $\text{CH}_3\text{SO}_3\text{H}$
	Anion-cation hybrid redox pair	$\text{Cr}_2\text{O}_7^{2-}/\text{Cr}^{3+}$ [40]	+1.23
$\text{Cr}(\text{edta})^+/\text{Cr}(\text{edta})^-$ [27]		+1.14†	NaAc

Nonionic redox pairs [41] and gas-phase redox pairs [42-46] are not included, as their RFBs may not need IEMs. Standard redox potentials are calculated from standard Gibbs free energies or cited directly from standard redox potential tables [47] unless otherwise noted. Note that, when H^+ or OH^- are involved, unity was used as its activity unless otherwise noted.

* Calculated from Gibbs free energies in the reference [48].

† Calculated from formation constant of complex in the reference [49].

‡ The complex structure was taken at pH = 6 from the reference [50].

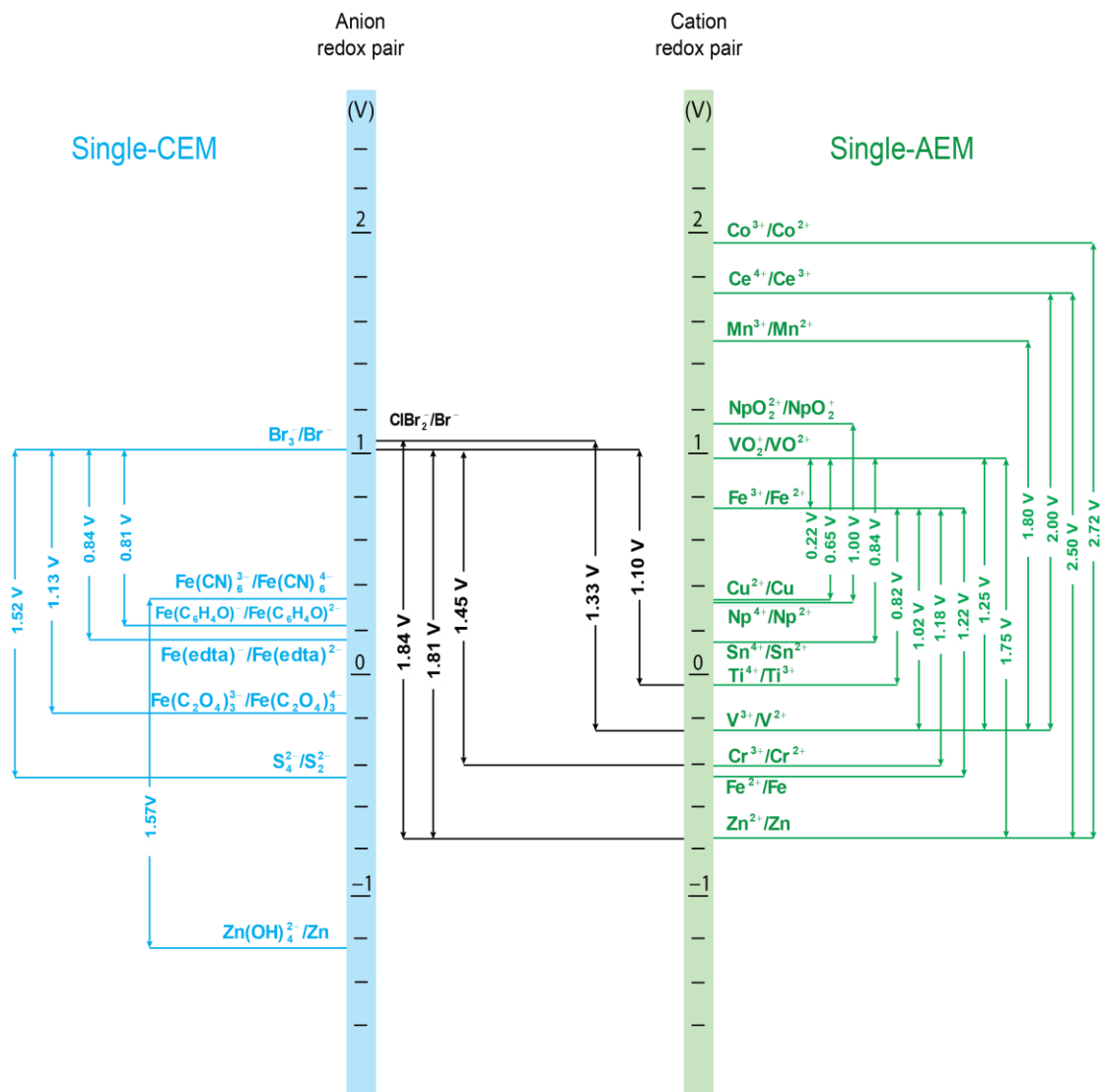
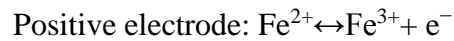


Figure 1.2 Redox pairs used in aqueous RFBs classified as cation and anion redox pairs, and RFBs built based on different redox pairs. The standard redox potentials of redox pairs are from the references in Table 1.1. The single-CEM cell is preferred for one anion-anion redox pair vs. another anion-anion redox pair (left region); the single-AEM cell is preferred for one cation-cation redox pair vs. another cation-cation redox pair (right region).

1.2.1 Chromium-Iron RFB

Chromium-Iron (Cr-Fe) RFB is the first example demonstrated by L. H. Thaller, who conceived of RFBs in 1974^[18, 51]. The Cr-Fe RFB uses $\text{Cr}^{3+}/\text{Cr}^{2+}$ and $\text{Fe}^{3+}/\text{Fe}^{2+}$ as the negative and positive redox pairs, as shown in Figure 1.1. The electrochemical reactions at the negative and positive electrodes are shown below.



The Cr-Fe RFB has been studied in detail in an NASA redox project from 1976-1984^[52]. Initially in the project, various redox pairs were scrupulously screened to find the most appropriate combination of redox pairs with optimal solubility, kinetics, cell voltage^[53]. Cr-Fe RFB was eventually determined to be further studied in detail and developed. The NASA project involves the work of membrane development^[54], catalyst study for $\text{Cr}^{3+}/\text{Cr}^{2+}$ ^[55], study of operation at elevated temperature and study of a pilot-scale system (1 kW, 12 kWh)^[52]. One of the key difficulties in Cr-Fe RFB is the crossover of Cr or Fe ions. Though the anion-exchange membrane was designed to conduct only anions, its selectivity cannot reach 100%, and Cr or Fe ions gradually diffuse from one side of the membrane to another during the cycle process. Crossover causes coulombic efficiency loss, capacity loss and electrolyte contamination, which could lower the standard cell voltage^[56]. Though a lot of early efforts were made to develop advanced membranes that could provide better selectivity and durability while maintain good conductivity, the newly invented membranes could not satisfy the strict requirement of a long service life. To mitigate the crossover problem, a pre-mixed Fe and Cr electrolyte was then used on both the positive and negative sides, with the sacrifice of lower cell voltage and doubled redox species usage. Although the first Cr-Fe RFB was calculated to have low system cost,

and a pilot system was built in the later period of NASA project, this RFB didn't receive commercial interest over the following three decades. The remaining challenges that were not completely mitigated in NASA project, such as long-term stability of $\text{Cr}^{3+}/\text{Cr}^{2+}$ catalyst, hydrogen evolution as side reaction at negative side, would possibly have hindered its continuous development.

1.2.2 Zinc-Bromine RFB

Zinc-Halogen (Zinc-chloride) RFB was first invented in 1884 by French chemist Charles Renard, which was at the time used to power the airship 'La France'^[57]. Because of this fact, some regarded Zn-Cl RFB as the first RFB. The technology was revived in the mid-1970s by Exxon in the U.S., and the Zinc-Bromine RFB was studied and developed^[57]. It should be noted that zinc redox pair is not completely soluble and its redox reaction involves the deposition and dissolution of solid zinc metal. The Zn-Br RFB is therefore usually termed as a "hybrid" RFB. The positive and negative electrode half reactions are shown below.



Zn-Br RFB has a cell voltage as high as 1.85 V. A microporous film is usually used as its separator to reduce stack cost. At positive electrolyte, complexing agents such as organic amines are added to increase the solubility of bromine and minimize the evolution of bromine. The low material costs of both zinc and bromine, high cell voltage (1.85 V vs. ~1.2 V for many other RFBs), high energy density (>70 Wh/L vs. ~30 Wh/L for many other RFBs), facile kinetics make Zn-Br very attractive for the past few decades. A number of companies have dedicated themselves to the development of Zn-Br RFB, including ZBB Energy (US), Primus Power (US),

RedFlow (Australia), Smart Energy (China), ZBEST Power (China). In recent years, effort in extending the Zn-Br RFB to other Zn-halide RFBs has also provided insights for improving performance and energy density. A Zn-Br/Cl RFB with a mixed positive electrolyte containing both bromine and chlorine showed an improved cell voltage (1.95 V) and very high theoretical energy density (>500 Wh/L)^[21]. A Zn-I RFB using I_3^-/I^- as the positive redox pair demonstrated 167 Wh/L energy density with a theoretical energy density exceeding 300 Wh/L, thanks to the very high solubility of zinc iodide (7 mol/L)^[58]. Continued progress in Zn-Br and other Zn-halide RFBs is promising and inspiring for their further development.

1.2.3 Sulfur-Bromine RFB

Sulfur-Bromine (S-Br) RFB was first patented in 1983^[59]. It employs polysulfide and bromide redox pairs at the negative and positive sides, respectively, as shown below.



The cell has an open-circuit voltage of 1.5 V. Both chemicals are abundant and of low cost. The system cost was estimated to be only \$109/kWh (2006 USD) at the optimal current density of 50 mA/cm² and the energy efficiency 64% for a 15 MW, 120 MWh system^[60]. The polysulfide redox pair has relatively sluggish kinetics compared with the bromide. Research has been focused on developing advanced catalysts for sulfur redox pair by using nickel foam^[61], activated carbon^[62] and cobalt-coated carbon felt^[63]. Nickel foam and cobalt-coated carbon felt showed good catalytic performance for the polysulfide redox pair: 27 mV overpotential for charge and 15 mV for discharge was observed at 50 mA/cm² for nickel foam, and ~30 mV

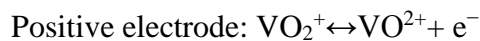
overpotential was observed for both charge and discharge on cobalt-coated carbon felt, compared to more than 200 mV overpotential for pure carbon felt electrode at the same current density. Though much progress has been made on polysulfide catalysts, technical challenges persist, including crossover of redox species, deposition of sulfur species, and long term stability.

1.2.4 All-Vanadium RFB

All-Vanadium (all-V) RFB has been considered one of the most promising RFBs ever since its invention^[64, 65]. Although both vanadium redox pairs have been investigated, and an all-V RFB concept was introduced in an early NASA report, it was excluded from serious research mostly due to the slow kinetics and high cost of the vanadium species^[53]. The first successful demonstration of an all-V RFB was eventually made by Skyllas et al. in 1984^[66, 67]. The all-V RFB has received increasing research effort ever since, and remained one of the most popular topics in RFB research. There is also intensive effort on its commercialization. Several emerging companies have successfully launched their all-V RFB systems, including UniEnergy, Primus in the United States, Rongke Power, Prudent Energy in China, and Cellennium in Thailand.

As discussed, crossover of redox species remains as a big concern for those RFBs employ different redox elements. Though the crossover problem could be mitigated by using mixed electrolytes, this method sacrifices the cell voltage and doubles the electrolyte usage and hence the cost. All-V RFB takes a more elegant approach by utilizing the same element on both the positive and negative sides and therefore fundamentally excluding the cross-contamination of two elements to yield

unlimited cyclability in theory. The electrochemical reactions on the positive and negative electrode are shown below.



All-V RFB has been thus far the most studied RFB and received increased attention with regards to commercialization. While there is a lot of work focusing on membrane development^[68] and catalyst study^[69], some of the most important advancements of all-V RFB were achieved recently in electrolyte and cell architectures. Researchers at Pacific Northwestern National Lab (PNNL) gained 70% increase in energy density by using a mixed acid as the supporting electrolyte. The mixed sulfuric and hydrochloric acid was found to improve the solubility of vanadium species from 1.7 M (in pure sulfuric acid) to 2.5 M, and extend the temperature range from 10–40 °C (in pure sulfuric acid) to –5–50 °C^[70]. The chlorine ion was found to complex with the V(IV) cation to form $[\text{V}_2\text{O}_3\text{Cl}\cdot 6\text{H}_2\text{O}]^{2+}$, which provides higher solubility and thermal stability at elevated temperatures^[71]. T. A. Zawodzinski et al. and M. Perry et al. both achieved dramatic performance gains in the all-V RFB in discharge power density^[72-74], as high as 767 mW/cm² and 1300 mW/cm², respectively, compared to peak power densities less than 150 mW/cm² for conventional all-V RFB. The improvement hinges on the substantial reduction of internal resistance, which was attributed as the cause of major voltage loss in conventional all-V RFB, by constructing a new membrane-electrode-assembly type cell structure. The large improvement of power density could greatly minimize the area of RFB stack and reduce the overall cost.

Despite the level of study and advancement of the all-V RFB, the high cost of vanadium materials still remains the biggest obstacle for its wide deployment. The vanadium materials alone cost ~\$70/kWh for system capital cost (\$13.5/kg for V₂O₅, see Appendix B Table B1, Table B3 for calculation). The current cost of the all-V RFB is estimated to be \$300-350/kWh^[10], which is still much higher than pumped hydro or compressed air storage technologies (\$100/kWh). Further development of more advanced stacks and inexpensive exploit and refinement of vanadium ore are needed to bring broader market penetration to the all-V RFB.

1.3 Nonaqueous Redox Flow Batteries

Although the majority of RFBs are based on aqueous solutions as electrolytes, and these aqueous RFBs have demonstrated high cell performance and excellent system reliability, nonaqueous RFBs have become an emerging area that has garnered increasing research in recent years. Since the first concept of nonaqueous RFB was proposed by Singh in 1984,^[75] many types of nonaqueous RFBs have been invented and studied, which clearly confirm the feasibility of using organic solvents for RFBs^[76].

Compared with aqueous RFBs, nonaqueous RFBs can offer a wide range of working temperatures, high cell voltage, and potentially high energy density, thanks to the nature of organic solvents. As part of the family of RFBs, nonaqueous RFBs, especially those with the ability to work at low temperatures, are an important complement to aqueous RFBs, broadening the spectrum of RFB applications.

Non-aqueous RFBs can be categorized by the redox pairs used: metal-based redox pairs and metal-free redox pairs, which are discussed in the following two sections.

1.3.1 Metal-based Redox Pairs

The use of metal-based redox pairs in nonaqueous RFBs is a natural extension of their success in aqueous RFBs. Unlike the simple metal ions in aqueous RFBs, metal-organic ligand coordination complexes are used to construct redox pairs in nonaqueous RFBs, largely due to the need to improving their solubilities in organic solvents. Simple metal salts have very limited solubilities in most organic solvents, but metal-organic ligand complexes are reasonably soluble in many organic solvents.

A metal-ligand complex is composed of a metal center and several chelating ligands. The metals used to construct nonaqueous RFB pairs include Ru,^[77-80] Fe,^[77-79, 81, 82] U,^[83-89] V,^[90-95] Cr,^[96] Ni,^[81, 82] Mn,^[97] and Co.^[98] Among those metals, V has become increasingly attractive because it has good redox reversibility. Ru also shows good redox reversibility but its cost is prohibitive. For example, the retail price of Ru(acac)₃ is over 30 times higher than that of V(acac)₃, i.e., \$72.4/g vs. \$1.96/g, from Sigma-Aldrich (with the same ligand and the same purity of 97%). With the aim of reusing the massive amount of depleted and recovered radioactive elements from the nuclear industry, Yamanura et al. has pioneered the use of U as redox pairs for nonaqueous RFBs. Fe, Cr, Mn, and Co are inexpensive and have the potential to drastically lower the material cost for nonaqueous RFBs. However, these metals have poorer redox reversibilities than Ru and V.

Double-oxygen bidentate ligands include “acac” (acetylacetonone),^[78-80, 83, 86, 89-93, 95-97] “hfa” (hexafluoroacetylacetonone),^[83] “tfa” (1,1,1-trifluoroacetylacetonone), “fod”

(hexafluorobutanoylpivaloylmethane),^[83] “pta” (pivaloyltrifluoroacetone),^[83] “ba” (benzoylacetone), “dpm” (dipivaloylmethane),^[83] “btk” [m-bis(2,4-dioxo-1-pentyl)benzene],^[84, 85, 88, 89] “etk” (8-oxo-2,4,12,14-acetylacetone),^[84, 85, 89] and “acacen” [bis(acetylacetone)ethylenediamine].^[98] Among those organic ligands, “acac” is the most frequently used species in the construction of metal-organic coordination complexes serving as redox pairs for nonaqueous RFBs, since it is one of the simplest bidentate ligands that form strong coordination bonds with many transition metals.

The double-nitrogen bidentate ligand used includes “bpy” (2,2'-bipyridine),^[77-79, 81, 82] and the double-sulfur bidentate ligand used includes “mnt” (maleonitriledithiolene),^[94] Hybrid-atom bidentate ligand includes “tmma” (N,N,N',N'-tetramethylmalonamide)^[87] where both the oxygen atom and the nitrogen atom serve as each dentate of the bidentate. In addition, there are monodentate ligands such as (single-oxygen) “dmso” (dimethyl sulfoxide) and (single-oxygen) “dmf” (dimethylformamide).^[83]

For an oxygen-dentate ligand, such as acac, the metal in the metal-ligand complex facilitates electron transfer via the changing of its oxidation number upon redox reaction, in which ligands are redox-innocent. For nitrogen- (such as bpy) or sulphur-dentate ligands (such as mmt), both metal and ligand can provide electron transfer, in which ligands are redox-non-innocent. Combination of different metals (with variable oxidation numbers) and different ligands (with variable substituents), metal-ligand complex redox pairs offer a wide range of redox potentials, shown in Table 1.2. Note that the redox potential can be influenced substantially by both the organic solvent and the supporting electrolyte.^[99]

The properties of metal-ligand coordination complexes are the result of the interactions between metals and ligands. As such, it is difficult to compare one group of ligands to another. Within the same group of ligands, the impact of ligand however can be seen. For example, the increase of the basicity of the oxygen-dentate ligand (via introducing electron-withdrawing substituents) can lead to a negative shift in the redox potential of a U-oxygen-dentate ligand complex: an increase of eight units of pK_a value for basicity of ligands leads to a negative shift of roughly 500 mV for redox potential for U(VI)/U(V) complex redox pairs. It is expected that the rate constant of the redox reaction will also be impacted, but the correlation has not been elucidated yet.

Generally speaking, the redox kinetics of metal-ligand complex redox pairs in nonaqueous solvents is more facile than that of simple metal ions-based redox pairs in aqueous system. As seen in Table 1.2, the standard rate constant is generally on the order of 10^{-3} – 10^{-1} cm s^{-1} for most metal-ligand complex redox pairs, which is statistically one to two orders of magnitude higher than those of aqueous metal ions-based redox pairs (a wide range of 10^{-6} – 10^{-2} cm s^{-1}).^[15] This can be rationalized by the fact that the electron transfer in metal-ligand complexes does not involve the change of coordinating groups.^[100, 101] Facile redox kinetics can lower the electrode overpotential, which is useful for achieving high voltage efficiency.

Aside from metal-ligand complexes, polyoxometalates are an emerging class of redox compounds to serve as metal-based redox pairs in nonaqueous RFBs.^[102] Polyoxometalates are polyatomic ions consisting of three or more transition metal oxyanions linked together by shared oxygen atoms to form a large, closed, three-dimensional framework. Two polyoxometalate redox pairs were introduced recently

by Anderson et al. for both aqueous and nonaqueous RFBs: $[\text{SiV}_3\text{W}_9\text{O}_{40}]^{10-}/[\text{SiV}_3\text{W}_9\text{O}_{40}]^{13-}$ with the metal W as the electroactive element and $[\text{SiV}_3\text{W}_9\text{O}_{40}]^{7-}/[\text{SiV}_3\text{W}_9\text{O}_{40}]^{10-}$ with the metal V as the electroactive element.^[102] Both pairs offer up to three transferred electrons in their redox reactions. With organic cations such as Bu_4N^+ , these polyoxometaltes are soluble in many organic solvents. Considering the number of available structures, polyoxometalates may be a promising class of metal-based redox systems to be explored for advancing nonaqueous RFBs.

1.3.2 Metal-free Redox Pairs

Redox pairs can also be constructed with metal-free organic redox compounds for nonaqueous RFBs (Table 1.3). Unlike the metal-based redox pairs, the electron transfer here involves the formation of stable radicals. By gaining or losing electrons, neutral organic molecules can form radical anions or radical cations, respectively. In turn, the electron transfer between radical ions associated with neutral molecules lead to certain redox potentials. One example is the first proposed metal-free redox pairs for nonaqueous RFBs^[103]: one pair was constructed by a neutral rubrene molecule and rubrene radical anion (i.e., Rubrene/Rubrene^{-•} with a redox potential of -1.9 V vs. SHE) and the other by a neutral rubrene molecule and rubrene radical cation (i.e., Rubrene^{+•}/Rubrene with a redox potential of 1.4 V vs. SHE).

Most radicals are extremely reactive and thus short-lived, but there are many radicals that are relatively stable and sometimes persistent; thus, they could be used to construct metal-free redox pairs. From a structural point of view, radicals can be stabilized through electronic resonance, steric crowding, and/or dimer formation.^[104]

Besides rubrene, other metal-free redox compounds include 2,2,6,6-tetramethyl-1-piperidinyloxy (TEMPO[•], note this radical is neutral),^[105] N-

methylphthalimide (NMPI),^[105] 1,5-bis(2-(2-(2-methoxyethoxy)ethoxy)ethoxy)anthracene-9,10-dione (15D3GAQ),^[106] 2,5-di-tert-butyl-1,4-bis(2-methoxyethoxy)benzene (DBBB),^[107] and a quinoxaline family^[107] (Table 1.3). The neutral TEMPO• radical is a classic persistent radical molecule, whose stability is provided by both steric crowding from four methyl groups and electronic resonance. NMPI•⁺ cationic radical is stabilized through the electronic resonance with its electron-deficient benzene ring.^[105] 15D3GAQ•⁻ anionic radical is likely stabilized by the electronic resonance across two benzene rings.^[108] DBBB•⁺ cationic radical is largely stabilized via the electronic resonance from para-methoxybenzene ring as an extended conjugation system (steric crowding is also provided from two t-butyl substituents).^[109] With different substituents, a group of quinoxaline redox compounds have been introduced and these quinoxaline anionic radicals are likely stabilized by their electronic resonance.

Considering the typical energy-storing timescale in RFBs being a few hours to up to a few days, the stability of radical-involving metal-free redox pairs may be sufficient. For example, up to 30 charge-discharge cycles have been demonstrated from a nonaqueous RFB based on a quinoxaline redox pair and a DBBB based redox pair, without substantially compromising either charge or discharge capacities.^[107] Such cyclability supports the feasibility of using radical redox compound for nonaqueous RFBs.

The substituent of redox compounds impacts not only the redox potential but also the redox activity for redox pairs. For example, electron-donating substituents are shown to lower the redox potential but enhance the redox activity for the Quinoxaline/Quinoxaline•⁻ redox pair.^[107] Note that the influence of substituent is

expected to be different from that of anionic radicals and cationic radicals. Meanwhile, the substituent has significant impact on the solubility of redox compounds. For instance, with two substituents of 2-(2-(2-methoxyethoxy)ethoxy)ethoxy, 15D3GAQ has a solubility five times higher than that of the substituent-free anthraquinone (Aq) (more than 0.25 M for 15D3GAQ vs. less than 0.05 M for Aq, in solvent PC).^[106]

Based on a variety of redox radicals, metal-free redox pairs offer a wide range of redox potentials and large rate constants, similar to metal-based redox pairs (Table 1.3). Like metal-based redox pairs, electron transfer does not involve any bond forming or breaking; hence, the redox kinetics is very fast. Unlike metal-based redox compounds, whose solubilities are generally limited (mostly less than 1 M), some metal-free redox compounds can offer very high solubilities, such as substituent-free quinoxaline, which has a solubility of 7 M in PC.^[107]

Considering the huge number of stable radicals and possible substituent modifications, there are a great deal of possible choices in organic compounds for constructing metal-free redox pairs for nonaqueous RFBs.

Table 1.2 Metal-based redox pairs proposed in nonaqueous RFBs

Redox pair ^[a]	$\phi^{\bullet[b]}$ (V vs. SHE)	$k^0[c]$ (cm s ⁻¹)	Test condition ^[d]
[Ru(bpy) ₃] ³⁺ /[Ru(bpy) ₃] ²⁺	1.5 (from Ag ⁺ /Ag) ^[77]	3.4×10^{-3} (from $i_0^{[e]}$) ^[110]	
[Fe(bpy) ₃] ³⁺ /[Fe(bpy) ₃] ²⁺	1.3 (from SCE) ^[110]	1.3×10^{-2} (from i_0) ^[110]	
[Ru(acac) ₃] ⁺ /Ru(acac) ₃	1.2 (from SCE) ^[110]	4.6×10^{-2} (from i_0) ^[110]	
[Mn(acac) ₃] ⁺ /Mn(acac) ₃	1.2 (from Ag ⁺ /Ag) ^[97]		0.5 M Et ₄ NBF ₄
[V(acac) ₃] ⁺ /V(acac) ₃	1.0 (from Ag ⁺ /Ag) ^[90]	6.5×10^{-4} (DMSO, 0.05 M Et ₄ NPF ₆) ^[92]	
[Cr(acac) ₃] ⁺ /Cr(acac) ₃	1.0 (from Ag ⁺ /Ag) ^[96]		0.5 M Et ₄ NBF ₄

[V(mnt) ₃] ⁻ /[V(mnt) ₃] ²⁻	0.9 (from Fc ⁺ /Fc) ^[94]		0.1 M Bu ₄ NPF ₆
[Co(acacen)] ⁺ /Co(acacen)	0.3 (from Ag ⁺ /Ag) ^[98]		0.1 M Et ₄ NPF ₆
Mn(acac) ₃ /[Mn(acac) ₃] ⁻	0.1 (from Ag ⁺ /Ag) ^[97]		0.5 M Et ₄ NBF ₄
[V(mnt) ₃] ²⁻ /[V(mnt) ₃] ³⁻	-0.2 (from Fc ⁺ /Fc) ^[94]		0.1 M Bu ₄ NPF ₆
[UO ₂ (dmsO) ₅] ⁻ /[UO ₂ (dmsO) ₅] ²⁻	-0.3 (from Fc ⁺ /Fc) ^[83]		DMSO, 0.1 M Bu ₄ NClO ₄ , Pt
[UO ₂ (hfa) ₂] ⁻ /[UO ₂ (hfa) ₂] ²⁻	-0.3 (from Fc ⁺ /Fc) ^[83]		DMSO, 0.1 M Bu ₄ NClO ₄ , Pt
[UO ₂ (tfa) ₂] ⁻ /[UO ₂ (tfa) ₂] ²⁻	-0.3 (from Fc ⁺ /Fc) ^[83]		DMSO, 0.1 M Bu ₄ NClO ₄ , Pt
[U(tmma) ₄] ⁴⁺ /[U(tmma) ₄] ³⁺	-0.4 (from Fc ⁺ /Fc) ^[87]	4.8 × 10 ⁻⁷ ^[87]	DMF, 0.1 M Bu ₄ NBPh ₄ , Pt
Ru(acac) ₃ /[Ru(acac) ₃] ⁻	-0.5 (from SCE) ^[110]		
[UO ₂ (fod) ₂] ⁻ /[UO ₂ (fod) ₂] ²⁻	-0.5 (from Fc ⁺ /Fc) ^[83]		DMF, 0.1 M Bu ₄ NClO ₄ , Pt
[UO ₂ (pta) ₂] ⁻ /[UO ₂ (pta) ₂] ²⁻	-0.5 (from Fc ⁺ /Fc) ^[83]		DMSO, 0.1 M Bu ₄ NClO ₄ , Pt
[SiV ₃ W ₉ O ₄₀] ⁷⁻ /[SiV ₃ W ₉ O ₄₀] ¹⁰⁻	-0.5 (from Li ⁺ /Li) ^[102]		PC, 0.5 M Bu ₄ NOTf, GC
[UO ₂ (ba) ₂] ⁻ /[UO ₂ (ba) ₂] ²⁻	-0.7 (from Fc ⁺ /Fc) ^[83]		DMSO, 0.1 M Bu ₄ NClO ₄ , Pt
UO ₂ (acac) ₂ /[UO ₂ (acac) ₂] ⁻	-0.8 (from Fc ⁺ /Fc) ^[88]	7.7 × 10 ⁻³ ^[88]	DMSO, 0.1 M Bu ₄ NPF ₆ , GC
[UO ₂ (dpm) ₂] ⁻ /[UO ₂ (dpm) ₂] ²⁻	-0.8 (from Fc ⁺ /Fc) ^[83]		DMSO, 0.1 M Bu ₄ NClO ₄ , Pt
UO ₂ (btk)/[UO ₂ (btk)] ⁻	-0.8 (from Fc ⁺ /Fc) ^[88]	1.03 × 10 ⁻³ ^[88]	DMSO, 0.1 M Bu ₄ NPF ₆ , GC
UO ₂ (etk)/[UO ₂ (etk)] ⁻	-0.8 (from Fc ⁺ /Fc) ^[89]	1.1 × 10 ⁻² ^[89]	DMSO, 0.1 M Bu ₄ NClO ₄ , GC
[Ru(bpy) ₃] ²⁺ /[Ru(bpy) ₃] ⁺	-1.1 (from Ag ⁺ /Ag) ^[77]	2.0 × 10 ⁻¹ (DMF, 0.2 M Bu ₄ NClO ₄ , Pt) ^[111]	
[Fe(bpy) ₃] ²⁺ /[Fe(bpy) ₃] ⁺	-1.1 (from SCE) ^[110]	1.6 × 10 ⁻¹ (DMF, 0.2 M Bu ₄ NClO ₄ , Pt) ^[111]	
V(acac) ₃ /[V(acac) ₃] ⁻	-1.2 (from Ag ⁺ /Ag) ^[90]	8.7 × 10 ⁻⁴ (from <i>i</i> ₀) ^[91]	0.5 M Et ₄ NBF ₄
[Ni(bpy) ₃] ²⁺ /Ni(bpy) ₃	-1.2 (from Ag ⁺ /Ag) ^[82]		PC, 0.05 M Et ₄ NBF ₄
U(pta) ₄ /[U(pta) ₄] ⁻ (or U(pta) ₃)	-1.3 (from Fc ⁺ /Fc) ^[83]		DMSO, 0.1 M Bu ₄ NClO ₄ , Pt
[V(mnt) ₃] ³⁻ /[V(mnt) ₃] ⁴⁻	-1.4 (from Fc ⁺ /Fc) ^[94]		0.1 M Bu ₄ NPF ₆
Co(acacen)/[Co(acacen)] ⁻	-1.7 (from Ag ⁺ /Ag) ^[98]		0.1 M Et ₄ NPF ₆
U(btk) ₂ /[U(btk) ₂] ⁻	-1.8 (from Fc ⁺ /Fc) ^[89]	8.8 × 10 ⁻³ ^[89]	DMF, 0.1 M Bu ₄ NClO ₄
U(acac) ₄ /[U(acac) ₄] ⁻ (or U(acac) ₃)	-1.8 (from Fc ⁺ /Fc) ^[89]	1.7 × 10 ⁻² ^[89]	DMF, 0.1 M Bu ₄ NClO ₄
U(etk) ₂ /[U(etk) ₂] ⁻	-1.8 (from Fc ⁺ /Fc) ^[89]	1.5 × 10 ⁻² ^[89]	DMF, 0.1 M Bu ₄ NClO ₄
Cr(acac) ₃ /[Cr(acac) ₃] ⁻	-1.8 (from Ag ⁺ /Ag) ^[96]		0.5 M Et ₄ NBF ₄
[SiV ₃ W ₉ O ₄₀] ¹⁰⁻ /[SiV ₃ W ₉ O ₄₀] ¹³⁻	-2.2 (from Li ⁺ /Li) ^[102]		PC, 0.5 M Bu ₄ NOTf

[a] Full names of the ligand abbreviations: “bpy” stands for 2,2'-dipyridine, “acac” for acetylacetonate, “mnt” for maleonitriledithiolene, dmsO for dimethyl sulfoxide, “hfa” for hexafluoroacetylacetonate, “tfa” for 1,1,1-trifluoroacetylacetonate, “tmma” for N,N,N',N'-tetramethylmalonamide, “fod” for hexafluorobutanoylpivaloylmethane, “pta” for pivaloyltrifluoroacetone, “ba” for benzoylacetone, “dpm” for dipivaloylmethane, “btk” for m-bis(2,4-dioxo-1-pentyl)benzene, “etk” for 8-oxo-2,4,12,14-acetylacetonate, and “acacen” for bis(acetylacetonate)ethylenediamine.

[b] ϕ° : formal redox potential. Potential was converted to SHE scale by relationships: Ag⁺/Ag = 0.54 V vs. SHE, SCE = 0.24 V vs. SHE, Li⁺/Li = -3.00 V vs. SHE, and Fc⁺/Fc = 0.69 V vs. SHE.^[99] Caution is needed for using the potential conversion.

[c] *k*⁰: standard rate constant of redox reaction.

[d] Test conditions are AN as solvent, 0.1 M Et₄NBF₄ as supporting electrolyte, and GC as electrode, unless otherwise noted.

[e] *i*₀: exchange current density.

Table 1.3 Metal-free redox pairs proposed in nonaqueous RFBs

Redox pair ^[a]	ϕ° ^[b] (V vs. SHE)	k^0 ^[c] (cm s ⁻¹)	Test conditions ^[d]
Rubrene ^{•+} /Rubrene	1.4 (from Ag wire) ^[103]		AN:ToI, 0.05 TBAP, GC
DBBB ^{•+} /DBBB	1.0 (from Li ⁺ /Li) ^[107]	1.0×10^{-2} (estimated)	
TEMPO ^{•+} /TEMPO [•]	0.9 (from Ag wire) ^[105]	1.0×10^{-1} (0.1 TBABF ₄ , Pt) ^[112]	AN, 1 M NaClO ₄ , GC
Quinoxaline/Quinoxaline ^{•-}	0.1 (from Li ⁺ /Li) ^[107]		
DPh-quinoxaline/DPh-quinoxaline ^{•-}	0.0 (from Li ⁺ /Li) ^[107]		
Me-quinoxaline/Me-quinoxaline ^{•-}	-0.1 (from Li ⁺ /Li) ^[107]		
DMe-quinoxaline/DMe-quinoxaline ^{•-}	-0.2 (from Li ⁺ /Li) ^[107]		
TMe-quinoxaline/TMe-quinoxaline ^{•-}	-0.2 (from Li ⁺ /Li) ^[107]		
DPh-quinoxaline ^{•-} /DPh-quinoxaline ^{•2-}	-0.3 (from Li ⁺ /Li) ^[107]		
Quinoxaline ^{•-} /Quinoxaline ^{•2-}	-0.4 (from Li ⁺ /Li) ^[107]		
Me-quinoxaline ^{•-} /Me-quinoxaline ^{•2-}	-0.4 (from Li ⁺ /Li) ^[107]		
15D3GAQ ^{•-} /15D3GAQ ²⁻	-0.5 (from Li ⁺ /Li) ^[106]		PC, 1 M LiPF ₆ , GF
DMe-quinoxaline ^{•-} /DMe-quinoxaline ^{•2-}	-0.5 (from Li ⁺ /Li) ^[107]		
TMe-quinoxaline ^{•-} /TMe-quinoxaline ^{•2-}	-0.5 (from Li ⁺ /Li) ^[107]		
15D3GAQ/15D3GAQ ^{•-}	-0.8 (from Li ⁺ /Li) ^[106]		1 M LiPF ₆ , GF
NMPI/NMPI ^{•-}	-0.8 (from Ag wire) ^[105]	4.6×10^{-2} (0.1 TBABF ₄ , Pt) ^[113]	AN, 1 M NaClO ₄ , GC
Rubrene/Rubrene ^{•-}	-0.9 (from Ag wire) ^[103]		AN:ToI, 0.05 TBAP, GC

[a] Full names of the abbreviations: DBBB: 2,5-di-tert-butyl-1,4-bis(2-methoxyethoxy)benzene; TEMPO: 2,2,6,6-tetramethyl-1-piperidinyloxy; NMPI: N-methylphthalimide; 15D3GAQ: 1,5-bis(2-(2-(2-methoxyethoxy)ethoxy)ethoxy)anthracene-9,10-dione.

[b] ϕ° : formal redox potential. Potential was converted to SHE scale by relationships: Ag⁺/Ag = 0.54 V vs. SHE, and Li⁺/Li = -3.00 V vs. SHE. Caution is needed for using the potential conversion.

[c] k^0 : standard rate constant of redox reaction.

[d] Test conditions are PC as solvent, 0.2 M LiPF₆ as supporting electrolyte, and Pt as electrode, unless otherwise noted.

1.4 Challenges for State-of-the-art RFBs

To serve as a grid-scale energy storage system, RFB must maintain very low cost to be competitive with existing technologies such as pumped hydro or compressed air. To make electricity storage systems economically viable, the U.S.

Department of Energy has set a system capital cost target of \$150/kWh by 2023. However, these targets have not been met so far due to the high cost of redox pairs and/or the low power density of cells^[114]. For example, the most developed all-vanadium (denoted as all-V) RFBs currently have a system capital cost ~\$300–\$800/kWh.

The RFB system cost has two major contributions, electrolyte cost and stack cost:

$$C_{\text{sys}} \approx C_e + C_s = U_e/V_{\text{eff}} + U_s/(t \cdot I \cdot V_{\text{eff}}) \quad (\text{Equation 1.6})$$

where, C_{sys} , C_e and C_s are system, electrolyte and stack cost (\$/kWh), respectively; U_e is the unit cost of electrolyte including redox elements and supporting salts/acids/bases (\$/Ah); U_s is the unit cost of stack including electrodes, membranes and bipolar plates (\$/m²); V_{eff} is the effective discharge cell voltage (V); t is the designed discharge duration (h); and I is the current density (A/m²).

From Eq. 1.6, low system cost can be achieved by minimizing U_e and/or U_s , or maximizing V_{eff} . Low U_e and U_s can be obtained by using low cost redox pairs and stack material, while high V_{eff} requires high reversible cell voltage, small overpotential and internal resistance, as shown in Eq. 1.7.

$$V_{\text{eff}} = V_{\text{rev}} - \eta - I \cdot R \quad (\text{Equation 1.7})$$

where, V_{rev} is the reversible voltage, η is the total activation overpotential at both electrodes (V), I is the current density and R is the area-specific internal cell resistance ($\Omega \cdot \text{cm}^2$).

Though more than four decades have passed since the first invention of Cr-Fe RFB and all possible elements on the periodic table has been evaluated for RFB applications, current RFBs cannot satisfy simultaneously low U_e and high V_{eff} at high

current densities. In aqueous RFBs, for example, the All-V RFB recently achieved dramatic improvement in its V_{eff} at high current density by reduction of internal resistance, but their U_e is too high; On the other hand, the Cr-Fe RFB has low U_e , but its V_{eff} is low due to the intrinsically low reversible cell voltage and sluggish kinetics of the Cr redox pair. In terms of nonaqueous RFBs, the substantially low conductivities for organic electrolytes results in much larger internal resistances compared with aqueous systems, and thus precludes operation at high current densities to yield high V_{eff} . It is therefore imperative to find two redox pairs that have low elemental cost, fast redox kinetics, and high reversible voltage in a system with low internal resistance.

The fundamental barrier originates from the fact that almost all state-of-the-art RFBs rely on the single ion-exchange membrane (IEM) configuration ever since 1974 without any evolution. In a single-membrane setup, only limited combinations of redox pairs are available, because neither one single AEM nor one single CEM can effectively prevent the mixing of electroactive redox pairs with mixed ion charges, despite the fact that some of these mixed ion pairs can lead to RFBs with potentially higher performance and lower costs. Moreover, single-membrane configurations cannot separate acid and base electrolytes since either proton (H^+) or hydroxide (OH^-) would crossover the membrane and neutralize with each other.

Crossover of redox species is another problem caused by imperfect selectivity of ion-exchange membrane. For RFBs that employ redox pairs of different elements (*e.g.* Cr-Fe RFB), this problem could be mitigated by using mixed electrolyte but would sacrifice cell voltage and double redox material cost. An alternative approach is to use redox pairs of the same element. As one of the most successful RFBs so far, the

all-vanadium (all-V) RFB uses two soluble vanadium redox pairs that fundamentally preclude cross-contamination of two elements and theoretically provide unlimited cyclability. However, one challenge for the all-V RFB is its high redox material cost, which limits its widespread deployment. It is therefore imperative to find a single low-cost element that could be used in both sides.

The ion-exchange membrane is also attributed to a major portion of internal resistance. To solve this problem, a lot of effort has been spared in developing membrane with improved selectivity and reduced internal resistance. Alternatively, it is possible to reduce cell resistance by modifying the configuration of the flow cell. For example, the membrane-less RFB has been developed for the all-V and H-Br RFBs and both showed substantially reduced internal resistance because of the absence of membrane. However, the current membrane-less RFBs have been built as laminar flow cells, which cannot provide effective separation of two redox species, resulting in low coulombic efficiency^[115-119].

The redox pairs in state-of-the-art RFBs are also dependent on individual metal elements in the periodic table. The number of possible redox pairs for the RFB applications is limited. Recent development of organic redox pairs such as quinone family and redox complexes suggests that the extension of conventional metal ion based redox pairs to organic compound based redox pairs may bring new breakthroughs in the field of RFBs^[120-122]. Therefore, actively exploring new redox pairs especially in organic or complex area may widen the perspective for advanced RFBs.

1.5 Outline of Dissertation

As discussed in the limitations of state-of-the-art RFBs, innovative RFB design is needed to bring about new combinations of two redox pairs with low cost, fast kinetics and the highest possible cell voltage. This dissertation has addressed the objective in three approaches.

Chapter 2 introduces a double-membrane triple-electrolyte flow cell design that allows the combination of redox pairs of different supporting pHs and types of charge. In particular, three RFBs have been proposed and verified including Zn-Ce RFB with high voltage (3.08 V), S-Fe RFB with low redox-material cost (\$0.22/Ah), and Zn-Fe RFB with the balanced choice of high voltage (2.0 V) and low redox-material cost (\$0.73/Ah). Zn-Fe RFB is estimated as the most cost-effective RFB among several notable RFBs including all-V, Cr-Fe, quinone-Br, and membrane-less H-Br RFB and has an overall capital cost under \$100/kWh.

Chapter 3 describes a conventional single-membrane setup with two soluble redox pairs based on a single element—iron. Using the same element on both sides of membrane theoretically precludes the cross-contamination of ions. The use of an inexpensive element, iron, potentially yields an RFB with low cost. Built on different coordination chemistries of Fe(III)/Fe(II), the all soluble all-Fe RFB provides an appropriate cell voltage (1.30 V) and shows decent durability and performance.

Chapter 4 studies a novel membrane-less RFB based on immiscible organic-inorganic electrolytes. The natural stratification of two immiscible electrolytes provides a thermodynamically stable method for the separation of two redox pairs. The example demonstrated in Chapter 4, the Zn/Ferrocene RFB, involves Zn^{2+}/Zn in an aqueous phase and ferrocenium/ferrocene in a butyl acetate phase. The successfully

demonstrated membrane-less RFB built on immiscible organic-inorganic electrolytes provides another promising approach to construct new RFBs.

Chapter 5 summarizes the work and reiterates the aim of this dissertation, which is to explore alternative ways to build novel RFBs instead of improving existing ones. Perspectives on developed RFBs have been discussed and some promising approaches have been recommended for future work.

Chapter 2

DOUBLE ION-EXCHANGE MEMBRANE DESIGN FOR REDOX FLOW BATTERIES

2.1 Introduction

In the conventional RFB design, a single membrane was implemented to separate two redox pairs of the same charge while maintaining ionic conduction between positive and negative sides. For example, in the original Cr-Fe RFB, one anion-exchange membrane (AEM) was used to isolate the $\text{Cr}^{3+}/\text{Cr}^{2+}$ pair from the $\text{Fe}^{3+}/\text{Fe}^{2+}$ pair to prevent self-discharge; at the same time, it allows the conduction of the non-electroactive anions (e.g., Cl^- in hydrochloric acid solution) to balance the charges between two electrolytes. Similarly, one cation-exchange membrane (CEM) can work for a cell with two anion redox pairs. However, neither one single AEM nor one single CEM can effectively prevent the mixing of redox pairs with mixed ion charges [20, 27, 123, 124], in spite that some of these mixed ion pairs can lead to RFBs with potentially higher performance and lower cost, as shown in Figure 1.2. Although appreciable effort has been made in researching charge-mixed ion pairs separated by a single membrane (i.e., AEM, CEM, or non-ion-selective porous membrane), the overall efficiency of these RFBs are limited. Examples of charge-mixed ion pairs

Part of Chapter 2 is reprinted from *Energy & Environ. Sci.*, **2015**, DOI: 10.1039/C5EE02315G, and *Energy & Environ. Sci.*, **2014**, 7, 2986-2998. See Appendix C for permission.

separated by a single membrane (AEM, CEM, or non-ion-selective porous membrane) include a RFB with cation/cation negative pair (*e.g.*, V^{3+}/V^{2+}) and anion/anion positive pair (*e.g.*, $ClBr_2^-/Br^-$)^[20, 124], *e.g.*, V-Br RFB. The reported efficiency was far below the state-of-the-art level (non-ion-selective porous membrane: 38–56%; single AEM: 36%; single CEM: 27%–66%, although the redox pairs and test conditions were somewhat different).

Alternatively, a bipolar-IEM (one side being AEM and the other being CEM with no gap in between) was introduced by K.Y. Chan and his co-workers in a semi-RFB in early 2013, using a non-flow metal hydride negative electrode combined with a flow vanadium positive electrode.^[125, 126] The bipolar IEM cell configuration can in principle isolate redox pairs of different charges, but the charge communication between the two electrolytes is limited by water dissociation inside the bipolar membrane, *i.e.*, high current density operation is subject to a substantial voltage penalty^[127-130]. In addition, electrolyte selection is also limited, since protons (H^+) and hydroxide ions (OH^-) are required to be the charge carriers in the bipolar-IEM (H^+ for the CEM side and OH^- for the AEM side)^[131, 132]. On the other hand, it is known in the electro dialysis industry that coupling one AEM and one CEM with a middle electrolyte in between effectively separates ions with mixed charges and also provides efficient charge communication between the two electrolytes^[133]. The charge carriers in a double-IEM are not limited to protons and hydroxide ions, thus eliminating the limitations in electrolyte selection faced by the bipolar-IEM cell configuration. In addition, the double-IEM cell configuration has also been introduced in traditional rechargeable batteries^[130, 134]. These successes suggest the feasibility of introducing

multiple IEMs with middle electrolyte(s) in RFBs with redox pairs of mixed charges for both redox ion isolation and electrolyte charge communication.

In this chapter, a general multiple-IEM RFB cell design that can accommodate any redox pair combinations of mixed ion charges for both the negative and the positive pairs is introduced^[135]. Composed of one AEM, one CEM, and a middle electrolyte in between, the double-IEM cell configuration allows for redox pairs with all combinations of ion charges except that of two hybrid pairs (i.e., an anion-cation pair vs. another anion-cation pair). For the case of two hybrid pairs, a triple-IEM cell configuration with three membranes (CEM/AEM/CEM or AEM/CEM/AEM) and two middle electrolytes is needed. The multiple-IEM (double-IEM and triple-IEM) designs bring unprecedented freedom to the redox pairs and electrolytes, and three aqueous RFBs are featured and demonstrated here: (i) **the ultra-high voltage zinc-cerium RFB** with standard cell voltage of 3.08 V ($\text{Zn(OH)}_4^{2-}/\text{Zn}$ anion redox pair combined with $\text{Ce}_2\text{O}^{6+}/\text{Ce}^{3+}$ cation redox pair); and (ii) **the ultra-low material cost sulfur-iron RFB** with 1.22 V of standard cell voltage ($\text{S}_4^{2-}/\text{S}_2^{2-}$ anion redox pair combined with $\text{Fe}^{3+}/\text{Fe}^{2+}$ cation redox pair), with two highly-abundant elements (iron and sulfur are the, 1st and 5th most produced element worldwide); and (iii) **the high-voltage and low-cost zinc-iron RFB** with 1.99 V of standard cell voltage ($\text{Zn(OH)}_4^{2-}/\text{Zn}$ anion redox pair combined with $\text{Fe}^{3+}/\text{Fe}^{2+}$ cation redox pair), with two low cost elements.

2.2 Working Principle of Multiple-membrane RFB

The double-IEM RFB is shown in Figure 2.1a, consisting of a CEM, an MX solution (middle electrolyte), and an AEM sequentially placed between the negative and positive electrodes. The working principle of the double-IEM configuration is

illustrated in Figure 2.1b, for the RFB combination of an anion/anion redox pair vs. a cation/cation redox pair, represented by $A_N^{2-}/A_N^-||C_P^{2+}/C_P^+$ (the double vertical lines representing the double-IEM). Note that single-electron redox reactions were assumed for all redox reactions for simplicity. M^+ and X^- denote non-electroactive balancing ions. When the cell is being charged, A_N^- are reduced into A_N^{2-} at the negative electrode and C^+ are oxidized into C^{2+} at the positive electrode. Meanwhile, M^+ cations cross the CEM from the middle electrolyte to the negative electrolyte, and X^- anions pass the AEM from the middle electrolyte to the positive electrolyte. During the charging process, the concentration of MX decreases in the middle electrolyte. When the cell is being discharged, the opposite processes occur. If a cation/cation pair is used in the negative electrolyte and an anion/anion redox pair in the positive electrolyte, the IEM sequence needs to be reversed from CEM-middle electrolyte-AEM to AEM-middle electrolyte-CEM.

The double-IEM configuration can also be applied to RFBs with an anion/anion vs. an anion-cation hybrid pair (i.e., anion/cation or cation/anion) or a cation/cation pair vs. an anion-cation hybrid pair. Taking anion/anion pair vs. cation/anion hybrid pair (e.g., the aforementioned $Cr(edta)^-/Cr(edta)^{2-}$ vs. $Cr(edta)^+/Cr(edta)^-$) as an example, the AEM can block the electroactive cation of the cation/anion hybrid pair and allow its balancing anion (X_p^-) as well as the electroactive anion (A_p^-) to pass into the middle electrolyte; and the CEM can prevent those anions from passing into the negative electrolyte. As a result of the double-IEM design, the mixing of electroactive ions is avoided.

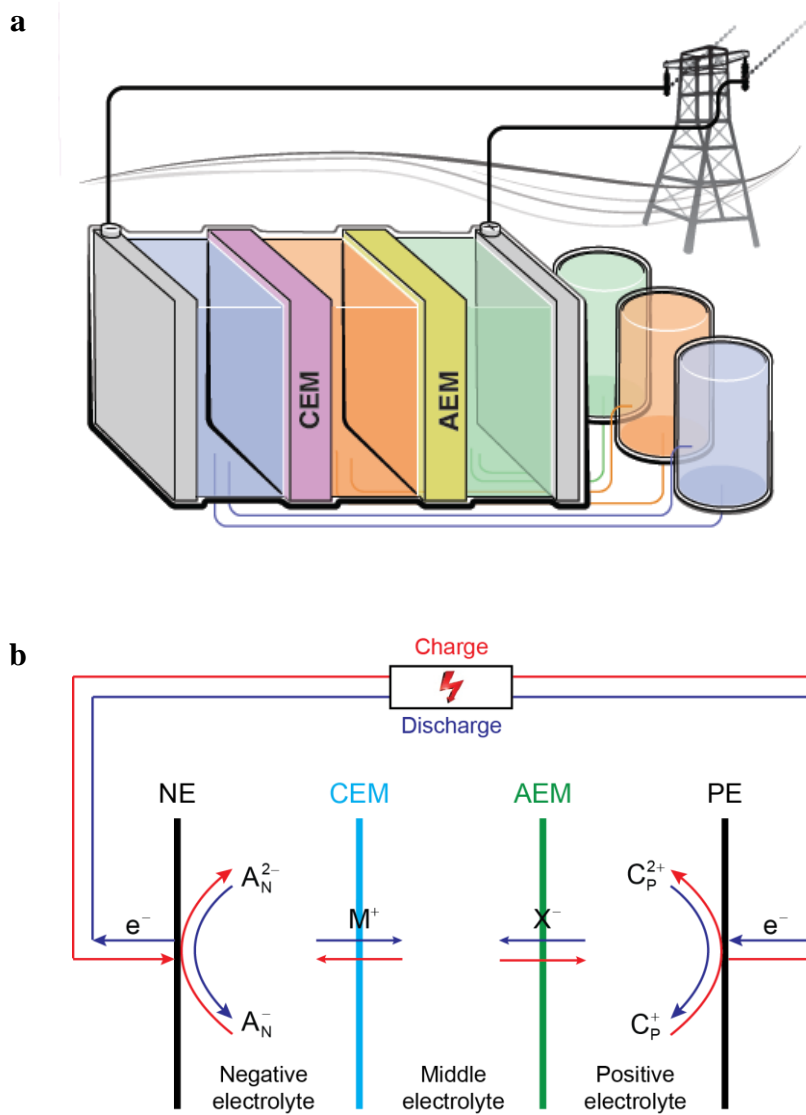
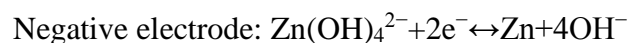


Figure 2.1 (a) Concept schematic. Double-IEM RFB. It consists of two types of IEMs (one CEM and one AEM) and three separate electrolytes (negative, middle, and positive). (b) Working principles of double-IEM RFB cell configuration. NE and PE represent the negative electrode and positive electrode, respectively. Combination of an anion-anion (negative) redox pair (A_N^-/A_N^{2-}) and a cation-cation (positive) redox pair (C_P^{2+}/C_P^+).

Occasionally, redox pairs of mixed charges could be used in RFBs (*e.g.* cation/anion or anion/cation redox pairs). To effectively separate these redox pairs, a triple-IEM RFB should be considered. The triple-IEM RFB consists of either two AEMs plus one CEM, or two CEMs plus one AEM. In practice, however, we have not found combinations of two mixed charged redox pairs that would provide superior properties. In addition, triple-IEM RFB involves three membranes and four electrolytes, greatly adding the challenges in fluid management and control of internal resistance. Thus the triple-IEM configuration was not studied in detailed in this dissertation.

2.3 Zinc-Cerium RFB

The configuration of Zn-Ce RFB is shown in Figure 2.2 and the redox reactions for the positive and negative sides are shown below.



Zn-Ce RFB demonstrates a 3.08-V standard cell voltage by combining the very negative redox potential of $\text{Zn(OH)}_4^{2-}/\text{Zn}$ in base (-1.22 V) ^[28] and the very positive redox potential of $\text{Ce}_2\text{O}^{6+}/\text{Ce}^{3+}$ in acid (+1.87 V) ^[30]. To the best of our knowledge, this cell voltage is the highest among all known aqueous RFBs reported. It is 2.6 times that of the chromium-iron RFB (1.18 V) ^[18], 2.5 times that of the all-vanadium RFB (1.25 V) ^[35], and 2.1 times that of the sulfur-bromine RFB (1.50 V) ^[23]. In this section, a proof-of-concept study of the Zn-Ce RFB successfully demonstrated high cell voltage and cycle performance.

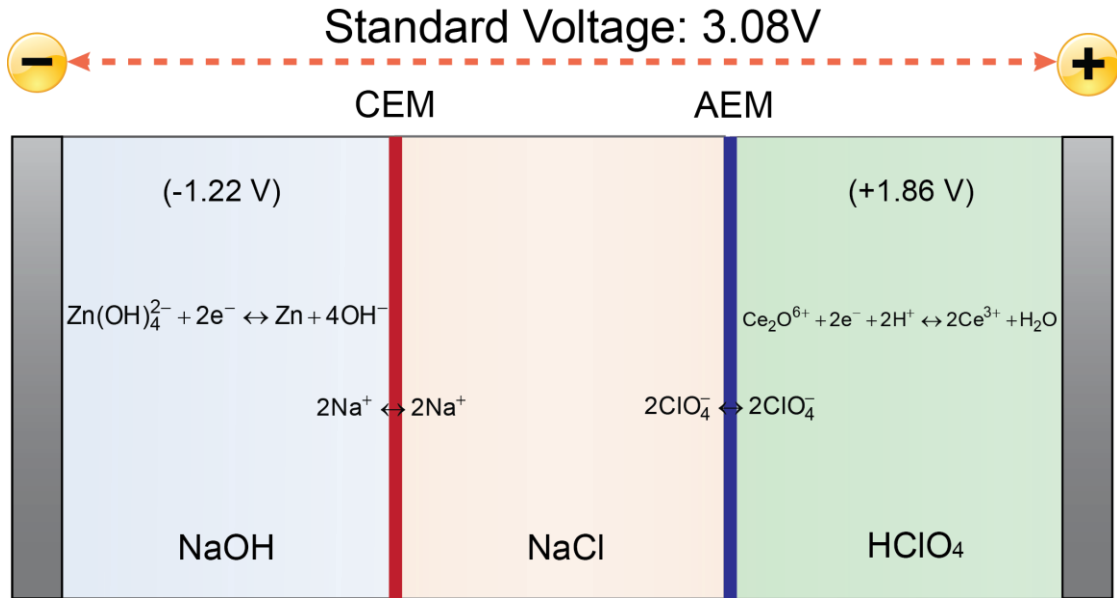


Figure 2.2 Schematic of Zn-Ce RFB. The negative electrolyte is comprised of $\text{Zn(OH)}_4^{2-}/\text{Zn}$ as the negative redox pair and a NaOH solution; The middle electrolyte is a NaClO_4 solution; The positive electrolyte is comprised of $\text{Ce}^{4+}/\text{Ce}^{3+}$ as the positive redox pair and an HClO_4 solution. A cation-exchange membrane (CEM) separates the negative electrolyte and middle electrolyte while an anion-exchange membrane (AEM) separates the middle electrolyte and positive electrolyte. The working principles are as follows. When the cell is being charged, Zn(OH)_4^{2-} anions are reduced to form Zn metal deposits in the negative electrolyte, and Na^+ cations move from middle electrolyte, passing through the CEM, to the negative electrolyte. At the same time, Ce^{3+} cations are oxidized to form Ce^{4+} cations, and ClO_4^- anions move from the middle electrolyte, passing through AEM, to the positive electrolyte. As a result, the NaClO_4 concentration in the middle electrolyte decreases in the charging process. The discharging process is the reverse of the charging process.

2.3.1 Experiment and Method

RFB assembly. The experimental setup of the Zn-Ce RFB consists of three blocks of electrolyte frames, two current collectors, two types of electrodes, two pieces of membranes, and necessary cell accessories such as gaskets, tubes, and pumps (Figure 2.3). Electrolyte frames consist of solid PTFE blocks. The thickness of the recess area on the middle-electrolyte frame is 2.5 mm. Graphite blocks were used as current collectors. Gold-plated copper sheets were used as conductors to connect with battery test station. One piece of carbon felt (Sigracell[®] GFD4.6, 4.6 mm uncompressed) and two pieces of copper mesh (TWP, Inc., 30×30 grid per square inch, 0.5 mm thickness each) were used as the positive and negative electrodes, respectively. Nafion[®] 212 (Ion power, 50 μm) was used as the cation-exchange membrane. A901 (Tokuyama Co., 10 μm) was used as the anion-exchange membrane. All membranes were soaked separately in 3 M NaClO₄ solution for 24 hours and thoroughly washed with DI water to remove residual surface NaClO₄ before use. Both Viton[®] rubber (0.75 mm thickness per piece) and PTFE-coated fiber (0.15 mm thickness per piece) were used as gaskets. Viton rubber was used to contact with graphite block. PTFE-coated fiber was used to contact with the middle electrolyte frame. Eight bolts were torqued to 16 lb ft to tighten the cell and provide firm compression between the electrode and the current collector. The electrolyte was actuated by a peristaltic pump (Cole Parmer, Masterflex[®] L/S 600 rpm) through PTFE-lined rubber tubes (Cole Parmer, ChemDurance[®] #16). The Zn-Ce RFB was then connected to and tested by a commercial battery test station (Arbin, BT2000). All battery test experiments were conducted at room temperature.

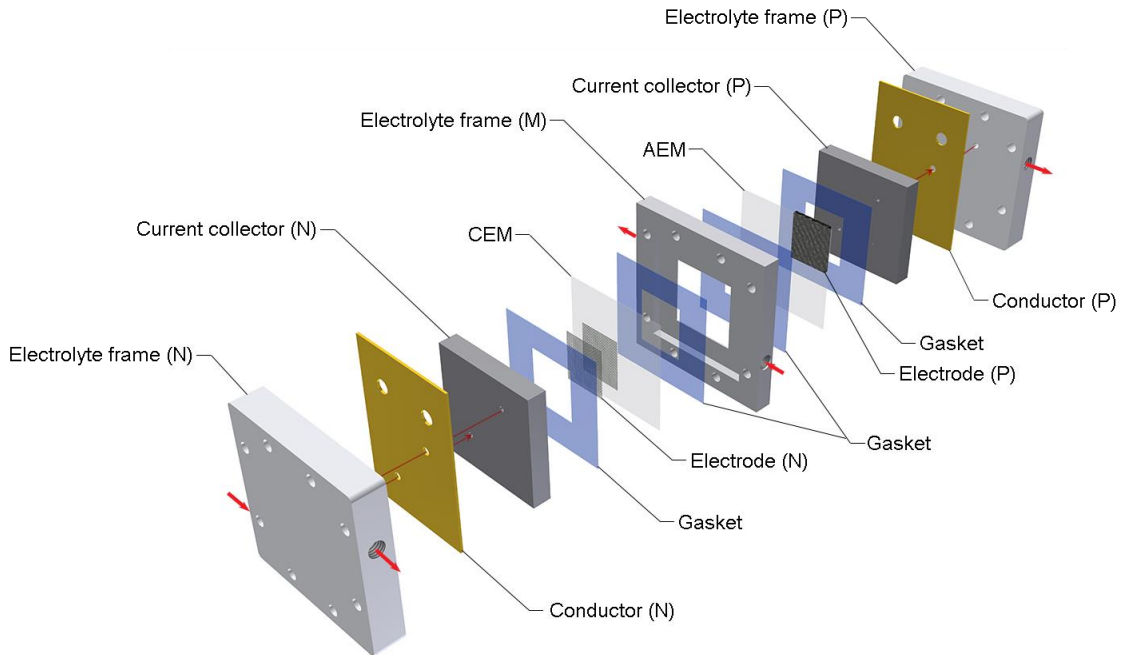


Figure 2.3 Cell configuration of Zn-Ce RFB. The electrolyte flow pathways are shown with red arrows. The electrolytes enter and exit the system through the side holes on the electrolyte frames (thick red arrows). Once into the electrolyte frames, the positive and negative electrolytes flow sideways and through the small holes on the electrolyte frame, conductor, and current collector into the chamber encompassed by gasket and membrane and then return to the electrolyte frames (thin red arrows). The middle electrolyte enters the middle electrolyte frame and then through the tiny hole on the recessed portion of the middle electrolyte frame (not shown in figure) into the open area in the middle electrolyte chamber defined by the two membranes. N, M, and P in parentheses stand for negative, middle, and positive, respectively.

Cycle test. The cycle test of Zn-Ce RFB cell was performed with the following electrolyte compositions: 0.2 M $\text{Ce}(\text{ClO}_4)_3$ in 2.4 M HClO_4 as the positive electrolyte, 3 M NaClO_4 as the middle electrolyte, and 0.2 M $\text{Na}_2[\text{Zn}(\text{OH})_4]$ in 2.6 M NaOH as the negative electrolyte. A volume of 20 mL was used for all electrolytes. The cycle test was carried out while maintaining an SOC swing of 50%. The discharge cut-off

voltage was 1.6 V. During testing, all electrolyte containers were sealed. A flow rate of 100 mL/min was used during the test.

2.3.2 Result and Discussion

A stable open circuit voltage (OCV) of 3.1 V was observed in the basic zinc-acidic cerium RFB (90% of state of charge, SOC, Figure 2.4a) as expected. The observed high, stable OCV validates the double-IEM concept and its capability of effectively coupling redox pairs with mixed ion charges and pH-different electrolytes. Equally importantly, both discharge and charge operations have been conducted (2-hr charge-discharge cycle and 0–75% SOC swing, Figure 2.4b). At a constant current density (20 mA/cm²), the cell voltage smoothly increased from 3.0 V to 3.2 V during a 1-hr charge operation; it smoothly decreased from 2.8 V to 2.7 V after a discharge operation of 57 minutes and then dropped precipitously when the active species had been mostly converted. A round-trip voltage efficiency of 87% was obtained for the entire charge-discharge cycle, and a round-trip coulombic efficiency as high as 96% was also achieved, confirming the excellent redox pair isolation ability of the double-IEM configuration. The overall energy efficiency was close to 82%. In addition, the double-IEM cell is stable, *e.g.*, the overall energy efficiency of the cell remained almost the same during a 40-hr deep cycle test (20 complete cycles with a wide SOC swing of 0–75%, Figure 2.5a).

Note that the high cell voltage of the double-IEM basic zinc-acidic cerium RFB is not compromised by water solvent, as the voltage window of water electrolysis has been largely extended. For a single-IEM RFB, its reversible voltage is limited to 1.23 V (*e.g.*, HER, hydrogen evolution reaction, = 0 vs. OER, oxygen evolution reaction, = +1.23 V at pH = 0, or HER = -0.83 vs. OER = +0.40 V at pH = 14),

because the same pH has to be maintained in both the negative and positive electrolytes. By contrast, a double-IEM cell can have a much larger reversible voltage window of 2.06 V (i.e., HER = -0.83 at pH=14 vs. OER = $+1.23$ V at pH = 0), due to the ability to combine strong-base negative electrolyte and strong-acid positive electrolyte. The double-IEM design also takes advantage of the fact that the overpotential tolerance to the hydrogen evolution side reaction in base is higher than in acid while the overpotential tolerance to oxygen evolution side-reaction is higher in acid than in base.

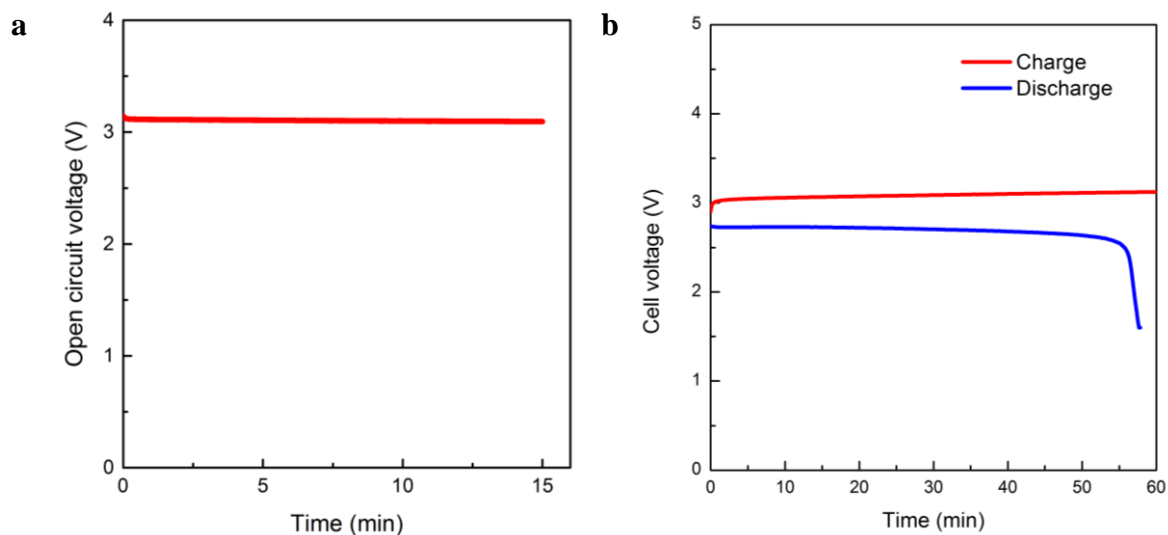


Figure 2.4 (a) Open-circuit voltage (OCV) of Zn-Ce RFB at 90% State of charge (SOC). (b) A full charge-discharge test of Zn-Ce RFB at 20 mA/cm^2 showed 96% coulombic efficiency, 86% voltage efficiency and 83% energy efficiency.

The performance of the Zn-Ce flow battery over 20 cycles with more than 50 mV/cm² power density showed averages of 95.4% coulombic efficiency, 82.2% voltage efficiency and 78.3% energy efficiency. There is no observably significant loss in either efficiency or capacity, as shown in Figure 2.5b, indicating the stability of Zn-Ce RFB over the 20-cycle test.

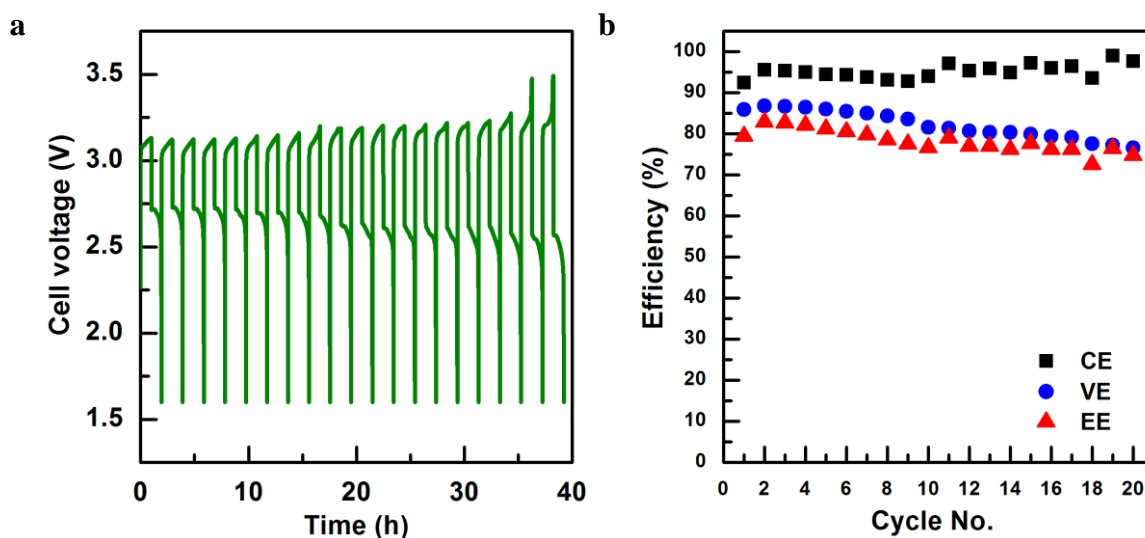


Figure 2.5 (a) 20-cycle test of Zn-Ce RFB at 20 mA/cm². (b) Coulombic efficiency (CE), voltage efficiency (VE) and energy efficiency (EE) for each cycle in 20-cycle test.

Over the long-term cycle test, the durability of the Zn-Ce RFB was found to be a concern, mostly due to the degradation of the AEM in the presence of the highly oxidative and acidic cerium electrolyte. Several commercial membranes have been investigated in this work for their stability in cerium electrolyte, including FAA-2 from Fumatech GmbH, and A901 from Tokuyama Co.; and ASP from AGC Co..

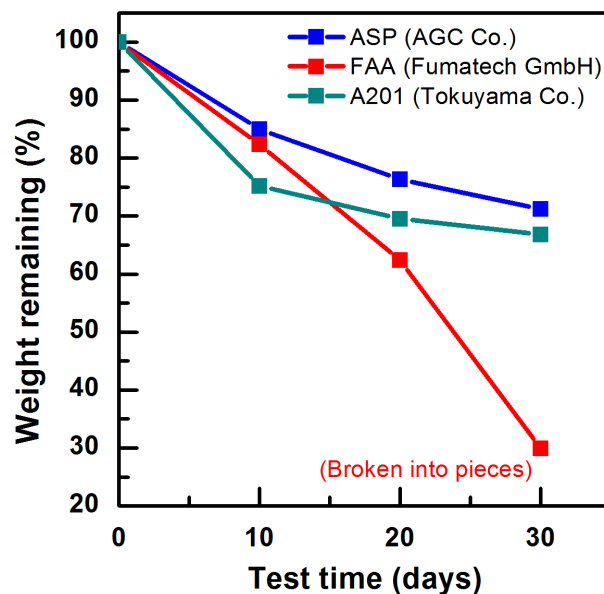


Figure 2.6 Weight remaining of three different AEMs after soaked in Ce(IV) solution (0.5 M $\text{Ce}(\text{ClO}_4)_4$, 1 M HClO_4). FAA-2 membrane broke into several pieces during the transfer of membrane and therefore its remaining weight might be inaccurate.

As shown in Figure 2.6, all membranes showed a significant amount of weight loss, indicating degradation in the cerium electrolyte. A better AEM with enhanced stability in oxidative and acidic environment is needed in order to improve the durability of the Zn-Ce RFB.

2.3.3 Summary of Zn-Ce RFB

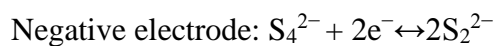
Based on the newly invented double-membrane design, a Zn-Ce RFB with unprecedentedly high cell voltage was demonstrated. The Zn-Ce RFB showed a stable open-circuit voltage as well as expected charge-discharge behavior. Experimental successes fully validated the double-membrane design. However, the high electrode potential of the Ce electrode raises stability concerns of AEM as a challenge to the

long-term durability. Though some effort has been made in exploring better AEMs, no stable AEM has been identified so far. Given this difficulty, alternative redox chemistries should be considered and tested for double-membrane design.

2.4 Sulfur-Iron RFB

In order to overcome the membrane stability issue, alternative redox chemistries have been explored. Sulfur and iron are two elements of interest to us. Polysulfide in a basic solution and iron in an acidic solution have both been used separately in other RFBs. It is evident that both iron and sulfur redox pairs are suitable for flow battery applications. The solubility of $\text{Fe}^{3+}/\text{Fe}^{2+}$ is 2.5 M in 1 M HCl^[53] and that of $\text{S}_4^{2-}/\text{S}_2^{2-}$ is more than 3 M with Na^+ counter ion, and more than 8 M with K^+ as the counter ion^[136]. The $\text{Fe}^{3+}/\text{Fe}^{2+}$ has facile kinetics and shows negligible overpotential even at high current density^[137]. With a modified electrode structure, the S redox reaction has less than 200 mV at 600 mA/cm²^[63], which indicates sufficient kinetics in flow battery applications.

The configuration of the S-Fe RFB is shown in Figure 2.7 and the redox reactions for the positive and negative sides are shown below.



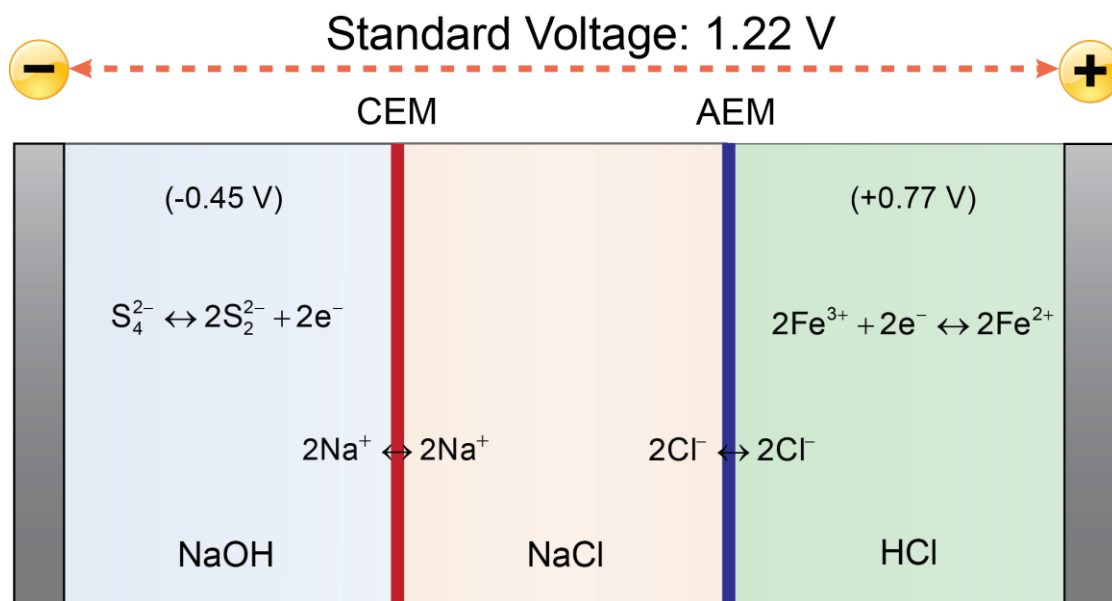


Figure 2.7 Schematic of S-Fe RFB. The negative electrolyte is comprised of S_4^{2-}/S_2^{2-} as the negative redox pair and a NaOH solution; The middle electrolyte is a NaCl solution; The positive electrolyte is comprised of Fe^{3+}/Fe^{2+} as the positive redox pair and an HCl solution. The cell configuration and working principle are similar to those of Zn-Ce RFB described in Figure 2.2.

Choice of S and Fe is largely due to material cost considerations. The S and Fe are the 17th and 4th most abundant elements on Earth and the 5th and 1st most produced material in the world. Employment of earth-abundant elements as energy storage materials would drastically reduce storage capacity based cost, especially in large scale application. The combination of S with Fe would deliver one of the cheapest electrolytes for RFBs.

2.4.1 Experiment and Method

Electrolyte, electrode, and membrane preparation. The 1 M Na_2S_4 in 1 M NaOH negative electrolyte was prepared by dissolving $\text{Na}_2\text{S} \cdot 10\text{H}_2\text{O}$ (Sigma-Aldrich, 99%) and sulfur (Sigma-Aldrich, 99%) into NaOH solution. The mixture was then maintained at 40 °C until fully dissolved. 1 M FeCl_2 in 1 M HCl, the positive electrolyte, was prepared by dissolving $\text{FeCl}_2 \cdot 4\text{H}_2\text{O}$ (Sigma-Aldrich, 99%) into HCl solution. Nickel foam (MTI Corp. 80-110 PPI, 1.6 mm thickness, 10 cm²) was boiled in 1 M Na_2S_4 solution for 30 min and washed with DI water prior to cell assembly. Graphite felt (Sigracell[®] GFD4.6, 4.6 mm, 10 cm²) was used as received from SGL group. The Nafion 212 membrane (Ion power, 50 μm) and FAA-3 (Fumatech, non-reinforced, 45 μm) were soaked separately in 3 M NaCl solution for 24 hours and washed with DI water to remove NaCl solution on surface before used in cell.

Cell assembly. The flow battery cell configuration is the same as that in the Zn-Ce RFB, shown in Figure 2.3. The as-treated nickel foam and carbon felt were used as the negative and positive electrodes, respectively. A total of 3.75 mm gasket thickness was used on the positive side in order to maintain a 20% compression rate of graphite felt.

OCV and cycle test. The assembled flow cell was tested under constant current with a battery test station (Arbin, BT2000). For the OCV test, the flow cell was charged to 50% state of charge (SOC), after which the OCV was monitored for 48 hours. The cycle test was carried out by setting charged capacity constant (225 mAh) to maintain a 70% SOC swing and discharge cut-off voltage at 0.6 V. The initial electrolyte volume for all electrolytes is 12 ml. During testing, all electrolyte containers were sealed and the negative electrolyte was maintained at 40 °C via a water bath in order to improve kinetics. 3 ml of 5 M HCl and 5 M NaOH were added

into positive and negative side every 24 hours. A flow rate of 50 mL/min was used during the test.

Polarization test. The polarization curve was obtained at 50% SOC. The cell was discharged at a particular current density for 30 s and the final voltage was used in the polarization curve. In order to maintain the same SOC, after each discharge test, the cell was charged for 30 s and left idle for 30 s before the next discharge test.

2.4.2 Result and Discussion

Figure 2.8a shows the open circuit voltage at 70% state of charge over 48 hours. The OCV is stable between 1.238 V and 1.218 V. In contrast to the all-vanadium RFB using Nafion, whose OCV generally drops within 20 hours with less membrane exposure area^[138], here, the extended OCV holding time without a large drop indicates that the double-membrane triple-electrolyte design well prevents ion crossover.

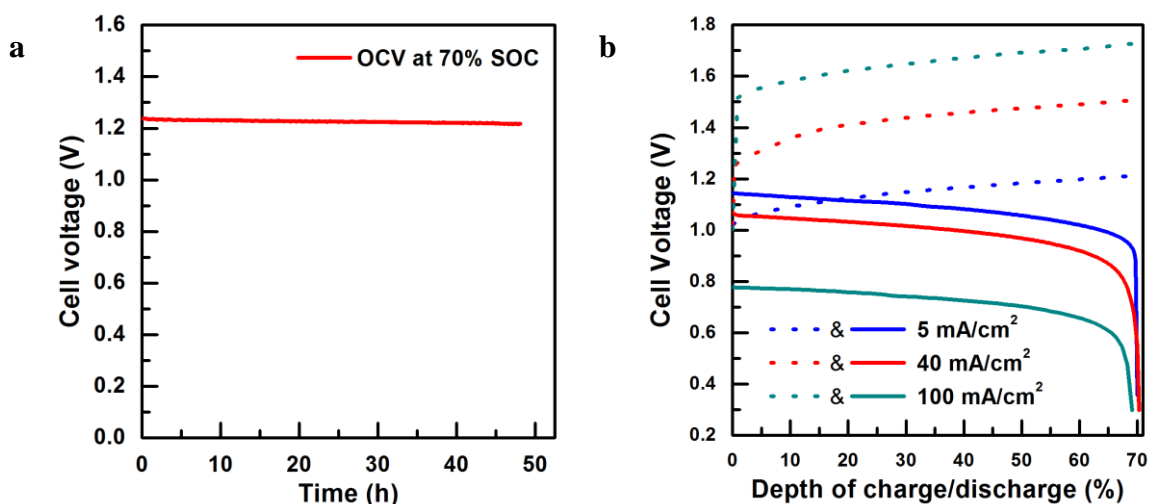


Figure 2.8 (a) Open-circuit voltage (OCV) of S-Fe RFB at 70% State of Charge (SOC). (b) Charge-discharge test of S-Fe RFB with 70% SOC swing at different current densities.

The cycle tests at 5 mA/cm², 40 mA/cm² and 100 mA/cm² were shown in Fig 2.8b. As the current density increases, the voltage efficiency decreases (94%, 70%, and 44% respectively) due to larger voltage losses from internal resistance and overpotential. The coulombic efficiency remained at 100% both at 5 mA/cm² and 40 mA/cm² but decreases to 98% when current density reaches 100 mA/cm². The coulombic efficiency at high current densities is not caused by crossover but rather by insufficient transport and kinetics when the concentration of remaining active species is low; the cell could still discharge at low current densities until coulombic efficiency reaches 100%.

The as-expected OCV and charge-discharge results at different current densities show the new S-Fe RFB is fully functional by a double-membrane triple-electrolyte configuration and is able to operate at 40 mA/cm² with acceptable efficiency.

The polarization curve of S-Fe flow battery at 50% SOC is shown in Figure 2.9a. A peak power density of 94 mW/cm² was achieved. Considering economical operation warrants at least 70% round-trip efficiency, the practical current density should be less than 40 mA/cm², which yields a power density of 41 mW/cm². Figure 2.9b shows the divided voltage loss from the positive and negative electrodes, as well as the cation and anion exchange membranes. The overpotential of Fe is negligible even at high current density. The negative electrode shows 45 mV discharge overpotential at 200 mA/cm². Though a more advanced catalyst for polysulfide redox

reaction is necessary in order to operate at higher current density, the catalytic effect of treated nickel foam is good enough for RFB operation at normal current density. The major voltage loss comes from internal resistance. The tested S-Fe RFB has an estimated resistance of $3.7 \Omega \cdot \text{cm}^2$. The low standard voltage combined with large internal resistance hinders the high power density and high voltage efficiency at high current density.

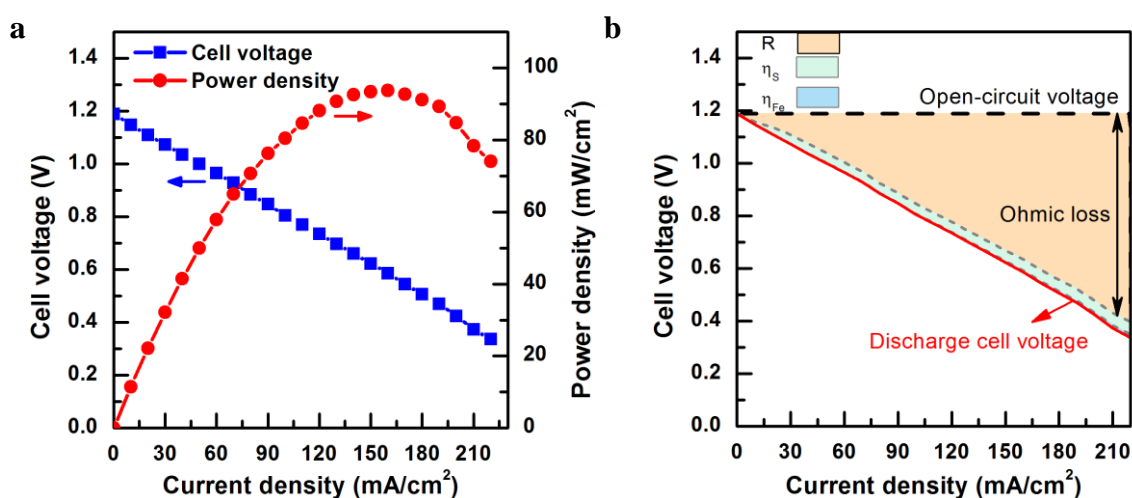


Figure 2.9 (a) Polarization curve of the S-Fe RFB at 50% SOC. (b) Analysis of cell voltage loss during discharging process. The orange part represents voltage loss from ohmic resistance.

A 100-cycle test was carried out to test the long-term durability of the S-Fe RFB. The result is shown in Figure 2.10. The CE remained close to 100% over 100 cycles, and discharge capacity also stayed constant, indicating excellent prevention of crossover. Comparing with the all-vanadium RFB, in which the capacity decay during operation is a widely reported phenomenon and the capacity fading rate could be

larger than 50% within 50 cycles^[139, 140], the S-Fe RFB has better retention of capacity, potentially requiring less effort in crossover management and electrolyte balance. The voltage efficiency gradually decreases due to increased membrane resistance that is mainly caused by membrane fouling. The negatively charged ferric chloride complex (FeCl_4^- , FeCl_6^{3-}) formed in ferric chloride solution is able to block the channels within the anion exchange membrane, thereby increasing membrane resistance. The crossover of iron ion into middle electrolyte was also measured with Inductively Coupled Plasma Optical Emission Spectrometry (ICP-OES) after long term cycle test. The concentration of iron in the middle electrolyte was only 293 ppm, which again supports the low crossover feature of the double-membrane, triple-electrolyte design.

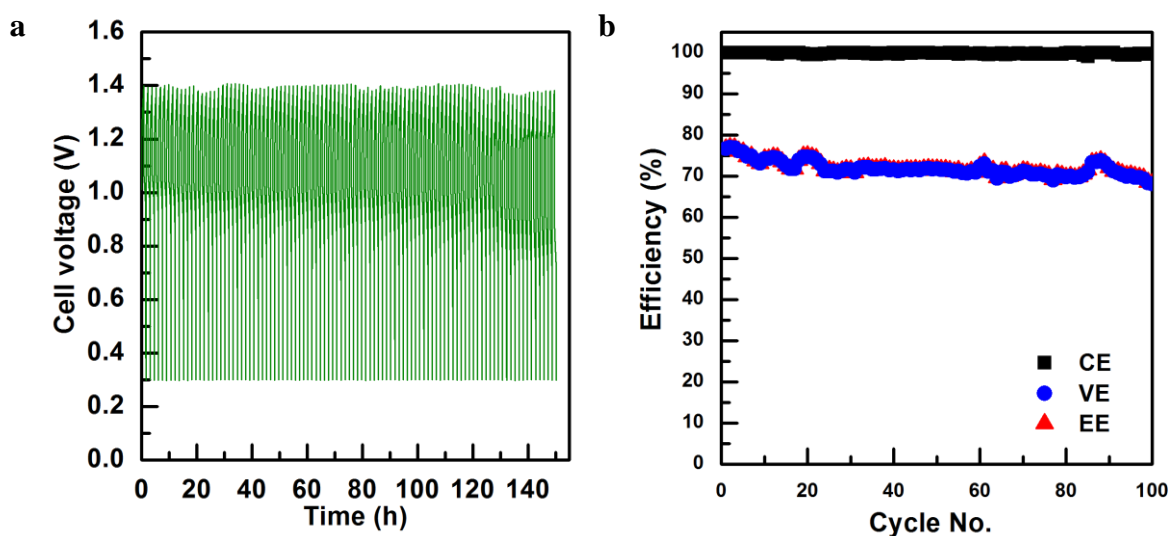


Figure 2.10 (a) 100-cycle test of S-Fe RFB at 30 mA/cm^2 . During the cycle process, certain amounts of acid and base was added into positive and negative electrolytes to sustain the appropriate pH for each electrolyte. (b) Coulombic efficiency (CE), voltage efficiency (VE) and energy efficiency (EE) for each cycle in 100-cycle test.

2.4.3 Summary of S-Fe RFB

The new S-Fe RFB system showed excellent performance in terms of low crossover and high coulombic efficiency. Analysis of the voltage loss and internal resistance showed they were similar to those in conventional redox flow batteries. Long term cycle test showed good system stability and capacity retention. The earth abundant element based system offers remarkable reduction of energy capacity based cost compared with the All-V RFB. Remaining challenges for the S-Fe RFB are the low cell voltage and high internal resistance. The cell voltage is determined by thermodynamics of the system and can hardly be modified. Should the internal resistance be reduced dramatically, S-Fe RFB still holds the potential to bring high performance and low capital cost. The successful demonstration of the S-Fe RFB showed double-membrane, triple-electrolyte configuration could be elegantly used to explore new chemistries and develop new flow batteries with attractive features.

2.5 Zinc-Iron RFB

As mentioned earlier in the introduction, a low-cost RFB calls for low-cost redox materials and high effective voltage at high current densities. Though Zn-Ce RFB has the highest voltage among all aqueous RFBs, the element Ce is not inexpensive. On the other hand, S-Fe RFB has very attractively low redox material cost, but its low standard voltage preclude it from delivering high effective voltage at high current densities.

Zn and Fe are two elements with the potential to satisfy these low cost requirements. Specifically, use of Zn in a basic environment and Fe in an acidic environment has been seen in many RFBs due to their low elemental cost, facile redox kinetics, and desirable standard potentials ($\phi_{\text{Zn(II)}/\text{Zn}} = -1.22 \text{ V vs. SHE in base, pH} =$

14; and $\phi_{\text{Fe(III)/Fe(II)}} = 0.77 \text{ V vs. SHE in acid, pH} = 0$)^[141, 142]. In addition, the long-standing concern of Zn dendrite formation is precluded by the flowing electrolyte in RFBs.^[143] Each of the two redox pairs has been separately used in the construction of many promising RFBs^[141, 142, 144]. In this work, the Zn-Fe RFB is fabricated using a double-membrane design that enables the use of redox pairs of different ion charges and supporting electrolytes of different pHs^[135]. The working principles of the Zn-Fe RFB based on the basic Zn redox pair and acidic Fe redox pair are illustrated in Figure 2.11, and the negative and positive electrode reactions are shown below^[145].

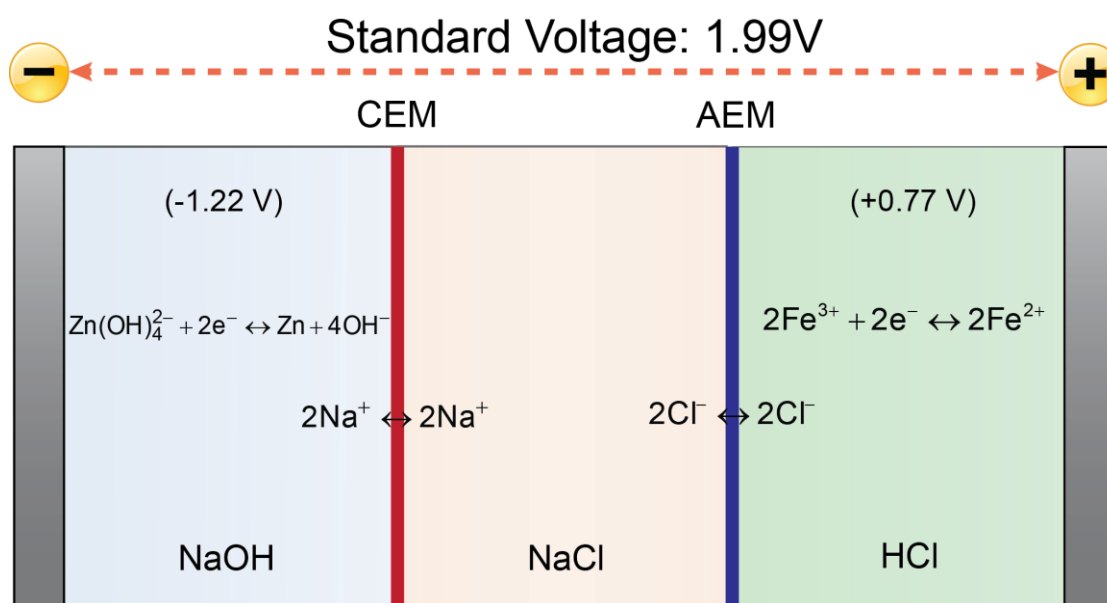
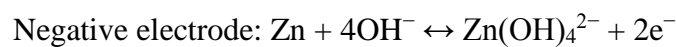


Figure 2.11 Schematic of the Zn-Fe RFB. The negative electrolyte is comprised of $\text{Zn(OH)}_4^{2-}/\text{Zn}$ as the negative redox pair and a NaOH solution; The middle electrolyte is a NaCl solution; The positive electrolyte is comprised of $\text{Fe}^{3+}/\text{Fe}^{2+}$ as the positive redox pair and an HCl solution. The cell configuration and working principle are similar to those of the Zn-Ce RFB described in Figure 2.2.

The combination of the Zn redox pair in base and the Fe redox pair in acid has the potential to achieve very low system capital cost: 1) Both Zn and Fe are inexpensive elements, *i.e.*, $\text{\$}0.13/\text{Ah}$ (half-cell) for Fe and $\text{\$}0.20/\text{Ah}$ (half-cell) for Zn (see Appendix B for calculation). Overall, a Zn-Fe RFB requires an electrolyte cost (U_e) of only $\text{\$}0.73/\text{Ah}$ (full-cell), which is one order of magnitude smaller than that of all-V RFBs ($\text{\$}8.10/\text{Ah}$, full-cell). 2) The combination of the $\text{Zn}(\text{OH})_4^{2-}/\text{Zn}$ redox pair in base and the $\text{Fe}^{3+}/\text{Fe}^{2+}$ redox pair in acid provides a high standard cell voltage of 1.99 V and also offers a wide electrochemical window of 2.06 V for water splitting (-0.83 V of hydrogen evolution at $\text{pH} = 14$ and 1.23 V of oxygen evolution at $\text{pH} = 0$). 3) Both $\text{Zn}(\text{OH})_4^{2-}/\text{Zn}$ and $\text{Fe}^{3+}/\text{Fe}^{2+}$ redox pairs have facile kinetics, with standard rate constants (k^0), of 2.5×10^{-4} cm/s for the former and 1.2×10^{-4} cm/s for the latter^[146]. The magnitudes of these standard rate constants yield very small electrode overpotential even at high current density. The attractive features of Zn and Fe redox pairs promise an RFB with the best balance between high voltage and low redox material cost.

2.5.1 Experiment and Method

RFB assembly. The experimental setup of the Zn-Fe RFB is similar to that of Zn-Ce RFB as shown in Figure 2.3. One piece of carbon felt (Alfa Aesar, 3.1 mm uncompressed) and two pieces of copper mesh (TWP, Inc., 30×30 grid per square inch, 0.5 mm thickness each) were used as the positive and negative electrodes, respectively. Either Nafion[®] 212 or 211 (Ion power, 50 and 25 μm respectively) was used as the cation-exchange membrane. Either FAA-3 (Fuma-Tech, 45 μm) or A901 (Tokuyama Co., 10 μm) was used as the anion-exchange membrane. All membranes

were soaked separately in 3 M NaCl solution for 24 hours and thoroughly washed with DI water to remove residual surface NaCl before use.

Measurements of cell resistance and electrode overpotential. Solutions of 1 M FeCl₂ in 1 M HCl, 3 M NaCl, and 0.5 M Na₂[Zn(OH)₄] in 4 M NaOH were used as the initial positive, middle, and negative electrolytes, respectively. The battery was charged to 50% SOC prior to measurements of cell resistance and electrode overpotential. The middle electrolyte concentration was 2.5 M at 50% SOC. Nafion[®] 212 and FAA-3 were used as the CEM and AEM, respectively, in cell resistance studies. An Ag/AgCl reference electrode was immersed into positive (or negative) electrolyte to measure the positive (or negative) electrode potential; the electrode overpotential for a given current density was obtained by comparing the charge/discharge potential with open circuit potential. The cell resistance was obtained by dividing the potential difference between the two Ag/AgCl reference electrodes (one in negative electrolyte and the other in positive electrolyte) by the applied charge/discharge cell current. Conditions sampled were flow rates of 0–400 mL/min and current densities of 10–200 mA/cm². Resistances measured in the charging process were used for data analysis.

Polarization test. The polarization of the Zn-Fe RFB cell was tested with the same initial electrolyte compositions but at 70% SOC. A Nafion[®] 211 membrane and an A901 membrane were used as CEM and AEM, respectively. A plastic mesh (~3×3 grids per square inch, 0.5 mm thickness) was put into the middle-electrolyte frame to separate the two membranes, to maintain the middle-electrolyte gap at 0.5 mm, and to generate turbulence for improved mass transport. Alternating charge and discharge

current was applied and cell voltage at each current density recorded. A flow rate of 150 mL/min was used during the tests.

Cycle test. The cycle test of Zn-Fe RFB cell was performed with the following electrolyte compositions: 0.6 M FeCl₂ and 0.5 M NaCl in 1 M HCl as the positive electrolyte, 3 M NaCl as the middle electrolyte, and 0.3 M Na₂[Zn(OH)₄] and 0.5 M NaCl in 2.4 M NaOH as the negative electrolyte. A volume of 20 mL was used for all electrolytes. Addition of NaCl to the positive and negative electrolytes minimizes the water transport during the cycle testing. Nafion[®] 212 and FAA-3 were used as the CEM and AEM, respectively, for cycle testing. The first cycle was carried out by charging to a capacity of 240 mAh to maintain an SOC swing of 75%. The ending voltage of the first charge cycle was set as the cut-off voltage for the following 19 cycles; charge and discharge cut-off voltages were 2.3 V and 0.8 V, respectively. During testing, all electrolyte containers were sealed. A flow rate of 100 mL/min was used during the test.

Cost model. The RFB is priced analogously to published methods^[147-149]. In the expression for effective voltage of a single cell (Eq. 1.7), activation overpotential is calculated from the Butler-Volmer equation and internal resistance from the Nernst-Einstein relation. The modeled results are validated against experimental data. To this shunt current losses and pumping losses are added when describing the voltage for the whole system.

For every stack size, then, optimal performance is attained at the flow rate that minimizes the sum of overpotential during each flow-through and pumping loss from the pressure drop due to flow. Using the smallest necessary stack size at its optimal flow rate will in turn minimize capital cost. The stack is sized to meet fixed power and

energy ratings (here, 1 MW and 8 MWh), at each current density within the practical range (*e.g.*, 10–200 mA/cm²). The tanks are sized to meet the electrolyte needs of constant-power discharge. Pricing information is referenced in detail in the Appendix B.

2.5.2 Result and Discussion

The fast kinetics of both redox reactions were confirmed by overpotential measurements. For example, the charge/discharge electrode overpotential is less than 10 mV for the Fe³⁺/Fe²⁺ redox pair (carbon felt electrode) and 40 mV for the Zn(OH)₄²⁻/Zn redox pair (copper mesh electrode), at a current density of 200 mA/cm² (Figure 2.12). The small overpotentials observed in this work are consistent with data reported in the literature^[143, 144].

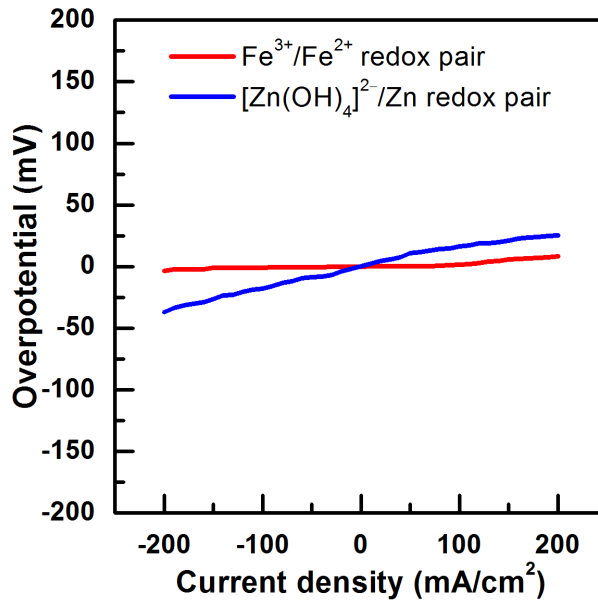


Figure 2.12 Overpotential measured at the zinc electrode (copper mesh) and iron electrode (carbon felt). The charge/discharge electrode overpotential is smaller than 10 mV and 40 mV for $\text{Fe}^{3+}/\text{Fe}^{2+}$ redox pair (carbon felt electrode) and $\text{Zn}(\text{OH})_4^{2-}/\text{Zn}$ redox pair (copper mesh electrode), respectively, at a current density of 200 mA/cm^2 . Overpotential was measured in cell at 50% SOC.

A sufficiently low cell resistance is then the remaining barrier to achieving low cost. Unlike in traditional single-membrane RFBs, the double-membrane design used by the Zn-Fe RFB requires an additional membrane and electrolyte, which adds challenges for managing the cell resistance. Study shows that the total cell resistance consists of two components: ohmic resistance (R_o) mostly from the two membranes and three electrolytes; and concentration-polarization resistance (R_{cp}) caused by insufficient ion diffusion in middle electrolyte^[150]. Specifically, the concentration-polarization resistance originates from the accumulation or depletion of Na^+ and Cl^- ions in the vicinity of either membrane when a current flows through the cell (Figure

2.13a). Compared with OH^- anions (in negative electrolyte) and H^+ cations (in positive electrolyte), the Na^+ cations and Cl^- anions have much smaller ion diffusion coefficients, and as such the middle electrolyte, to a great extent, controls R_{cp} .

R_0 can be managed by optimizing the electrolyte concentration and reducing the thickness of middle electrolyte (Figure 2.14a and 2.14b). With an optimal electrolyte concentration of 2.5 mol/L and a small electrolyte thickness of 0.5 mm, a R_0 as low as $2.3 \Omega \cdot \text{cm}^2$ was obtained, which is sufficiently low for Zn-Fe RFB, considering its close-to-2 V standard voltage. R_{cp} , on the other hand, depends on various structural and operational parameters^[151] (Figure 2.13b). The R_{cp} can be quantitatively measured by subtracting the constant R_0 from total cell resistance obtained at different flow rates and/or different current densities.

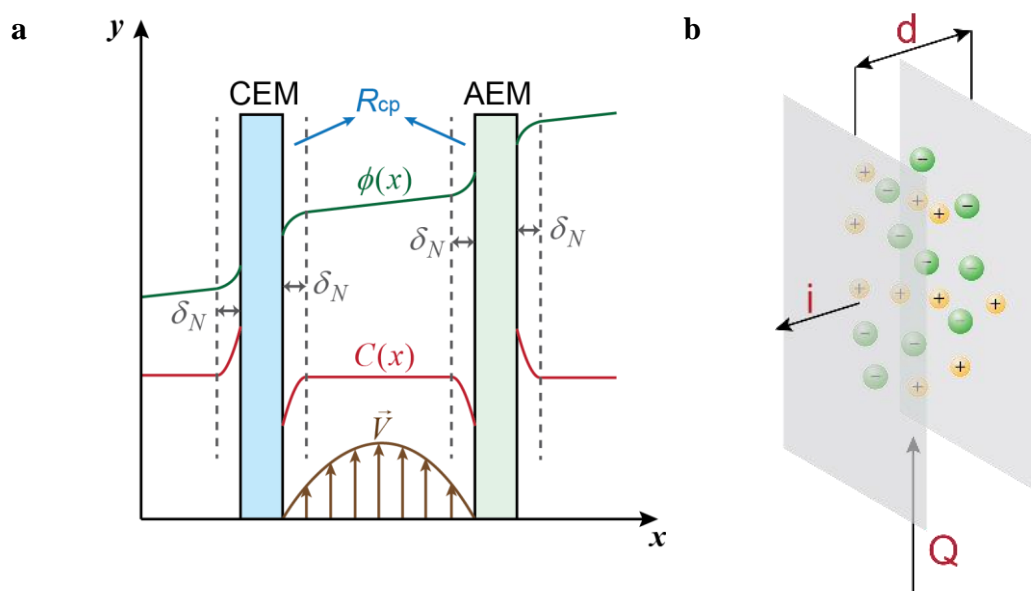


Figure 2.13 Schematics of middle electrolyte in between two membranes (a) Schematic illustrating velocity, concentration, and potential profiles of middle electrolytes during charging process. Φ , C , V and δ_N represent potential, concentration, velocity and Nernstian boundary layer of electrolyte. (b) Schematic illustrating middle electrolyte and three key parameters (thickness, current density and flow rate) that influence the cell resistance.

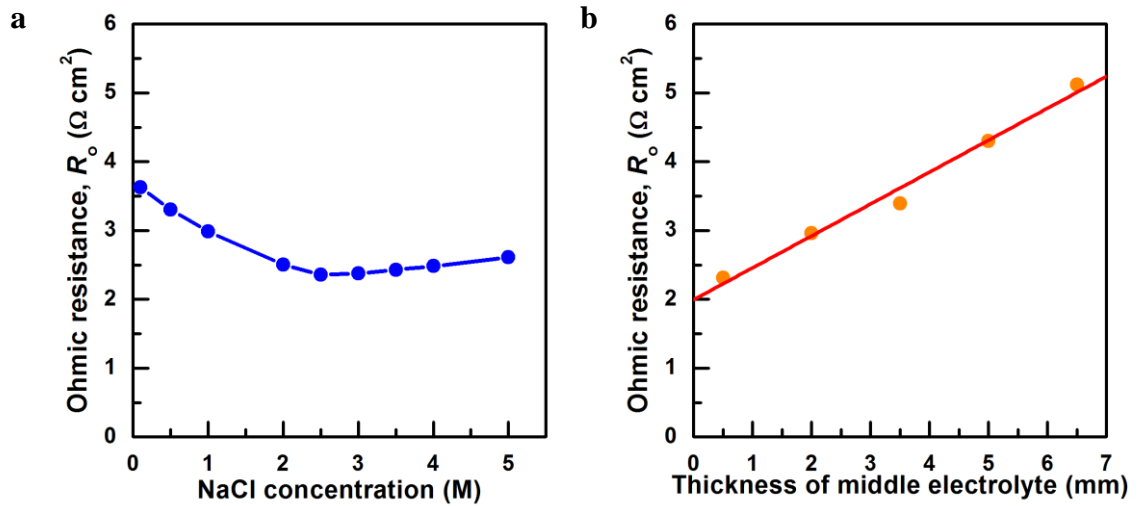


Figure 2.14 The impact of middle electrolyte (thickness and salt concentration) on ohmic resistance. (a) The NaCl concentration vs. ohmic resistance at a middle electrolyte thickness of 0.5 mm. The ohmic resistance firstly decreases with raising NaCl concentration (increasing ionic conductivity of middle electrolyte), and after reaching the minima around 2.5 mol/L it slowly increases with raising NaCl concentration (decreasing ionic conductivity of membranes). The water content in membrane decreases when in contact with highly concentrated salt solution, resulting in lowered ionic conductivity. (b) The thickness of middle electrolyte vs. ohmic resistance at a middle electrolyte NaCl concentration of 2.5 mol/L. Note: in both cases, a low current density of 10 mA/cm² and a high flow rate of 400 ml/min were used to minimize concentration polarization.

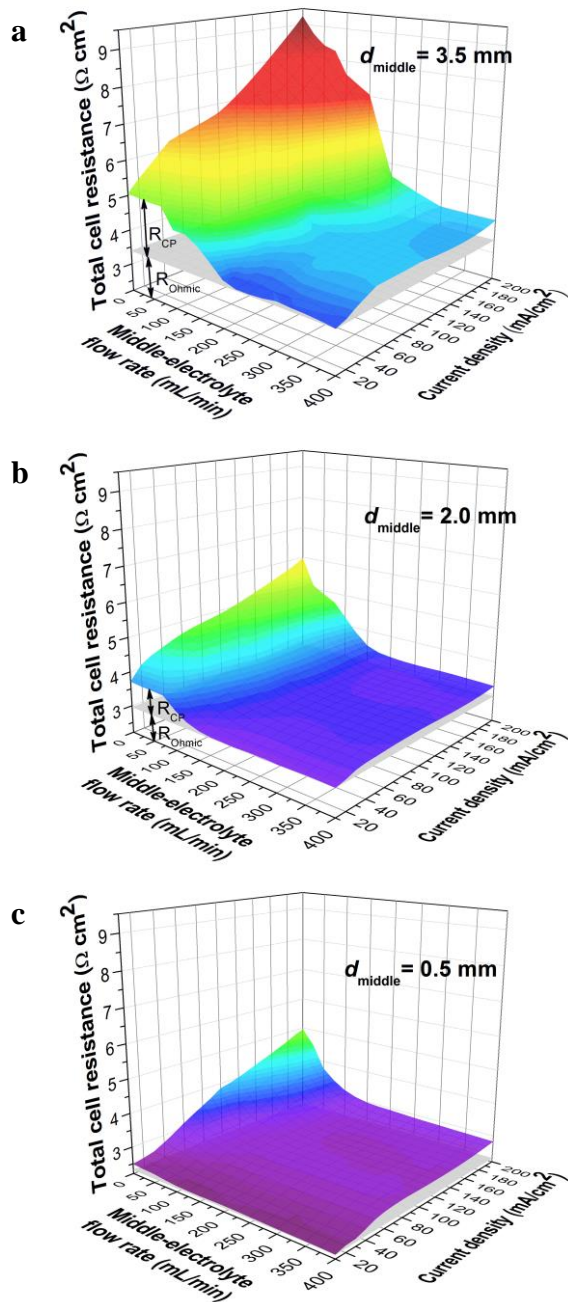
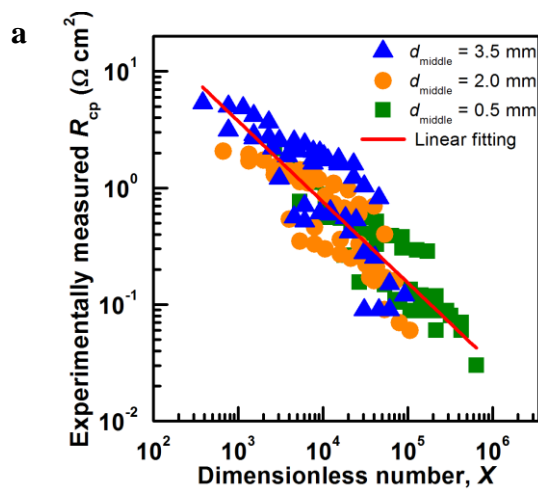


Figure 2.15 The impact of flow rate and current density on measured internal resistance at different middle electrolyte thicknesses. (a) $d_{\text{middle}} = 3.5 \text{ mm}$. (b) $d_{\text{middle}} = 2.0 \text{ mm}$. (c) $d_{\text{middle}} = 0.5 \text{ mm}$.

Figure 2.15 shows the impact of flow rate and current density on R_{cp} with different thicknesses of middle electrolyte (0.5, 2.0, and 3.5 mm). We found that the operational and structural parameters can be correlated to a dimensionless number X characterizing R_{cp} : $X = (Q \cdot d^{-1} \cdot w^{-1}) / (I \cdot F^{-1} \cdot C^{-1})$, where, Q is flow rate; d and w are thickness and width of middle electrolyte, respectively; I is current density; F is Faraday's constant; C is the salt concentration of middle electrolyte. The quantity X represents the ratio of vertical velocity of convection (direction of electrolyte flow) to horizontal velocity of ion diffusion (direction of current flow). From regression analysis, increasing X can effectively depress R_{cp} to a negligible level (Figure 2.16a). This relationship illustrates the general resistance behavior with respect to cell structural and operational parameters. The theoretically calculated R_{cp} also has a similar trend with respect to the dimensionless number X (Figure 2.16b and 2.16c), as compared with measured R_{cp} . Both results show that R_{cp} can be limited to around $0.1 \Omega \cdot \text{cm}^2$ if X is larger than 10^5 , suggesting that manipulation of cell structural and operational parameters is effective to minimize R_{cp} .



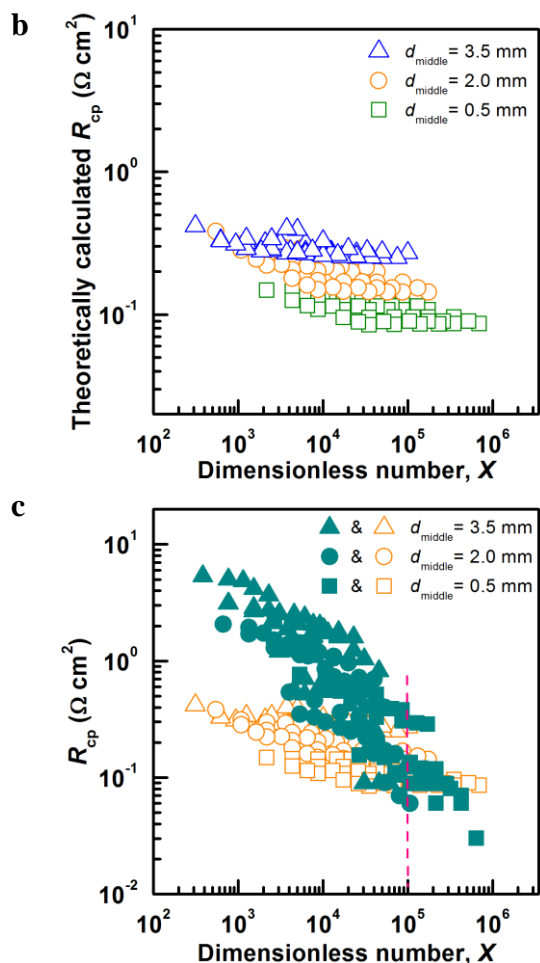


Figure 2.16 Experimentally measured and theoretically calculated R_{cp} as a function of dimensionless number X . (a) Experimentally measured R_{cp} as a function of dimensionless number X and linear fitting on log-log scale. Linear fitting of $\log X$ vs. $\log R_{cp}$ shows a slope of -0.7 , *i.e.*, as $R_{cp} \propto X^{-0.7}$. (b) Theoretically calculated R_{cp} as a function of dimensionless number X . We calculated R_{cp} considering contributions from 1) the potential difference through the Nernst boundary layer in electrolyte adjacent to ion-exchange membrane and 2) the potential difference from the Donnan equilibrium across ion-exchange membranes (detailed in Appendix A, Calculation Method). (c). Comparison between theoretically calculated R_{cp} (empty symbols) and experimentally measured R_{cp} (filled symbols) with respect with the dimensionless number X .

Both measured and calculated R_{cp} data have similar trend with respect with the dimensionless number X . It should be noted that the scaling law only roughly captures the trend of R_{cp} with X in both experiment and theory. The discrepancy at small X between experimentally measured and theoretically calculated R_{cp} is possibly due to the pressure differences between the middle electrolyte and the other two electrolytes. This pressure difference may cause the shape of the membranes to change from being flat to bent, consequently causing uneven flow distribution and extra R_{cp} . The theoretically calculated R_{cp} does not capture this effect and only illustrates the ideal scenario.

With an engineered middle electrolyte, Zn-Fe RFB achieves high performance (Figure 2.17). A peak power density of 676 mW/cm^2 was delivered during discharge at a current density of 660 mA/cm^2 (70% of SOC, Figure 2.17a). This peak power density is the highest among all RFBs based on zinc ($\sim 200 \text{ mW/cm}^2$ for Zn-Br RFB to our best estimation^[152]) or iron (257 mW/cm^2 for H-Fe RFB^[144]) and among the highest among advanced RFBs including quinone-Br RFB (600 mW/cm^2)^[153], all-V RFB ($1,300 \text{ mW/cm}^2$)^[74], and H-Br RFB ($1,450 \text{ mW/cm}^2$)^[154]. In addition, even at $I=600 \text{ mA/cm}^2$, V_{eff} remains at 1.1 V, which is comparable to V_{rev} of some of the most advanced RFBs. Zn-Fe RFBs also showed a very high coulombic efficiency of 99.9% regardless of current density (Figure 2.17b), indicating excellent isolation of two redox pairs, owing to the double-membrane cell configuration. In addition, the Zn-Fe RFB showed no decrease for coulombic efficiency (99.9%), voltage efficiency (76%) and capacity after 20 cycles at 80 mA/cm^2 current density with 75% state of charge (SOC) swing (Figure 2.17c and 2.17d).

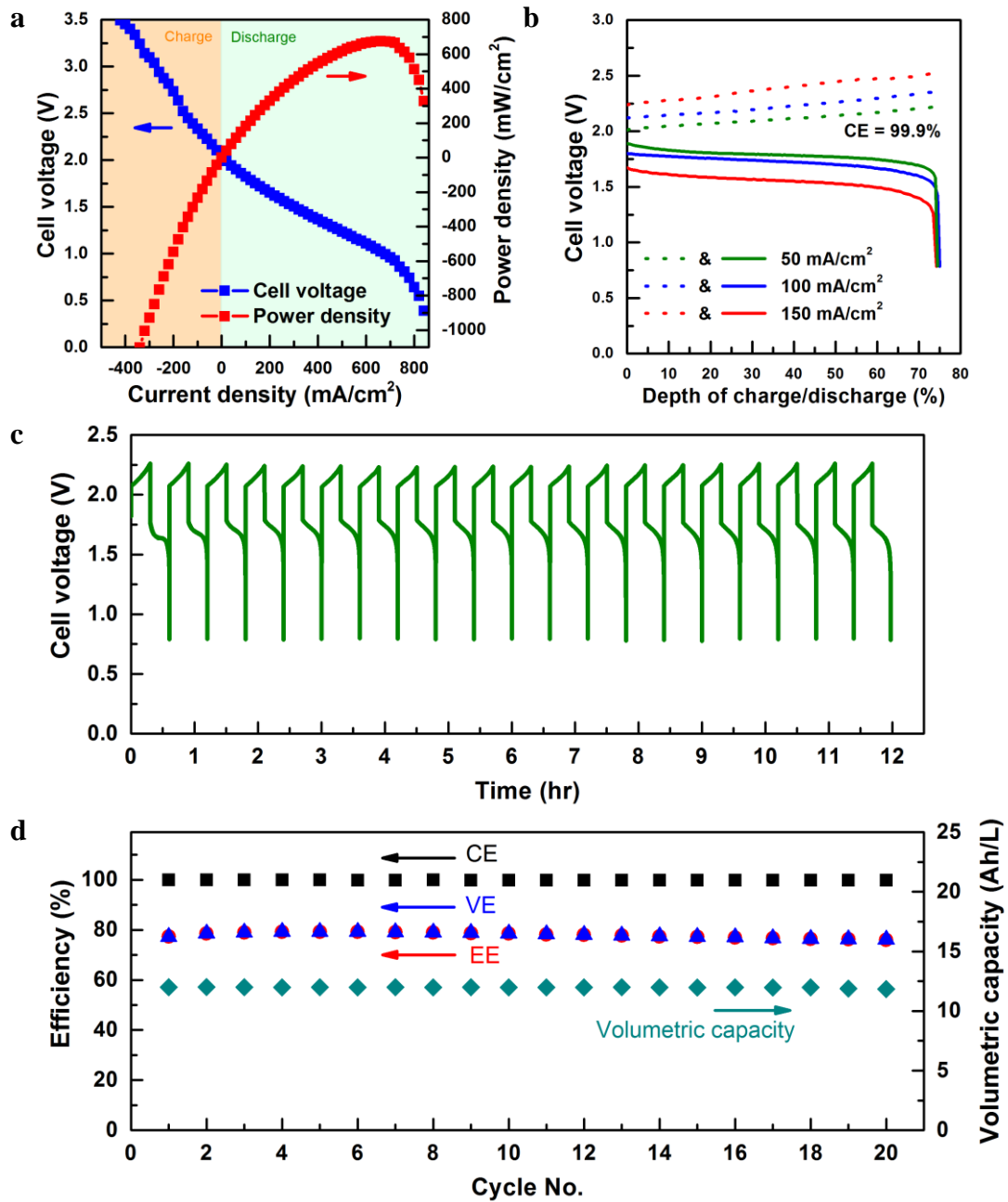


Figure 2.17 Cell performance and cycle test. (a) Discharge polarization curve of Zn-Fe RFB at 70% SOC. (b) Charge-discharge test with a 75% SOC swing at 50, 100, and 150 mA/cm² current density. (c) 20-cycle test voltage curve at 80 mA/cm² with a 75% SOC swing. (d) Coulombic efficiency (CE), voltage efficiency (VE) and capacity of each cycle.

Low element cost and high performance make the Zn-Fe RFB very attractive in terms of total capital cost. To quantify the capital cost of the double-membrane RFB system, we adapted the cost model for all-V and Fe-V RFBs developed by the Pacific Northwest National Lab (PNNL)^[149]. While the PNNL model has already taken into account all components in RFB system, adopted reliable pricing information and minimized total capital cost, we expanded the model to double-membrane configuration and other redox chemistries. The cell performance calculated by the model is validated against experimental data, as shown in Figure 2.18. Although it is not possible to verify the calculated result of large-scale systems, these preliminary results show that the model can precisely capture the Zn-Fe RFB performance at the small cell level.

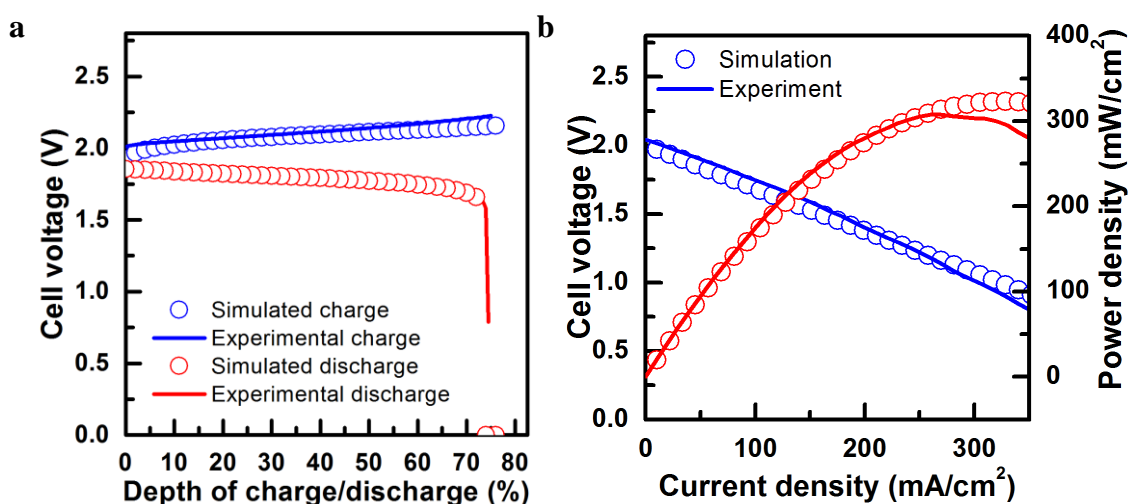


Figure 2.18 Validation of electrochemical model for Zn-Fe RFB. (a) Charge and discharge curves at current density of 50 mA/cm². (b) Polarization and power curves at a SOC of 50%. Note: the polarization curve was obtained by using Nafion 212 and FAA membranes which have larger resistances compared with Nafion 211 and Tokuyama A901.

Figure 2.19 shows the total capital cost of a 1 MW/8 MWh system with respect of operation current density for Zn-Fe RFBs and a few most notable RFBs, including all-V^[149], quinone-bromide^[153], hydrogen-bromide (membrane-less)^[117] and chromium-iron^[142]. It should be noted that Zn-Fe RFB shows the lowest overall capital cost in the mapped range among other RFBs. Such a low cost is achieved by the combination of high effective voltage and low redox material cost.

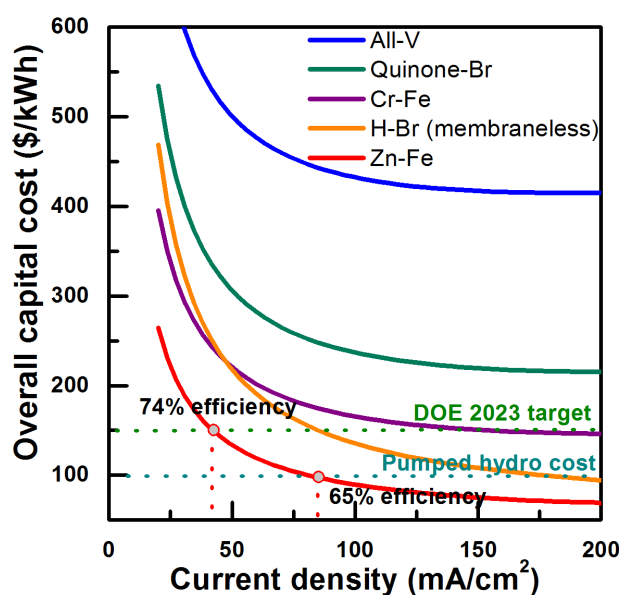
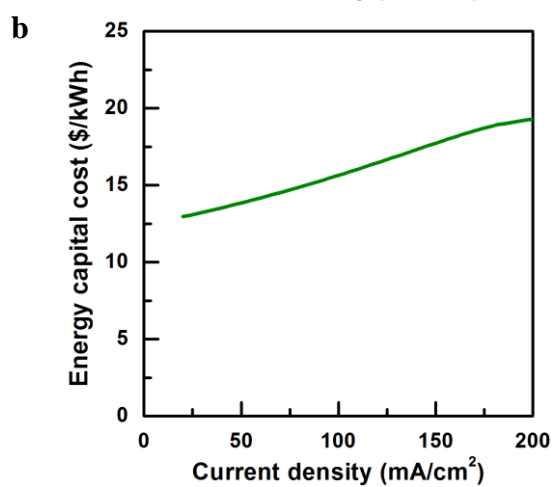
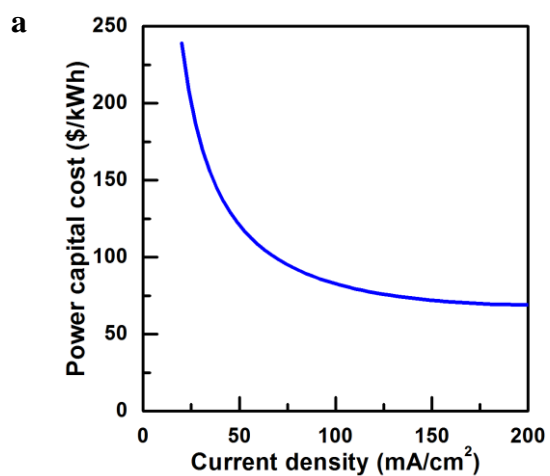


Figure 2.19 Zn-Fe RFB cost analysis and comparison with other notable RFBs.

Cost contributions and round-trip efficiency as a function of current density are also mapped over the range of current densities (Figure 2.20). It is apparent that power capital cost (mostly from stack cost) is decreasing along with current density while energy capital cost (mostly from redox material cost) increases along with current

density. The round-trip efficiency decreases along with current density because of larger voltage loss at high current density.



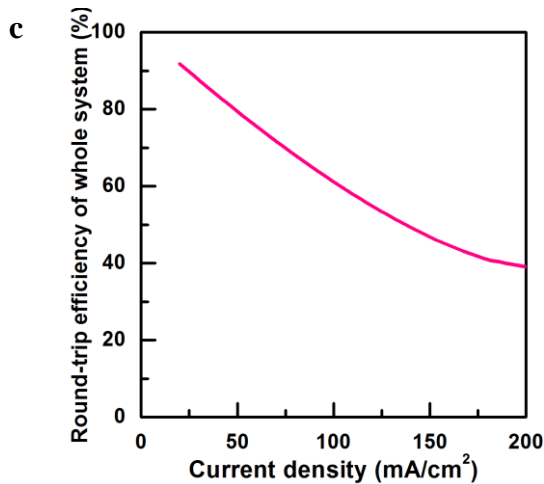


Figure 2.20 Capital cost and round-trip efficiency of the whole system. (a) Power capital cost (mostly from stack cost). (b) Energy capital cost (mostly from electrolyte cost). (c) Round-trip efficiency of the whole system.

At a current density of 40 mA/cm², a total capital cost of \$150/kWh is projected (with 73% of overall energy efficiency at the system level), which meets the 2023 DOE’s cost target (\$150/kWh). Increasing current density will result in even lower overall capital cost but lowered system efficiency, for example, a current density of 80 mA/cm² (65% system efficiency) will lower the total capital cost to \$100/kWh. It should be noted that the designed discharge duration is also an important factor that determines the total capital cost of RFB systems. The system capital cost decreases with increasing discharge duration, and it is below \$150/kWh when the discharge duration is greater than 5 hours (Figure 2.21).

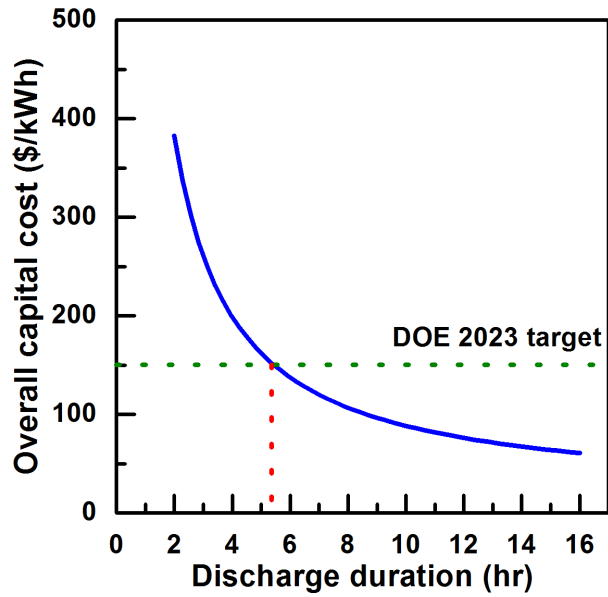


Figure 2.21 System capital cost of a 1 MW Zn-Fe RFB system as a function of discharge duration at a current density of 80 mA/cm².

In this work, we focus on engineering the middle electrolyte, leaving out the optimization of membranes and electrodes common to most RFB efforts. The system efficiency is expected to be improved by further reducing the cell resistance via adopting highly-conductive and selective membranes and engineering electrodes.

2.5.3 Summary of Zn-Fe RFB

Our results demonstrate that the Zn-Fe RFB can deliver high power density with inexpensive materials, making it the one of the most cost-effective RFB systems. The Zn-Fe RFB is able to meet the \$100/kWh of capital cost (with 65% system efficiency), although significant amount of work is still needed such as long-term durability testing and scale-up to large cells and stacks before industrial implementation.

2.6 Remaining Challenge — Crossover of Acid and Base

The new double-membrane cell configuration brings unprecedented freedom in choice and combination of redox pairs as well as supporting electrolytes. In this chapter, three of the most promising RFBs have been demonstrated. However, challenges associated with the double-membrane configuration will need to be addressed and mitigated before further pilot test and implementation in industrial.

In these three RFBs demonstrated, acid and base are used to support the positive and negative electrolytes respectively. The combination of acid and base could extend the water splitting window and redox chemistries applicable to RFB, but the crossover of acid and base and their further neutralization would bring challenges in long term stability and management.

In order to quantify the cyclability of the double-membrane RFB, the permeation coefficients of acid and base through an AEM or CEM were measured. The estimation method of RFB cyclability based on permeation coefficients and membrane resistance will be discussed in the following section.

2.6.1 Experiment and Methods

Cell setup. The permeation test was performed in a single-membrane cell assembled with either an AEM for H^+ crossover test, or a CEM for OH^- crossover test, as shown. 250 ml of 1 M HCl solution was used in the H^+ enriched side for acid crossover test, while 250 ml of 1 M NaOH was used in the OH^- side for base crossover test. 250 mL of 1 M NaCl solution was used in the H^+/OH^- deficient side to balance the osmotic pressure.

Detection of crossed-over acid and base. For detection of crossed-over acid/base concentration, 1 ml NaCl electrolyte was sampled at regular time intervals

and then diluted to 10 ml with deionized water. The pH of the diluted solution was then measured by a pH meter (Fisher Scientific, AB100).

Permeation coefficient. The general permeation of an ion crossing over through a membrane is shown in Eq. 2.1.

$$\frac{dn_B(t)}{dt} = P \frac{A}{L} (C_A - C_B(t)) \quad (\text{Equation 2.1})$$

where P is the permeation coefficient of the measured ion ($\text{cm}^2 \text{s}^{-1}$), A is the effective area of the ion-exchange membrane (cm^2), L is the thickness of the ion-exchange membrane (cm), C_A is the concentration of the measured ion in the enriched side (mol L^{-1}), C_B is the concentration of the measured ion in the deficient side (mol L^{-1}) and t is the permeation time (min).

The following assumptions can be made:

- The volume of solution in the deficient side (V_B) is constant.
- The value of C_A is constant (this is reasonable when employing a large volume of solution, e.g., 250 mL) and high concentration.
- The permeation coefficient is independent of the concentration.

Based on these assumptions, Eq. 2.1 can be integrated by the following steps:

$$\frac{dC_B(t)}{C_A - C_B(t)} = \frac{PA}{V_B L} dt \quad (\text{Equation 2.2})$$

$$-\int_0^{C_B} \frac{d(C_A - C_B(t))}{C_A - C_B(t)} = \frac{PA}{V_B L} \int_0^t dt \quad (\text{Equation 2.3})$$

$$\ln\left(\frac{C_A}{C_A - C_B(t)}\right) = \frac{PA}{V_B L} t \quad (\text{Equation 2.4})$$

Since A , V_B and L are known, the slope of a linearized fitting of $\ln(C_A/(C_A-C_B))$ against $At/(V_B L)$ can be used to obtain the permeation coefficient, P .

Method developed to estimate the lifetime for Zn-Fe RFB system. The method is based on a 1 MW/8 MWh RFB system. Due to the neutralization reaction between H^+ and OH^- , system failure is caused by the species that becomes depleted first. Since base is in excess in the Zn-Fe RFB, the limiting species is H^+ , i.e., battery fails whenever H^+ is completely consumed. Therefore, in this report, we define system failure as when the amount of crossed-over acid/base equals to 100% of initial acid amount. We assumed that the driving force is constant and thus the same as the initial driving force, and the coulombic efficiency of each cycle to be 100%. We set the RFB as having 75% voltage efficiency and all voltage losses from internal resistance.

The operational current density and internal resistance can be correlated through Eq. 2.5.

$$\eta = \frac{OCV - iR}{OCV + iR} = 75\% \quad (\text{Equation 2.5})$$

where η is voltage efficiency, OCV is the open circuit voltage of the Zn-Fe RFB, i is current density (A/cm^2) and R is total area-specific resistance ($\Omega \cdot cm^2$).

The amount of crossed-over species should be less than 100% of the initial amount of acid in positive electrolyte.

$$\frac{Power}{(OCV - iR) \cdot i} \times UCR \times t_{lifetime} = 100\% \cdot \frac{m \cdot Energy}{(OCV - iR) \cdot n \cdot F} \quad (\text{Equation 2.6})$$

where $Power$ is discharge power (MW), OCV is the open circuit voltage of Zn-Fe RFB (V), $t_{lifetime}$ is the battery lifetime (h), i is current density (A/cm^2) and R is total area-specific resistance ($\Omega \cdot cm^2$), UCR is unit crossover rate of membrane ($mol \cdot cm^{-2} \cdot h^{-1}$), $Energy$ is discharge energy (MWh), m is the concentration ratio of

acid over iron, n is the stoichiometric number of electrons in iron redox reaction, F is Faraday constant (C/mol).

The unit crossover rate is related to the permeation coefficient and concentration difference, as given by Fick's first law:

$$UCR(\text{flux}) = \frac{P}{d} \cdot \Delta C \quad (\text{Equation 2.7})$$

where ΔC is the concentration difference of H^+ / OH^- , d is membrane thickness.

The definition of conductivity gives:

$$R = \frac{d}{\sigma} \quad (\text{Equation 2.8})$$

where σ is the conductivity of balancing ion ($\Omega^{-1} \cdot \text{cm}^{-1}$).

Solving Eq. 2.5 – 2.8 gives the following result

$$t_{\text{lifetime}} = k \cdot \frac{\sigma}{P} \quad (\text{Equation 2.9})$$

where

$$k = \frac{m \cdot OCV}{\Delta C \cdot n \cdot F} \cdot \left(\frac{\text{Energy}}{\text{Power}} \right) \cdot \left(\frac{1 - \eta}{1 + \eta} \right)$$

$$\eta = 75\%$$

This equation is used to estimate the t_{lifetime} of membrane towards ion crossover of interest. The parameters used to calculate t_{lifetime} are listed in Table 2.1.

Table 2.1 Parameters used to calculate t_{lifetime} for Zn-Fe RFB

<i>Power</i> (MW)	1
<i>Energy</i> (MWh)	8
<i>OCV</i> (V)	2

ΔC_{NaOH} (mol/L)	5
ΔC_{HCl} (mol/L)	1
m	0.5
n	1

2.6.2 Results and Discussion

2.6.2.1 Permeation Coefficient of H^+ Through AEMs

The results of H^+ crossover through different AEMs are shown in Figure 2.22a. By a linear fitting of $\ln[C_A/(C_A - C_B)]$ vs. time, the permeation coefficient of H^+ was calculated. The result is listed in Table 2.2 and the battery lifetime of each membrane is positioned in Figure 2.22b.

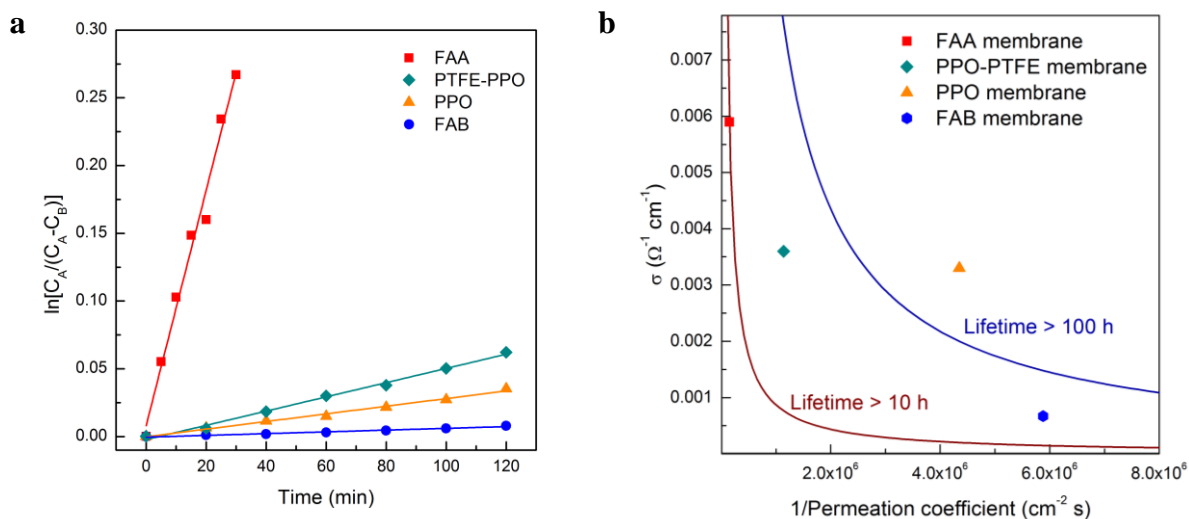


Figure 2.22 (a) Crossover measurement of H^+ across the FAA, PTFE-PPO, PPO and FAB membranes. The slope obtained from linear fitting of $\ln[C_A/(C_A - C_B)]$ vs. time is used to calculate the permeation coefficient. (b) Position of different AEMs in terms of conductivity of the balancing ion and $1/\text{permeation coefficient}$ of the proton. The contour lines of 10, 100 and 1000 h lifetimes are shown as red, blue, and green lines, respectively. Positions closer to the upper righthand corner represent longer lifetimes.

It can be seen that FAA membrane has a larger permeation coefficient compared with other three membranes. The battery lifetime, however, also depends on the conductivity of the membrane to the balancing ion, as shown in Eq. 7. σ/P and cyclability are calculated for each membrane and listed in Table 2.2. The results show that PPO membrane demonstrates the longest t_{lifetime} , reaching 170 h.

Table 2.2 Thickness, permeation coefficient, conductivity, σ/P and t_{lifetime} of different AEMs.

AEMs	Thickness (μm)	Permeation coefficient (cm^2/s)	σ of balancing ion ($\Omega^{-1}\cdot\text{cm}^{-1}$)	σ/P ($\Omega\cdot\text{cm}^{-1}\cdot\text{s}^{-1}$)	t_{lifetime} (h)
FAA	45	6.8×10^{-6}	5.9×10^{-3}	8.7×10^2	10
FAB	130	1.7×10^{-7}	6.7×10^{-4}	3.9×10^3	47
PPO	35	2.3×10^{-7}	3.3×10^{-3}	1.4×10^4	170
PTFE-PPO	55	8.8×10^{-7}	3.6×10^{-3}	4.1×10^3	48

2.6.2.2 Permeation Coefficient of OH^- Through CEMs

The result of OH^- crossover through different CEMs is shown in Figure 2.23. The permeation coefficient of OH^- was calculated based on Figure 2.23a. The result of membrane conductivity, σ/P and calculated lifetime is listed in Table 2.3 and the battery lifetime of each membrane is also positioned in Figure 2.23b.

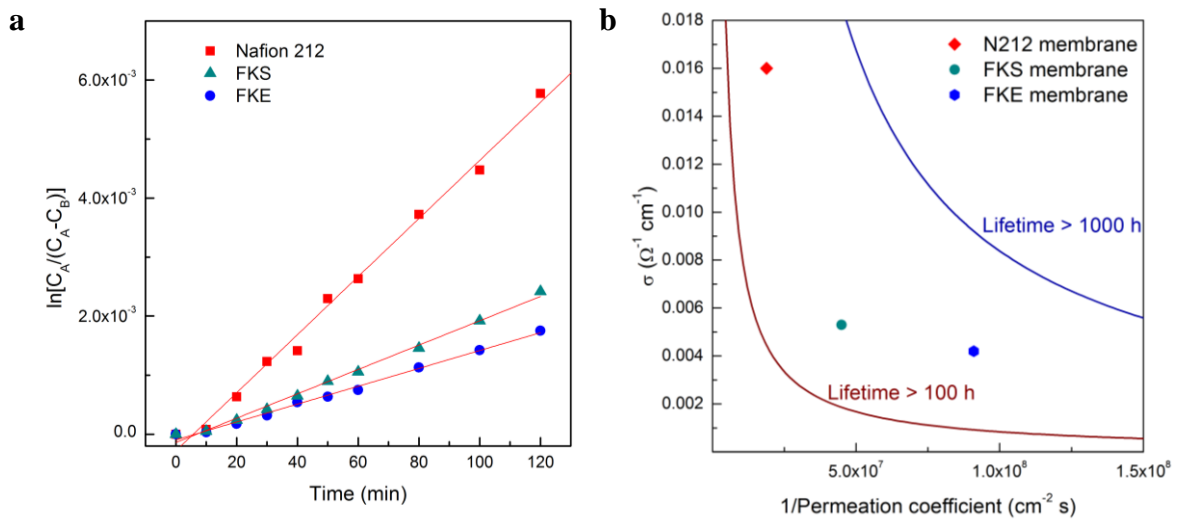


Figure 2.23 (a) Crossover measurement of OH⁻ across the Nafion 212, FKS, and FKE membranes. The slope obtained from linear fitting of $\ln[C_A/(C_A - C_B)]$ vs. time is used to calculate permeation coefficient. (b) Position of different CEMs in terms of their conductivity of balancing ion and 1/permeation coefficient of hydroxide ion. The contour lines of 100, 1000 and 5000 h lifetimes are shown in red, blue and green lines, respectively. Positions closer to the upper right corner represent longer lifetimes.

It is shown that three membranes have similar OH⁻ permeation coefficients. The OH⁻ permeation coefficients of CEMs is one order of magnitude smaller than H⁺ permeation coefficients of AEMs, due to the slower mobility of OH⁻ and better selectivities of CEMs. The conductivity of the balancing ion for CEMs is also larger than that for AEMs. However, since the driving force for base crossover is larger ($\Delta C_{\text{NaOH}}=5 \text{ M}$ vs. $\Delta C_{\text{HCl}}=0.5 \text{ M}$), the t_{lifetime} is only slightly longer than that for AEMs.

Table 2.3 Thickness, permeation coefficient, conductivity, σ/P and t_{lifetime} of different CEMs.

CEMs	Thickness (μm)	Permeation coefficient (cm^2/s)	σ of balancing ion ($\Omega^{-1} \cdot \text{cm}^{-1}$)	σ/P ($\Omega \cdot \text{cm}^{-1} \cdot \text{s}^{-1}$)	t_{lifetime} (h)
Nafion 212	50	5.3×10^{-8}	1.6×10^{-2}	3.0×10^5	358
FKE	50	1.1×10^{-8}	4.2×10^{-3}	3.8×10^5	452
FKS	50	2.2×10^{-8}	5.3×10^{-3}	2.4×10^5	285

From those crossover tests, it is evident that acid and base crossover is a prominent issue that prohibits long-term operation without intervention for the Zn-Fe

RFB. AEMs and CEMs with better acid and base blocking property are required for the Zn-Fe RFB under its present double-membrane configuration.

2.7 Concluding Remarks

This chapter explores a new RFB setup which uses a double-membrane triple-electrolyte configuration. This new configuration solves the long-lasting limitation of single-membrane cell and enables a lot of new redox chemistries in RFB. Three examples have been demonstrated: (i) the ultra-high voltage zinc-cerium RFB with 3.08 V of standard cell voltage; and (ii) the ultra-low material cost sulfur-iron RFB with 1.22 V of standard cell voltage, based on highly-available elements; and (iii) the balanced high-voltage and low-cost zinc-iron RFB with 1.99 V of standard cell voltage.

All these three RFBs showed expected open-circuit voltage and charge-discharge performance, which successfully demonstrated the feasibility of double-membrane configuration. The Zn-Ce RFB has the highest standard voltage among all aqueous RFBs, but is limited by the stability issue of the AEM. The S-Fe RFB takes advantage of ultra-low cost elements to deliver very cheap electrolyte cost, but its performance suffers from low standard voltage as well as large internal resistance. The Zn-Fe RFB achieves the best balance between high voltage (1.99 V) and low cost ($\$0.73/\text{Ah}$). The Zn-Fe RFB shows the 3rd highest power density, after the all-V and H-Br RFB, and the lowest initial capital cost among several notable RFBs including the All-V, quinone-Br, Cr-Fe, H-Br. The most urgent challenge identified so far is the crossover of acid and base through two membranes. Since the positive and negative electrolytes have to remain in acidic and basic environments, respectively, long-term

cycle testing can only be done with frequent addition of acid and base in the positive and negative electrolytes. This could obviously increase the maintenance cost and cause water balance problems in practice. Should the issue of acid/base crossover be mitigated through better membranes or techniques, the Zn-Fe RFB is recommended for pilot testing and further development.

Chapter 3

AN ALL-SOLUBLE ALL-IRON RFB BASED ON COORDINATION CHEMISTRY OF IRON

3.1 Introduction

Redox-flow batteries (RFBs) have been considered one of the most flexible systems for stationary energy storage, thanks to their decoupled energy and power^[6, 14]. A typical RFB consists of two soluble redox pairs separated by an ion-exchange membrane (IEM). Designed for large-scale energy storage, RFBs are required to have low system cost and long service life. Unfortunately, the imperfect selectivity of existing IEMs inevitably leads to undesired crossover of redox species between the negative and positive electrolytes. Electrolyte contamination brought on by the crossover of redox species can cause permanent losses in both battery capacity and coulombic efficiency, drastically threatening the reliability and durability of RFBs. The crossover problem can be mitigated to a certain extent by using one mixed electrolyte as both the negative and positive electrolytes. However, the use of mixed electrolytes often results in lowered cell voltage and increased material costs^[52]. An alternative approach is to use the same redox-active element to create the two redox pairs. The all-vanadium (all-V) RFBs are an excellent example, and the all-V RFBs use two vanadium-based redox pairs that fundamentally eliminate the problematic cross-contamination from two different redox-active elements and provide unlimited cyclability in theory^[67]. Largely because of their intrinsic tolerance to cross-contamination, significant efforts have been devoted to improve all-V RFBs for the

past three decades, making them the most successful RFBs to-date. However, one challenging issue for all-V RFBs is the high material cost that hinders their widespread deployment. Other RFBs based on the same redox-active elements with different valence states have been proposed, including all-chromium (all-Cr), all-iron (all-Fe), all-lead (all-Pb), and all-copper (all-Cu) RFBs^[155-158]. In particular, all-Fe RFBs have advantages such as low toxicity and very low cost^[38]. The existing all-Fe RFB was pioneered by L. W. Hruska and R. Savinell as early as 1981, and this all-Fe RFB is constructed by the Fe²⁺/Fe redox pair and Fe³⁺/Fe²⁺ redox pair in negative electrolyte and positive electrolyte, respectively^[38]. It was a great invention; however in their design, the solid iron metal is involved in the negative redox reaction. As such, the energy and power of this all-Fe RFB are no longer completely decoupled from one another. In addition, the deposition and dissolution of iron metal on the negative electrode brings concerns of dendrite formation. Moreover, the hydrogen evolution reaction (HER) as a side reaction poses a serious challenge, since the standard redox potential of Fe²⁺/Fe is 450 mV more negative than HER at pH = 0^[38]. An all-soluble all-Fe RFB may have the potential to address the issues associated with the participation of iron metal yet maintain the advantages from the same redox-active elements.

It has been known that organic ligands can coordinate with many metal ions to form soluble redox pairs, which offers many possibilities for all-soluble, all-(redox-active-element) RFBs. Many soluble redox pairs based on iron complexes have been explored and are summarized in Figure 3.1 and Table 3.1^[25, 159-162], and herein we present the first example of an all-soluble all-Fe RFB by combining the iron-triethanolamine redox pair (i.e., [Fe(TEOA)OH]⁻/[Fe(TEOA)(OH)]²⁻, denoted as Fe-

TEOA) and the iron-cyanide redox pair (i.e., $\text{Fe}(\text{CN})_6^{3-}/\text{Fe}(\text{CN})_6^{4-}$, denoted as Fe-CN) in a simple single-IEM cell configuration.

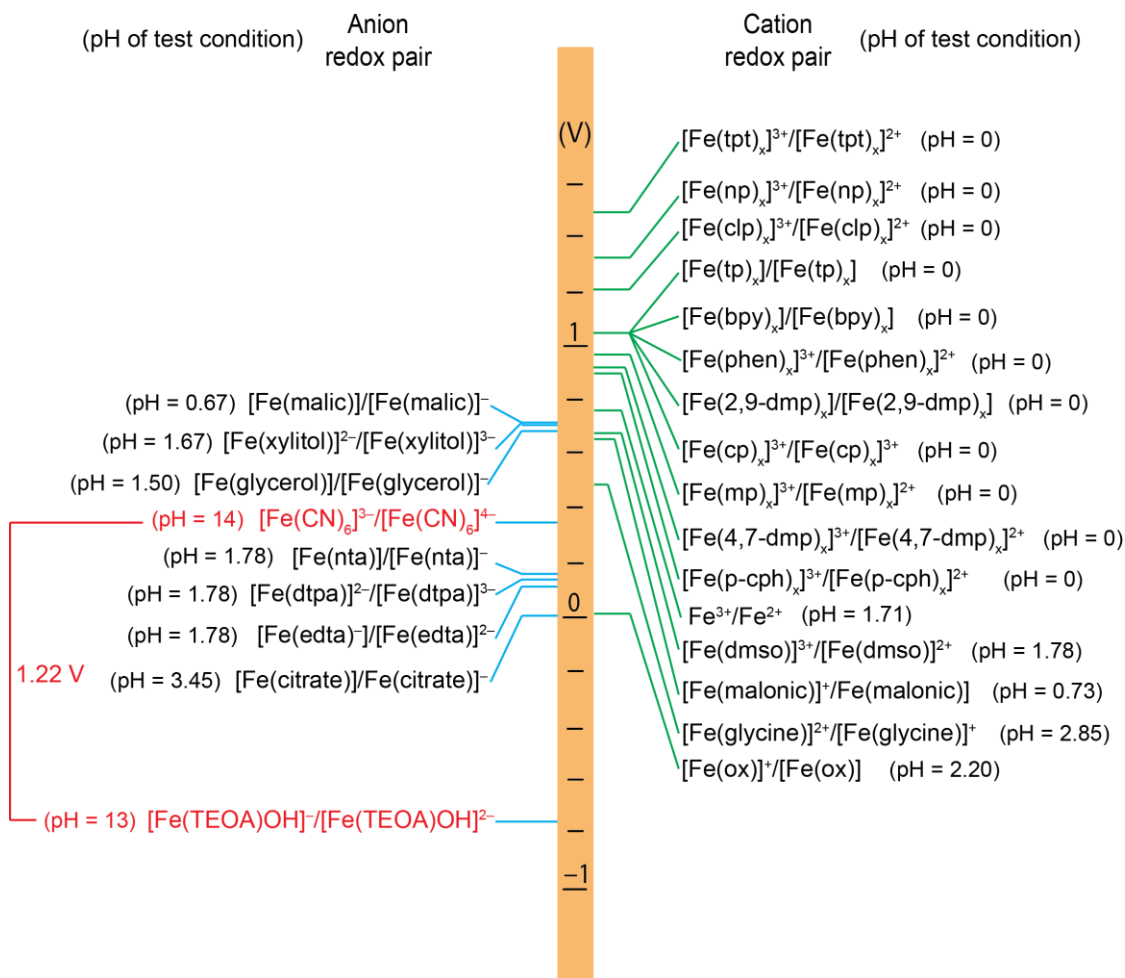


Figure 3.1 Redox pairs of iron complexes that have been tested for RFB applications. Each redox pair is represented by its formal potential vs. standard hydrogen electrode (SHE) potential at the corresponding pH of its test conditions. The full names of any abbreviations are listed in Table 3.1. The highlighted $[\text{Fe}(\text{TEOA})\text{OH}]^-/\text{Fe}(\text{TEOA})(\text{OH})_2^{2-}$ and $\text{Fe}(\text{CN})_6^{3-}/\text{Fe}(\text{CN})_6^{4-}$ redox pairs constitute the all-Fe RFB in this work.

Table 3.1 Electrode potentials, kinetic constants and pHs of test conditions of iron(III)/iron(II)-ligand redox pairs

Ligand	Abbreviation	ϕ' vs. SHE ^[a] (V)	k^0 (cm s ⁻¹) ^[b]	pH of test condition
Tripyridinetriazine	tpt	1.484 (from SCE)		0
5-Nitro-o-phenantroline	np	1.334 (from SCE)		0
5-Chloro-o-phenanthroline	clp	1.214 (from SCE)		0
Bipyridine	bpy	1.064 (from SCE)	5.60×10^{-2}	0
o-phenanthroline	phen	1.064 (from SCE)	5.80×10^{-2}	0
2,9-Dimethyl-o-phenantroline	2,9-dmp	1.064 (from SCE)		0
Terpyridine	tp	1.064 (from SCE)	6.00×10^{-2}	0
4-Cyanopyridine	cp	1.064 (from SCE)		0
4-methy-o-phenantroline	mp	0.974 (from SCE)	4.90×10^{-2}	0
4,7-Dimethyl-o-phenantroline	4,7-dmp	0.934 (from SCE)	2.50×10^{-2}	0
2-Pyridinecarboxaldehyde	p-cph	0.914 (from SCE)		0
malic acid		0.696 (from Ag/AgCl)	4.15×10^{-5}	0.67
xylitol		0.692 (from Ag/AgCl)	1.35×10^{-4}	1.67
glycerol		0.685 (from Ag/AgCl)	8.29×10^{-5}	1.5
Dimethylsulfoxide	dmsO	0.675 (from Ag/AgCl)	1.24×10^{-4}	1.78
malonic acid		0.652 (from Ag/AgCl)	9.33×10^{-5}	0.73
glycine		0.511 (from Ag/AgCl)	2.07×10^{-5}	2.85
Cyanide ^[c]	CN	0.483 (from SCE)	2.48×10^{-2}	14.5
Nitrilotriacetic acid	nta	0.174 (from SCE)	1.56×10^{-2}	2.8
Diethylenetriaminepentaacetic acid	dtpa	0.151 (from SCE)	1.24×10^{-2}	2.5
ethylenediaminetetraacetic acid	edta	0.130 (from SCE)	3.49×10^{-2}	2.8
oxalate	ox	0.054 (from SCE)		2.2
citrate		-0.045 (from Ag/AgCl)	9.33×10^{-5}	3.45
Triethanolamine ^[d]	TEOA	-0.859 (from Ag/AgCl)	1.08×10^{-2}	13

[a] ϕ' : formal redox potential. Potential was converted to standard hydrogen potential (SHE) by relationships: SCE=0.244 V vs. SHE, Ag/AgCl=0.194 V vs. SHE.
[b] k^0 : standard rate constant of redox reaction. k^0 was either taken directly from literature or converted from exchange current density reported in literature.
[c] This work.
[d] This work.

The Fe-TEOA redox pair is composed of two anions and has a redox potential of -0.86 V vs. SHE (formal potential, measured in $\text{pH} = 13$). The Fe-CN redox pair is also composed of two anions and has a redox potential of $+0.36$ V vs. SHE (standard potential). The all-soluble all-Fe RFB based on Fe-TEOA and Fe-CN as redox pairs is expected to have a standard cell voltage of 1.22 V, slightly higher than that of the existing metallic-Fe-based all-Fe RFB mentioned above (1.12 V).

The corresponding redox reactions and electrode potentials are shown below.



In addition to the slightly increased cell voltage, the standard rate constants on glassy carbon of Fe-TEOA ($6.3 \times 10^{-2} \text{ cm s}^{-1}$)^[155] and Fe-CN ($1.0 \times 10^{-1} \text{ cm s}^{-1}$)^[163] are also more facile than pristine $\text{Fe}^{3+}/\text{Fe}^{2+}$ ($1.2 \times 10^{-3} \text{ cm s}^{-1}$) and Fe^{2+}/Fe ($3.3 \times 10^{-9} \text{ cm s}^{-1}$) redox pairs ^[163, 164], drastically lowering electrode overpotential.

All-soluble redox pairs, high cell voltage, and facile kinetics make this Fe-TEOA- and Fe-CN-based all-Fe RFB a possible candidate for renewable energy storage warranting consideration. Development is not limited to this example; as shown in Figure 3.1, there are many other possibilities to construct an all-soluble all-Fe RFB (note that a multiple-IEM cell configuration is required when using redox pairs with opposite charges^[135]).

3.2 Experiment and Method

Cyclic voltammetry. A three-electrode cell configuration was used for the cyclic voltammetry (CV) test. Glassy carbon (dia.=5 mm, Pine Instrument), platinum wire and a Ag/AgCl electrode were used as the working, counter, and reference

electrodes, respectively. The cell was tested by a multichannel potentiostat (VMP2, Princeton Applied Research). The working electrode was polished to a mirror finish prior to the use in each set of CV test.

RFB cell assembly. The all-soluble all-Fe RFB (Figure 3.2) consists of two blocks of electrolyte frames, two current conductors and collectors, and two Viton rubber gasket (0.4 mm thickness per piece). One piece of carbon paper (2.2 cm×2.3 cm, 0.37 mm thickness Toray-H-120) was used for the negative electrode. Two pieces of carbon paper (2.2 cm×2.3 cm, one 0.19 mm thickness, Toray-H-60, the other 0.37 mm thickness, Toray-H-120) were used for the positive electrode. The purpose of using different carbon papers on each side is to keep the total thickness of carbon paper only slightly larger than the total gasket thickness to ensure good sealing and firm contact between carbon paper and current collector. A Nafion 212 membrane was used as the separator. The membrane was soaked in 1 M NaCl solution for 48 hours and thoroughly washed with DI water to remove residual NaCl solution from the surface before use. Eight bolts were torqued to 16 lb ft to tighten the cell and provide firm compression between the electrode and the current collector. The electrolyte was pumped by a peristaltic pump (Cole Parmer, Masterflex[®] L/S 600 rpm) through PTFE-lined rubber tubes (Cole Parmer, ChemDurance[®] #16). A flow rate of 100 mL min⁻¹ was used in all tests. The all-soluble all-Fe RFB was tested by a commercial battery test station (Arbin, BT2000). All tests were conducted at room temperature.

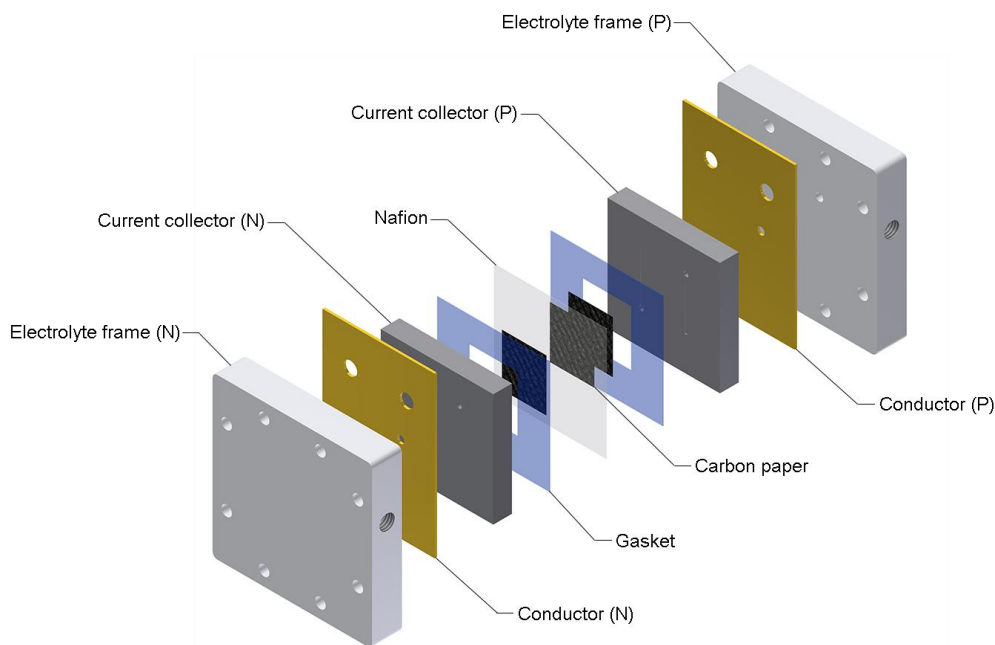


Figure 3.2 Cell configuration for the all-Fe RFB. The electrolyte flows into the system through the side inlet of electrolyte frame. The positive and negative electrolytes flow through the small holes on electrolyte frame, conductor, and current collector into the chamber encompassed by gasket and membrane.

TEOA, $[\text{Fe}(\text{TEOA})\text{OH}]^-$, $[\text{Fe}(\text{TEOA})(\text{OH})]^{2-}$, $\text{Fe}(\text{CN})_6^{3-}$ and $\text{Fe}(\text{CN})_6^{4-}$ crossover test. The RFB cell was set up with 20 cm² membrane exposure, an enriched side filled with solution of target species, and the deficient side filled with a blank salt solution. For TEOA, $[\text{Fe}(\text{TEOA})\text{OH}]^-$, $[\text{Fe}(\text{TEOA})(\text{OH})]^{2-}$ crossover tests, the enriched solution contained 0.2 M FeCl_3 or FeCl_2 , 1 M TEOA and 1.5 M NaOH (30 mL). 1 M NaCl solution (15 mL) was used on the deficient side to minimize the difference in osmotic pressure and volume change of electrolyte. Every 1 hour, 300 μL electrolyte from the deficient side was sampled with an addition of 400 μL deuterated water (D_2O) for ¹³C NMR testing (Bruker AV-400), and 600 μL was withdrawn and

diluted to 3 mL with 2315 μL 1 M hydrochloric acid and 85 μL 70% nitric acid for ICP-OES test (Optima 7300DV). The same cell setup was used for the $\text{Fe}(\text{CN})_6^{3-}$ or $\text{Fe}(\text{CN})_6^{4-}$ crossover tests. 30 mL 0.2 M $\text{Na}_4\text{Fe}(\text{CN})_6$ in 0.5 M NaOH or 0.2 M $\text{K}_3\text{Fe}(\text{CN})_6$ in 0.5 M KOH were used on the enriched side. 0.5 M NaCl or KCl were used on the deficient side. The deficient-side solution was sampled and measured by the same method as for the ^{13}C NMR test.

TEOA degradation study in presence of $\text{Fe}(\text{CN})_6^{3-}$. The chemical reaction between $\text{Fe}(\text{CN})_6^{4-}$ and TEOA was studied by analyzing the ^1H NMR spectra of deuterated water solutions containing 0.2 M TEOA, 0.5 M $\text{K}_3\text{Fe}(\text{CN})_6$ and 0.5 M KOH. The electrolyte was sampled at different times and measured by ^1H NMR spectroscopy using the same solvent and dilution ratio as in the TEOA crossover test. The ^1H NMR spectra for predicted degradation products were obtained by MestReNova 6.1.

Impedance test. Impedance for the all-soluble all-Fe full RFB cell was measured at 50% SOC. To study the impact of TEOA on the Nafion membrane, RFB cell was set up with three solution concentrations: a) 3 M NaOH for both sides; b) 3 M NaOH and 2 M TEOA for both sides; and c) 3 M NaOH, 2 M TEOA and 0.4 M FeCl_3 for both sides. The impedance was measured by a potentiostat (Solatron A1287) and impedance analyzer (Solatron A1260).

Cycle test. RFB cell was set up with solutions of 0.2 M FeCl_3 , 1 M TEOA, 1.5 M NaOH as the negative electrolyte; and 0.2 M $\text{Na}_4\text{Fe}(\text{CN})_6$, 3 M NaOH as the positive electrolyte. These concentrations were chosen to keep similar the osmotic pressure of the electrolytes and minimize water transport during long-term cycle test.

The current density was set at 40 mA cm^{-2} with cut-off voltages of 0.5 V (discharge) and 1.6 V (charge).

Polarization test. The RFB cell was set up with the same electrolytes as in cycle test. The battery was first charged to 70% SOC; then, alternating charge and discharge current was applied. Cell voltage was recorded at each current density.

3.3 Results and Discussion

3.3.1 Redox Electrochemistry

The standard potential of the $\text{Fe}(\text{CN})_6^{3-}/\text{Fe}(\text{CN})_6^{4-}$ redox pair is 0.36 V. However, the formal potential depends on the ionic strength of solution; it can reach around 0.44 V in a solution with an ionic strength equivalent to 0.5 M salt solution^[165]. As shown in cyclic voltammetry (CV) of the two redox pairs, the formal potential difference between the two redox pairs is 1.34 V (Figure 3.3).

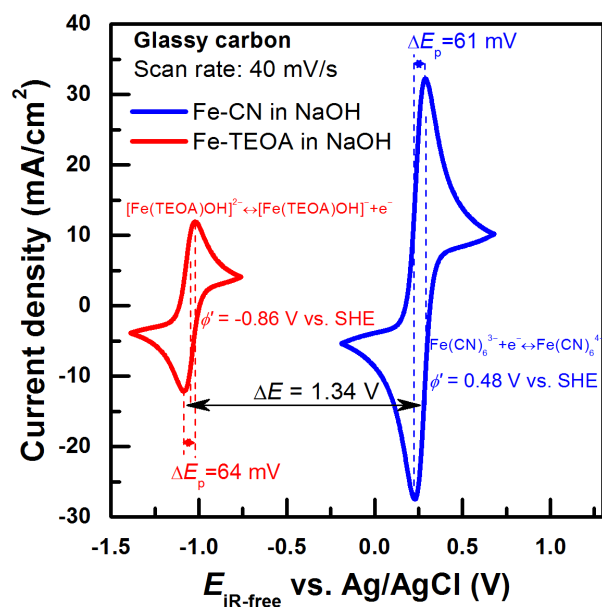


Figure 3.3 Cyclic voltammetry of $[\text{Fe}(\text{TEOA})\text{OH}]^{-}/[\text{Fe}(\text{TEOA})\text{OH}]^{2-}$ and $\text{Fe}(\text{CN})_6^{3-}/\text{Fe}(\text{CN})_6^{4-}$ in sodium hydroxide solution. The Fe-TEOA solution contains 0.2 M FeCl_2 , 0.2 M FeCl_3 , 2 M TEOA and 3 M NaOH. The Fe-CN solution contains 0.2 M $\text{Na}_4\text{Fe}(\text{CN})_6$, 0.2 M $\text{Na}_3\text{Fe}(\text{CN})_6$ and 3 M NaOH. The working electrode is glassy carbon and scan rate is 40 mV/s for both cases.

CVs at different scan rates were also taken to measure the standard rate constant of the $[\text{Fe}(\text{TEOA})\text{OH}]^{-}/[\text{Fe}(\text{TEOA})\text{OH}]^{2-}$ redox pair and the diffusion coefficient of each species, based on the method of Nicholson and the Randles-Sevcik equation, respectively (Figure 3.4). The results are listed in Table 3.2. Both diffusion coefficients and the standard rate constant measured in this work are comparable to the reported values in the literature ($1.6 \times 10^{-6} \text{ cm}^2 \text{ s}^{-1}$, and $6.3 \times 10^{-2} \text{ cm s}^{-1}$)^[155].

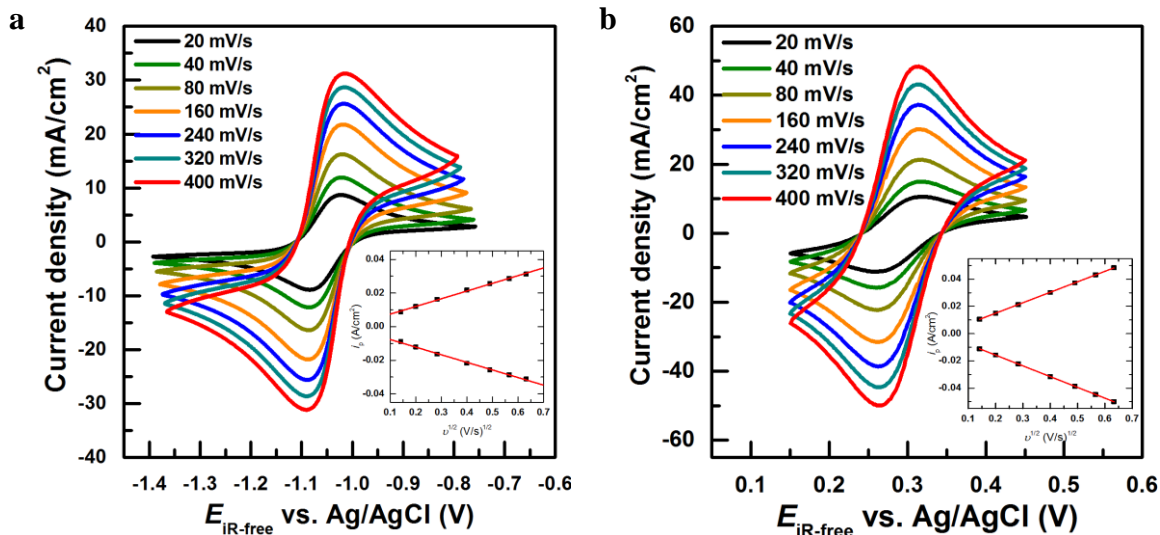


Figure 3.4 (a) Cyclic voltammetry of $[\text{Fe}(\text{TEOA})\text{OH}]^-/[\text{Fe}(\text{TEOA})\text{OH}]^{2-}$ at different scan rates on glassy carbon electrode. The electrolyte contains 0.2 M FeCl_2 , 0.2 M FeCl_3 , 2 M TEOA and 3 M NaOH. (b) Cyclic voltammetry of $\text{Fe}(\text{CN})_6^{4-}/\text{Fe}(\text{CN})_6^{3-}$ at different scan rates on glassy carbon electrode. The electrolyte contains 0.1 M $\text{Na}_4\text{Fe}(\text{CN})_6$, 0.1 M $\text{K}_3\text{Fe}(\text{CN})_6$, and 3 M NaOH.

Table 3.2 Diffusion coefficients of $[\text{Fe}(\text{TEOA})\text{OH}]^-$ (D_O), $[\text{Fe}(\text{TEOA})\text{OH}]^{2-}$ (D_R), and standard rate constant (k^0) of the $[\text{Fe}(\text{TEOA})\text{OH}]^-/[\text{Fe}(\text{TEOA})\text{OH}]^{2-}$ redox pair.

D_O ($\text{cm}^2 \text{s}^{-1}$)	D_R ($\text{cm}^2 \text{s}^{-1}$)	k^0 (cm s^{-1})
7.1×10^{-7}	7.2×10^{-7}	1.1×10^{-2}

The facile kinetics of the $\text{Fe}(\text{CN})_6^{3-}/\text{Fe}(\text{CN})_6^{4-}$ redox pair has been well established. The diffusion coefficients and standard rate constant of the $\text{Fe}(\text{CN})_6^{3-}/\text{Fe}(\text{CN})_6^{4-}$ redox pair were also measured; the results are listed in Table 3.3.

Table 3.3 Diffusion coefficients of $\text{Fe}(\text{CN})_6^{3-}$ (D_{O}), $[\text{Fe}(\text{CN})_6]^{4-}$ (D_{R}), and standard rate constant (k^0) of the $\text{Fe}(\text{CN})_6^{3-}/\text{Fe}(\text{CN})_6^{4-}$ redox pair.

D_{O} ($\text{cm}^2 \text{s}^{-1}$)	D_{R} ($\text{cm}^2 \text{s}^{-1}$)	k^0 (cm s^{-1})
8.6×10^{-6}	8.2×10^{-6}	2.5×10^{-1}

The standard rate constants of $[\text{Fe}(\text{TEOA})\text{OH}]^- / [\text{Fe}(\text{TEOA})(\text{OH})]^{2-}$ and $\text{Fe}(\text{CN})_6^{3-}/\text{Fe}(\text{CN})_6^{4-}$ are much larger than those of the $\text{Fe}^{3+}/\text{Fe}^{2+}$ redox pair in acid ($1.2 \times 10^{-4} \text{ cm s}^{-1}$), suggesting there is little overpotential on both the positive and negative sides.

3.3.2 Cell Performance and Preliminary Durability

The all-soluble all-Fe RFB was assembled, and the charge-discharge test at 40 mA cm^{-2} current density is shown in Figure 3.5. Coulombic efficiency (CE), voltage efficiency (VE), and energy efficiency (EE) for this one cycle are 93%, 78% and 73%, respectively. Energy efficiency is higher than that of the traditional metallic iron-based all-Fe RFB (Fe^{2+}/Fe vs. $\text{Fe}^{3+}/\text{Fe}^{2+}$), which demonstrates an energy efficiency between 11–44% at slightly higher current density (60 mA cm^{-2})^[38]. Successful charge-discharge testing and good performance observed here clearly confirms the feasibility of all-soluble all-Fe RFB.

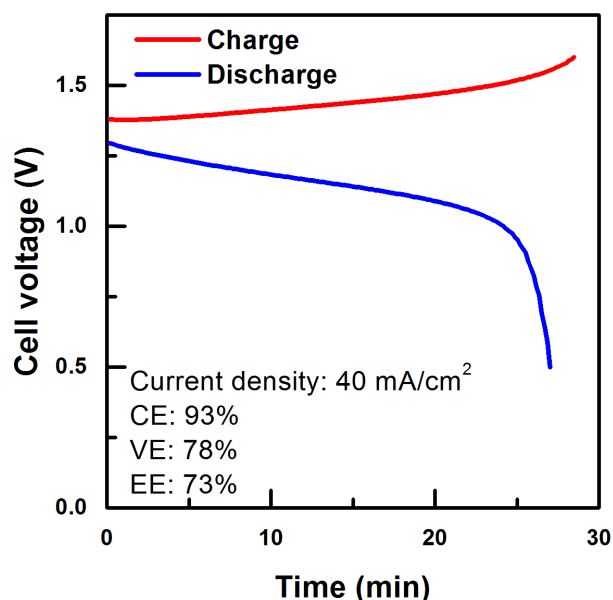


Figure 3.5 Cell voltage curve of a charge-discharge test of the all-Fe RFB at 40 mA/cm².

The polarization curve of the all-soluble all-Fe RFB is shown in Figure 3.6. Power density peaks at 160 mW cm⁻². The discharge power density is higher than in the traditional all-soluble all-Fe RFB, (~120 mW cm⁻²)^[38]. Due to the facile kinetics of both redox pairs, the electrode overpotential is very small. Voltage and current density follow a typical ohmic relationship, indicating that the majority of the voltage losses comes from the large internal resistance. A detailed analysis of internal resistance follows in Section 3.4.2.

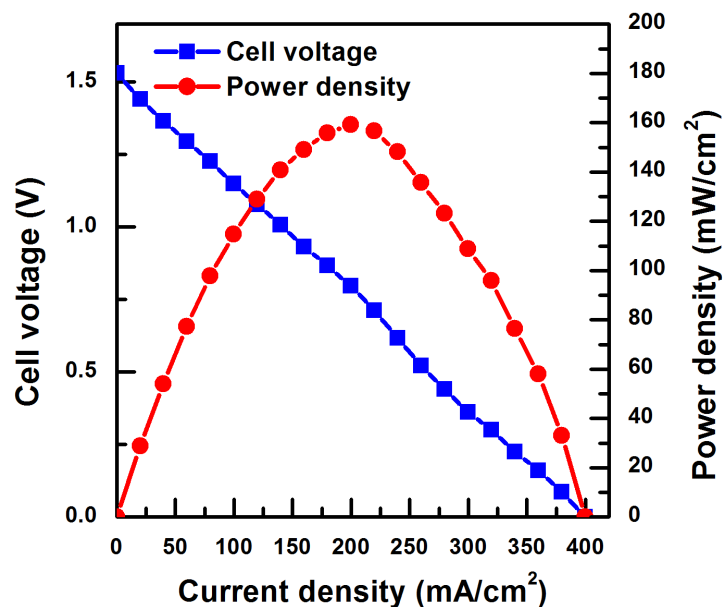


Figure 3.6 Polarization curve of the all-Fe RFB at 70% state of charge (SOC) with peak power density at 160 mW/cm². The polarization curve shows strong ohmic relationship between voltage and current density, indicating the system is limited by internal resistance.

Figure 3.7a shows 110 cycles of charge-discharge voltage curves at a current density of 40 mA cm⁻², and Figure 3.7b the corresponding CE, VE, EE and capacity. CE remains between 80% and 90%, and VE is stable at above 80%. The capacity initially decreases, then becomes stable and oscillates after 20 cycles. The initial decay is largely due to the crossover of free TEOA, which is discussed in more detail in Section 3.4.1. Such capacity decay is in agreement with observations in other Fe-TEOA related RFBs^[155, 158].

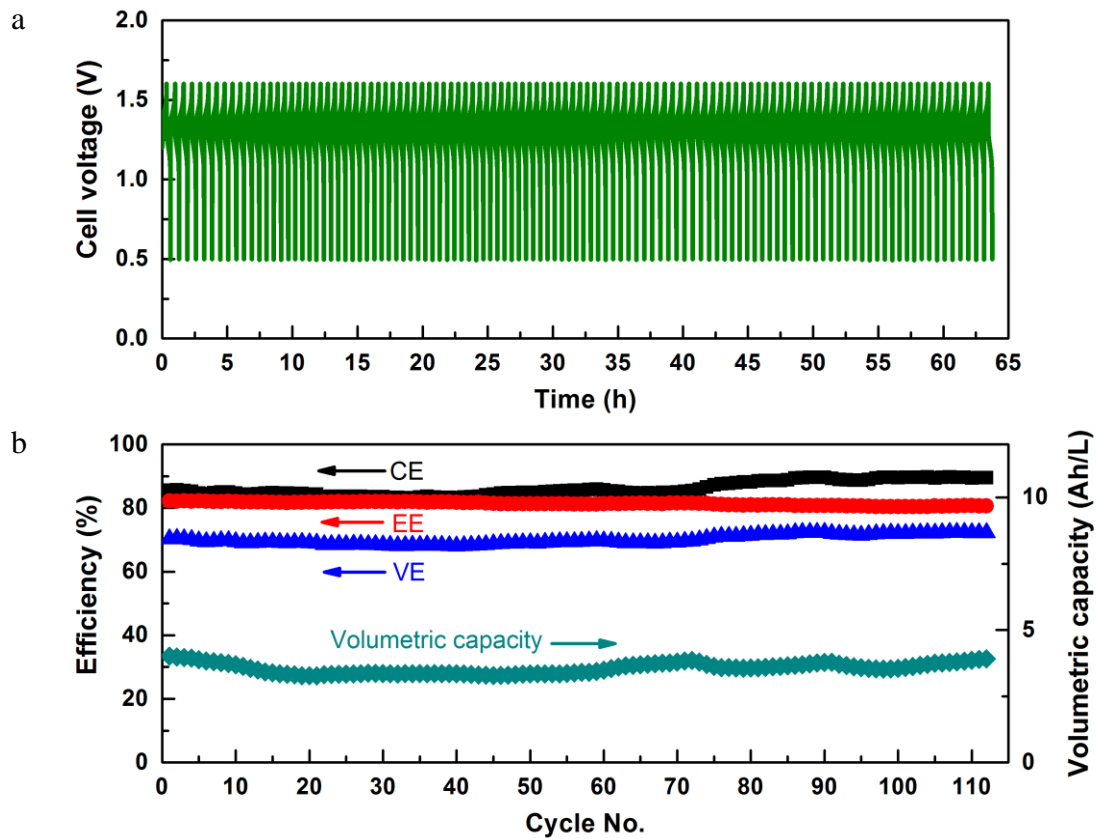


Figure 3.7 (a) Cell voltage of 110-cycle test of the all-Fe RFB at 40 mA/cm^2 . (b) Coulombic efficiency (CE), voltage efficiency (VE), energy efficiency (EE) and discharge capacity of each cycle in the same 110-cycle test of the all-Fe RFB.

3.4 Challenges

3.4.1 Relatively Low Coulombic Efficiency

Relatively low CE was observed in the cycle test and also reported in the literature for the Fe-TEOA redox pair^[155, 158].

As shown in Figure 3.8, electrode potential measurement in the end of discharge process during discharge process reveals that $\text{Fe}(\text{CN})_6^{3-}/\text{Fe}(\text{CN})_6^{4-}$ redox pair is the limiting side, which confirms that the shortage of oxidative species in positive electrolyte is responsible for CE loss.

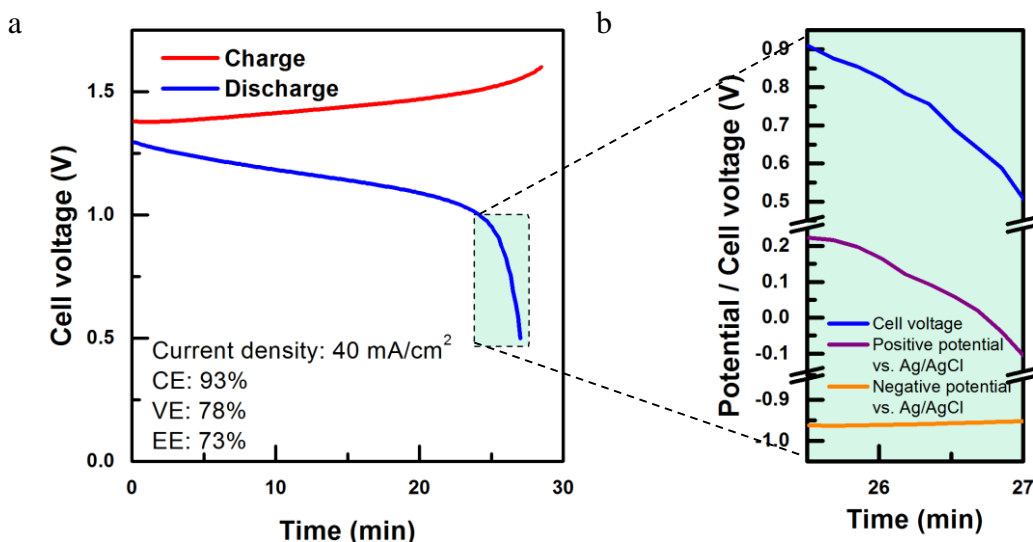


Figure 3.8 (a) Cell voltage curve of a charge-discharge test of all-Fe RFB at 40 mA/cm², and (b) zoomed-in cell voltage, positive and negative potential vs. Ag/AgCl reference electrode during the end of the discharge process, as indicated in the green rectangle in Figure 3.8 (a). The decrease of positive potential indicates the positive side is the dominating cause for the cell voltage drop and therefore the coulombic efficiency loss.

Oxygen evolution reaction (OER) as a side reaction on the positive electrode can be excluded for the shortage of oxidative species; the symmetrical cell study of $\text{Fe}(\text{CN})_6^{3-}/\text{Fe}(\text{CN})_6^{4-}$ redox pair did not have any CE loss even at high overpotential (CE = 100%, Figure 3.9). The crossover of $\text{Fe}(\text{CN})_6^{3-}$ species towards negative electrode can also be excluded. No new ¹³C NMR signals were observed in the

negative electrolyte after 20 cycles of testing (Figure 3.10a). The ^{13}C NMR spectra suggest that the permeation coefficient of $\text{Fe}(\text{CN})_6^{3-}$ across a Nafion 212 membrane is less than $1 \times 10^{-11} \text{ cm}^2 \text{ s}^{-1}$ (Figure 3.11).

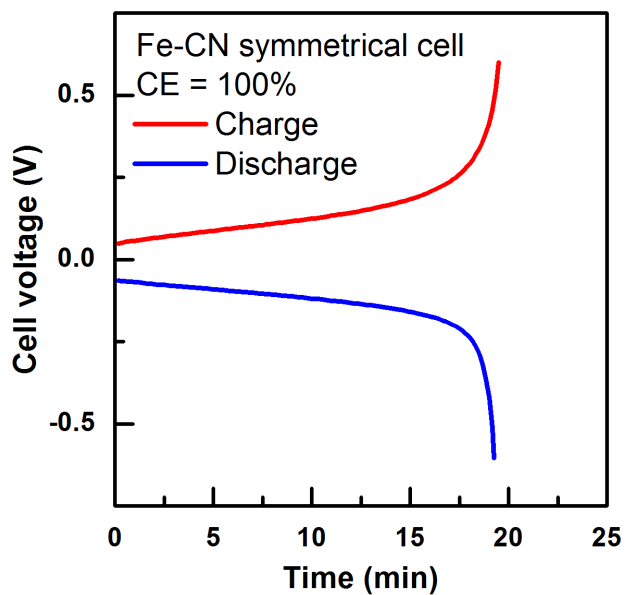


Figure 3.9 Cell voltage curve of the Fe-CN symmetrical cell. CE remains at 100%, indicating no oxygen evolution side reaction or crossover.

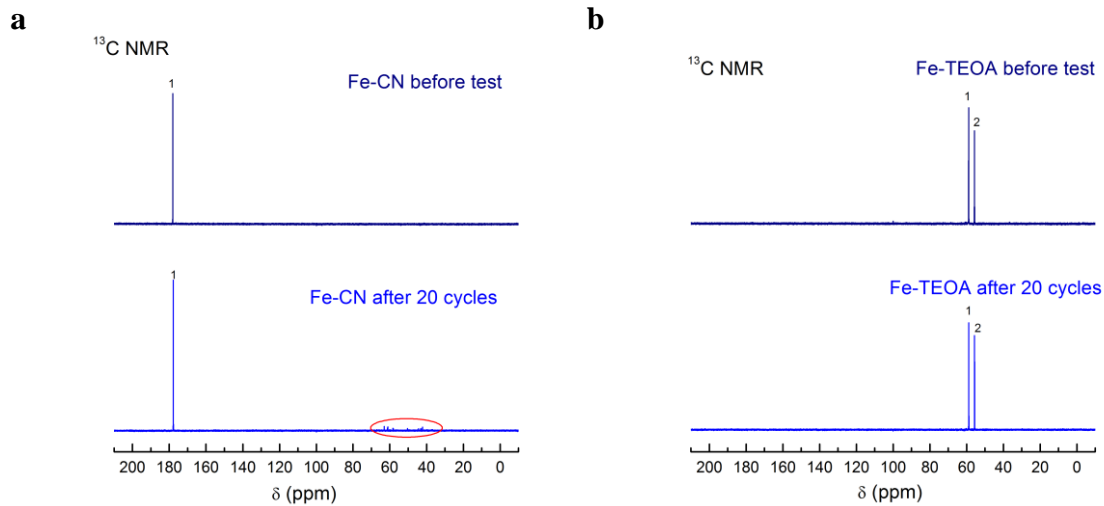


Figure 3.10 ^{13}C NMR spectra of positive (a) and negative (b) electrolytes before and after cycle testing of an all-soluble all-Fe RFB. A number of new peaks showed up in the positive electrolyte after 20 cycles, as enclosed in the red circle, whereas no new peaks were observed for negative electrolyte after testing.

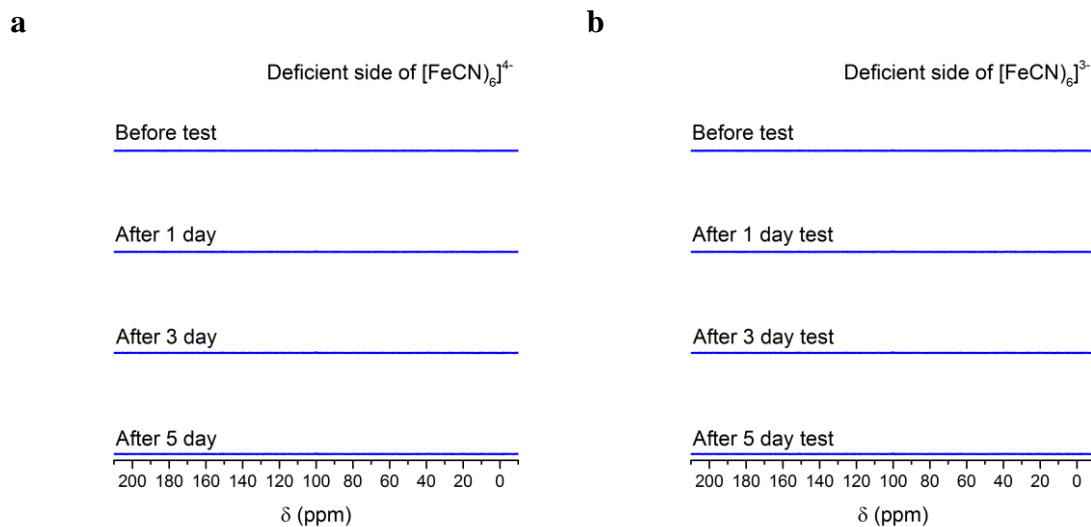


Figure 3.11 ^{13}C NMR spectra of electrolyte of the deficient side of a permeation cell with the enriched side being (a) $\text{Fe}(\text{CN})_6^{4-}$ and (b) $\text{Fe}(\text{CN})_6^{3-}$. No $\text{Fe}(\text{CN})_6^{4-}$ or $\text{Fe}(\text{CN})_6^{3-}$ was detected over five days. No peaks were detected during 5 days of testing. Since the lowest possible concentration that could be detected by NMR spectroscopy is 0.01 M, the permeation coefficient was then estimated to less than $1 \times 10^{-11} \text{ cm}^2/\text{s}$, by assuming the concentration after 5-day test is below 0.01 M.

The crossover of $[\text{Fe}(\text{TEOA})\text{OH}]^-$, $[\text{Fe}(\text{TEOA})(\text{OH})]^{2-}$, and/or free TEOA in the negative electrolyte is the key reason for CE loss, as evidenced by the ^{13}C NMR spectroscopic results for the positive electrolyte before and after the cycle test (Figure 3.10b). The permeation coefficients of $[\text{Fe}(\text{TEOA})\text{OH}]^-$, $[\text{Fe}(\text{TEOA})(\text{OH})]^{2-}$, TEOA are quantitatively studied with both ^{13}C NMR spectroscopy and inductively coupled plasma optical emission spectrometry (ICP-OES, Figure 3.12). The ^{13}C NMR spectrums of coordinated TEOA and free TEOA are indistinguishable; therefore, the total TEOA crossover rate for both $[\text{Fe}(\text{TEOA})\text{OH}]^-$ and $[\text{Fe}(\text{TEOA})(\text{OH})]^{2-}$ was measured by ^{13}C NMR test. The crossover rates of $[\text{Fe}(\text{TEOA})\text{OH}]^-$ and $[\text{Fe}(\text{TEOA})(\text{OH})]^{2-}$ were obtained by measuring the iron element crossover with ICP-OES. The crossover rate of free TEOA in each case can then be calculated by subtracting coordinated TEOA from the total TEOA.

It is possible to derive that the concentration of crossover species follows Eq.

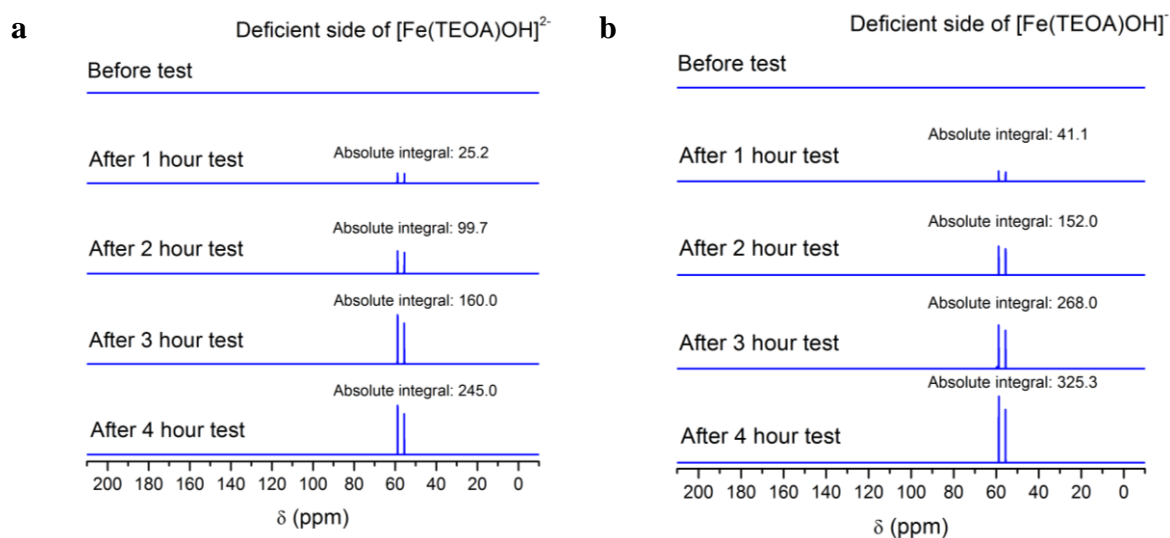
3.1.

$$V_B \frac{dC_B(t)}{dt} = A \frac{P}{L} \Delta C \quad (\text{Equation 3.1})$$

Where C_A is the concentration of the enriched side, C_B is the concentration of the deficient side, V_B is the volume of the deficient side, A is membrane area, L is

membrane thickness, and ΔC is the concentration difference between the enriched and deficient sides.

Given the experimental conditions, V_B and C_A can be assumed as constant. Since C_B is negligible compared to C_A , the driving force ΔC can also be treated as constant. The permeation coefficient of both free TEOA and the Fe-TEOA complex can then be obtained by a linear fitting of C_B vs. time for total TEOA and coordinated TEOA, respectively, as shown in Figure 3.12.



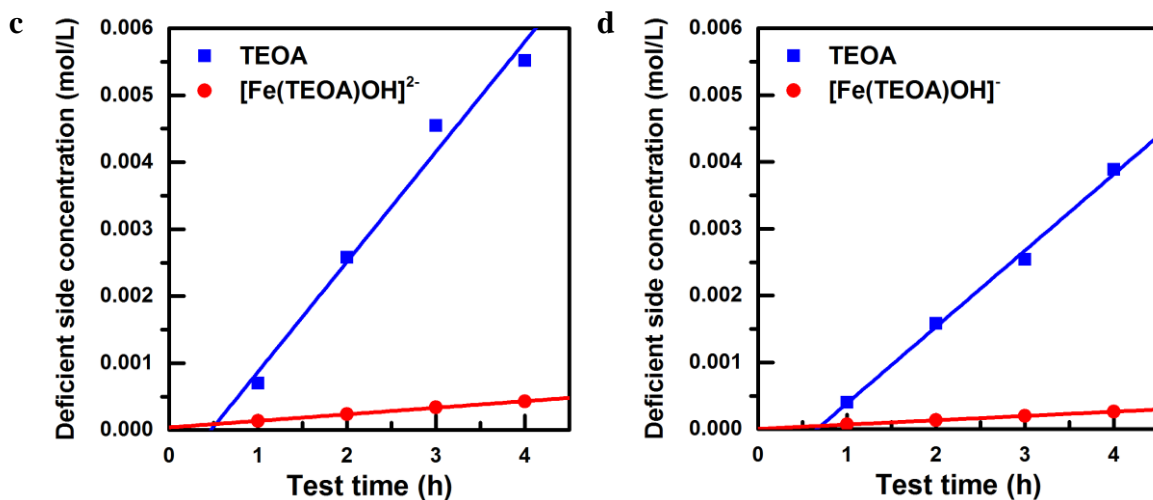


Figure 3.12 ¹³C NMR spectra of electrolyte of the deficient side of a permeation cell with the enriched side being (a) [Fe(TEOA)(OH)]²⁻ and (b) [Fe(TEOA)(OH)]⁻. The concentration of TEOA is converted by comparing the peak integral with that of the spectrum of standard TEOA solution, having known TEOA concentration. (c) Linear fitting of total TEOA and [Fe(TEOA)(OH)]²⁻ concentration vs. test time. (d) Linear fitting of total TEOA and [Fe(TEOA)(OH)]⁻ concentration vs. test time.

The permeation coefficients of [Fe(TEOA)OH]⁻, [Fe(TEOA)OH]²⁻, and free TEOA are listed in Table 3.4. The results further confirmed that free TEOA is the major crossover species. This identification is understandable, since free TEOA has higher permeation coefficient (2.9–4.4 times) and larger driving force as well (5 times, 1 mol L⁻¹ for free TEOA vs. 0.2 mol L⁻¹ for [Fe(TEOA)OH]⁻ or [Fe(TEOA)(OH)]²⁻).

Table 3.4 Permeation coefficient of [Fe(TEOA)OH]⁻, [Fe(TEOA)OH]²⁻, and free TEOA.

	[Fe(TEOA)OH] ⁻	[Fe(TEOA)OH] ²⁻	Free TEOA
--	---------------------------	----------------------------	-----------

Permeation coefficient (cm ² s ⁻¹)	5.1 × 10 ⁻¹⁰	3.4 × 10 ⁻¹⁰	1.5 × 10 ⁻⁹
--------------------------------------------------------------	-------------------------	-------------------------	------------------------

After crossover, the free TEOA could be oxidized either electrochemically on the electrode at high overpotentials, or chemically by Fe(CN)₆³⁻. The electrochemical oxidation of free TEOA is confirmed by the CV experiments in which free TEOA is oxidized at electrode potentials greater than 0.4 V vs. Ag/AgCl (Figure 3.13a). The addition of free TEOA into the dilute Na₄Fe(CN)₆ solution significantly changed the CV behavior at the potential region below 0.4 V vs. Ag/AgCl, suggesting that a direct chemical reaction between TEOA and Fe(CN)₆³⁻ can also take place (Figure 3.13a). The reaction rate between Fe(CN)₆⁴⁻ and TEOA was also studied by CV. It could be derived that a typical CV curve for a catalytic reaction shows a limiting value of current i_{∞} given by Eq. 3.2^[166].

$$i_{\infty} = nFAC_{Fe(CN)_6^{3-}}^* C_{TEOA}^* (Dk)^{1/2} \quad (\text{Equation 3.2})$$

Where n is the number of electrons transferred in electrochemical reaction, F is Faraday's constant, $C_{Fe(CN)_6^{3-}}^*$ is the concentration of ferricyanide, C_{TEOA}^* is the concentration of TEOA, D is the diffusion coefficient of TEOA^[167], k is the kinetic constant of reaction between TEOA and Fe(CN)₆³⁻.

The reaction rate constant can therefore be calculated by a linear fitting of TEOA concentration as a function of limiting current. CV studies at different TEOA concentrations and the linear fitting of TEOA concentration with limiting current are shown in Figure 3.13b. Since TEOA will further undergo direct electrochemical reaction at higher potentials, the limiting current was chosen using the plateau region

at 0.4 V vs. Ag/AgCl. The overall rate constant of the reaction is determined to be $1.0 \times 10^{-7} \text{ s}^{-1}$, assuming the overall reaction is a first-order reaction (Figure 3.13b).

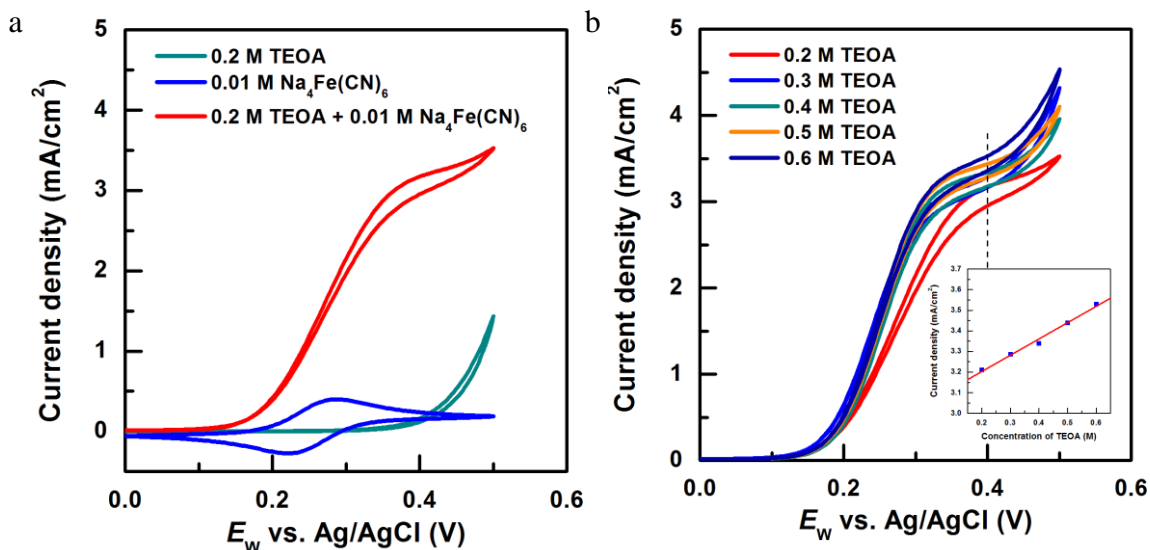
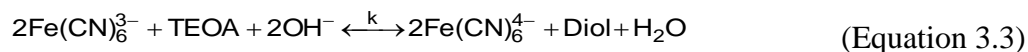
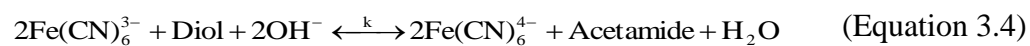


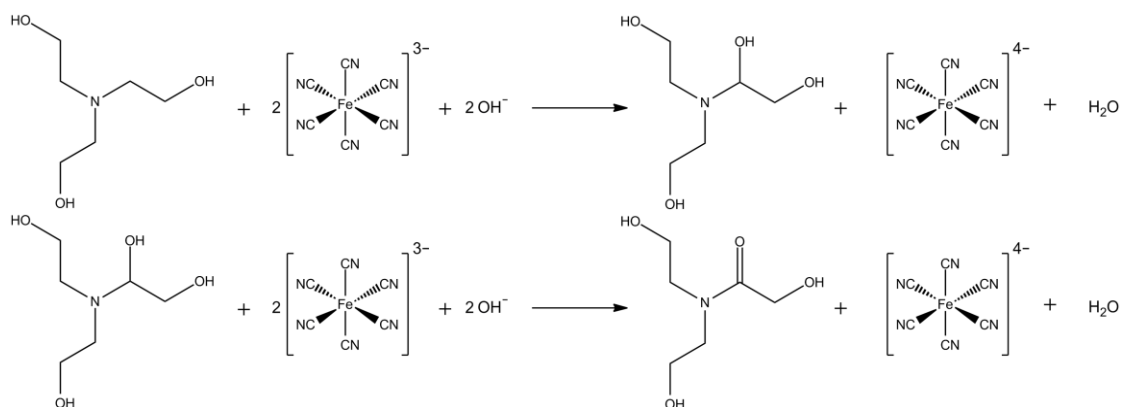
Figure 3.13 (a) CV scan on glassy carbon electrode at 5 mV/s from 0 V to 0.5 V vs. Ag/AgCl of 0.01 M $\text{Na}_4\text{Fe}(\text{CN})_6$ (blue curve), 0.2 M TEOA (green curve), 0.01 M $\text{Na}_4\text{Fe}(\text{CN})_6$ and 0.2 M TEOA (red curve). All electrolytes are supported with 1 M NaOH. The rising current at $E_w > 0.4 \text{ V vs. Ag/AgCl}$ confirms the electrochemical oxidation of TEOA on electrode surface (green curve). (b) CV scan of on glassy carbon electrode at 5 mV/s from 0 to 0.5 V vs. Ag/AgCl of 0.01 M $\text{Na}_4\text{Fe}(\text{CN})_6$ with different TEOA concentrations from 0.1 M to 0.6 M. The current density at 0.4 V vs. Ag/AgCl of forward scan was chosen as limiting current density. Inset: linear fitting of limiting current density vs. TEOA concentration.

The possible chemical reactions between TEOA and $\text{Fe}(\text{CN})_6^{3-}$ are proposed in Eq. 3.3 and 3.4, and represented in Scheme 1. The reaction products were confirmed via $^1\text{H NMR}$, by comparing the relative peak position of products (Figure 3.14).





where diol represents 1-(bis(2-hydroxyethyl)amino)ethane-1,2-diol, and acetamide represents 2-hydroxy-N,N-bis(2-hydroxyethyl)acetamide.



Scheme 1. Proposed possible reaction scheme of TEOA oxidation in $\text{Fe}(\text{CN})_6^{3-}$ electrolyte as shown in Eq. 3.3 and 3.4.

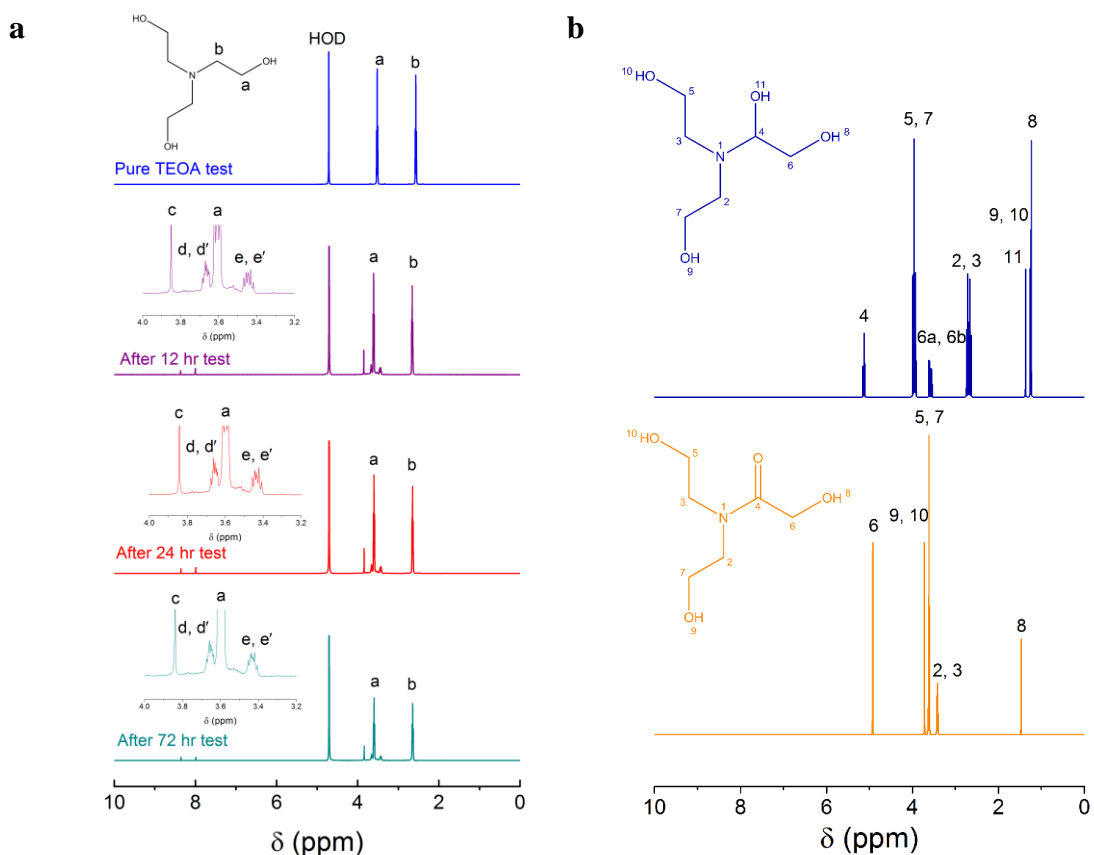


Figure 3.14 (a) ¹H NMR spectra of solutions containing 0.5 M K₃Fe(CN)₆, 0.2 M TEOA and 0.5 M KOH with test time. Inset: zoomed-in figure of ¹H NMR between chemical shifts of 4.0 and 3.2 ppm. Peaks a and b are attributed to α and β hydrogen in TEOA. Peaks c, d and e are possibly due to the oxidation at α-carbon and the formation of 1-(bis(2-hydroxyethyl)amino)ethane-1,2-diol and 2-hydroxy-N,N-bis(2-hydroxyethyl)acetamide. (b) Predicted ¹H NMR spectrum of 1-(bis(2-hydroxyethyl)amino)ethane-1,2-diol (upper) and 2-hydroxy-N,N-bis(2-hydroxyethyl)acetamide (lower). It is possible that the oxidation takes place at α-carbon and generates 1-(bis(2-hydroxyethyl)amino)ethane-1,2-diol. Diol can be further oxidized by Fe(CN)₆³⁻ and produces 2-hydroxy-N,N-bis(2-hydroxyethyl)acetamide. The shape and relative peak position of the obtained degradation product matches the predictions for the proposed product.

3.4.2 High Cell Resistance

Based on an impedance test of the full cell, as shown in Figure 3.15a, the charge-transfer resistance is $0.75 \Omega \cdot \text{cm}^2$, while the ohmic resistance ($2.6 \Omega \cdot \text{cm}^2$) is more than 3 times as large as the charge transfer resistance. The iR -free polarization was calculated and shown in Figure 3.15b, which demonstrates a peak power density near 800 mW cm^{-2} . Our experimental cell has an MEA structure, and thus the electrodes bring negligible resistances^[72]. As such, the large membrane resistance is the sole reason for this high internal resistance. The resistance of Nafion 212 membrane was measured in solutions of 3 M NaOH; 3 M NaOH and 2 M TEOA; and 3 M NaOH, 2 M TEOA and 0.4 M FeCl_3 . The results clearly show that the both Fe-TEOA and free TEOA can contaminate the Nafion membrane, leading to increased membrane resistance, as shown in Figure 3.16. This result is not surprising, since the absorption of alkylamine by cation exchange membrane has also been widely reported in other applications such as carbon dioxide transport^[168, 169]. It can be reasonably expected that TEOA-tolerant cation-exchange membranes will substantially improve the cell performance.

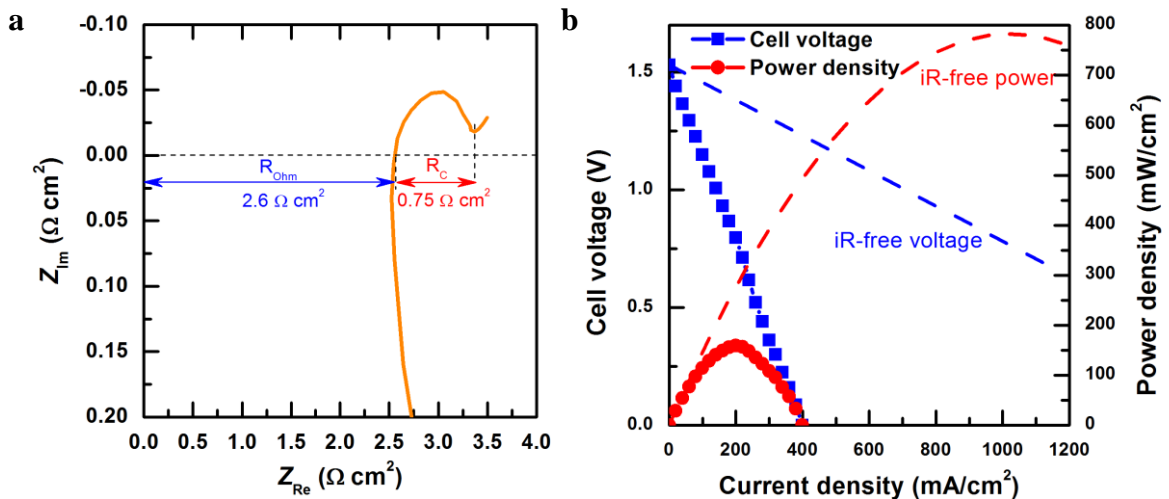


Figure 3.15 (a) Impedance of all-Fe RFB showing ohmic resistance (R_{ohm} , depicted in blue color) and charge transfer resistance (R_c , red). The ohmic resistance accounts for the major part of total resistance. (b) Experimental (solid) and predicted iR -free (dashed) polarization curve of all-Fe RFB at 70% State of Charge (SOC).

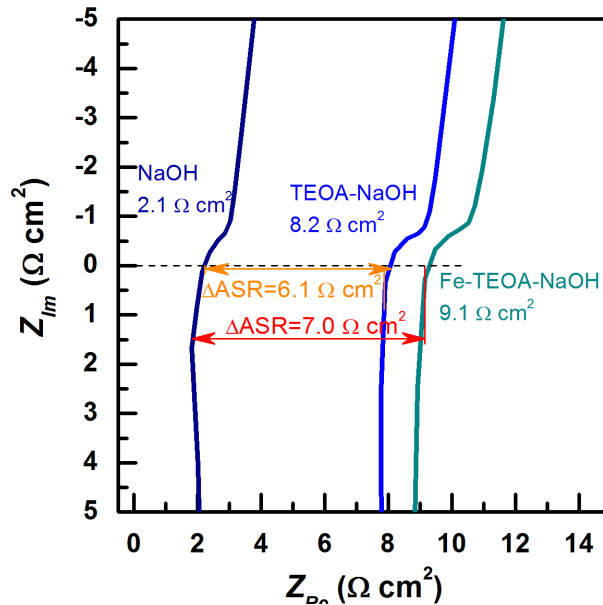


Figure 3.16 Impedance test of a symmetrical cell with three different electrolytes: 3 M NaOH (dark blue), 2 M TEOA in 3 M NaOH (blue), and 0.4 M $FeCl_3$, 2 M TEOA in 3 M NaOH (green).

3.5 Concluding Remarks

We introduced an all-soluble all-iron redox-flow battery by combining $[Fe(TEOA)OH]^-/[Fe(TEOA)(OH)]^{2-}$ and $Fe(CN)_6^{3-}/Fe(CN)_6^{4-}$ in a simple single-IEM cell configuration. The all-soluble all-Fe RFB demonstrated good performance (discharge power density $>160 \text{ mW cm}^{-2}$) and durability (110 cycles with stable efficiency and capacity). We identified that the major challenge in this all-soluble all-Fe RFB is the crossover of free TEOA ligand. The performance of the all-soluble all-

Fe RFB may be improved by using TEOA-tolerant membranes. In addition to the all-soluble all-iron RFB, there are many other possibilities to design all-soluble all-(redox-active)-element RFBs with redox pairs based on metal ligands.

Chapter 4

A MEMBRANE-LESS ZINC-FERROCENE REDOX FLOW BATTERY BASED ON IMMISCIBLE ORGANIC-INORGANIC ELECTROLYTES

4.1 Introduction

Rechargeable batteries rely on the physical separation of mutually reactive species to extract electrical energy from indirect electrochemical reactions. Conventional rechargeable batteries use liquid electrolyte to separate two solid electrodes that act as energy storing material. Redox flow batteries (RFBs), on the other hand, introduce a solid electrolyte (i.e., an ion-exchange membrane, IEM) as a separator, which changes the energy storing material from solid electrodes to liquid electrolytes with two soluble redox pairs^[18]. This gives RFBs excellent flexibility. Such independent tuning of energy storage capacity and power is regarded as a significant advantage when compared with other rechargeable batteries^[6]. However, the performance and cost of RFBs are limited by their large internal resistances and expensive membranes^[65, 68]. To address this issue, designing a membrane-less RFB has been a new approach in recent RFB development, and membrane-less all-vanadium^[115] (all-V) and hydrogen-bromide^[117] (H-Br) RFBs have been demonstrated with appreciably reduced internal resistance. However, currently, membrane-less RFBs do not provide a fundamentally stable solution for the separation of two redox pairs. The separation is based solely on the laminar flow of two electrolytes. Crossover of redox species, which has already long been a prominent issue in conventional membrane based RFB, then becomes even more pronounced in membrane-less design.

Consequently, low coulombic efficiency and contamination of redox species are still big concerns in membrane-less RFBs. In addition, laminar flow cell requires exquisite engineering of flow rate and cell structure and adds extra constraints to cell operation. Fundamental solutions to this crossover problem need another method to separate redox pairs in membrane-less RFB.

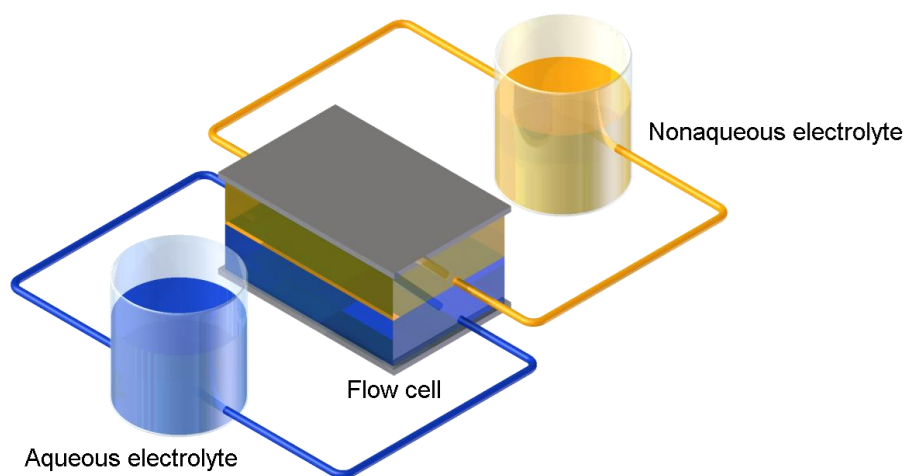
In this work, we demonstrate a new membrane-less RFB design based on the immiscibility of aqueous and non-aqueous electrolytes on the negative and positive sides, respectively, as shown in Figure 4.1a. Different from the laminar flow cell, the two electrolytes in this RFB are naturally separated from each other. Therefore, no membrane is needed. The redox pair in the organic electrolyte is only soluble in the organic solvent, whereas the redox pair in the aqueous phase is only soluble in water; no crossover is expected by design. In order to maintain ionic conductivity, at least one electrochemically inactive ion, to serve as a charge carrier, should be soluble in both the organic and inorganic phases. It is also apparent that either the reductive species in the negative redox pair, or the oxidative species in the positive redox pair should be insoluble, to prevent direct interfacial chemical reaction. One design satisfying these constraints is a Zinc/Ferrocene (Zn/Fc) RFB based on two immiscible electrolytes, shown in Figure 4.1b. Butyl acetate (BuAcO) is used as the solvent in the organic phase, dissolving both Ferrocenium/Ferrocene (Fc^+/Fc), the positive redox pair, and an hydrophobic ionic liquid (Aliquat[®] 336, mixture of tricapyrylmethylammonium chloride and trioctylmethylammonium chloride), the supporting salt. In the aqueous phase, the Zn^{2+}/Zn redox pair is used via dissolving ZnCl_2 in water. The Cl^- commutes between the organic and inorganic phases during

charge and discharge processes. The positive and negative electrode reactions, shown below, yield an overall cell voltage of 1.16 V.



As shown in Figure 4.1a, the cell must be placed horizontally due to gravity, and the electrolyte flows in and out from the side of cell. Since the density of butyl acetate is lighter than water ($\rho_{\text{BuAcO}} = 0.8 \text{ kg/L}$ vs $\rho_{\text{H}_2\text{O}} = 1.0 \text{ kg/L}$), the organic electrolyte flows on top of the aqueous electrolyte.

a



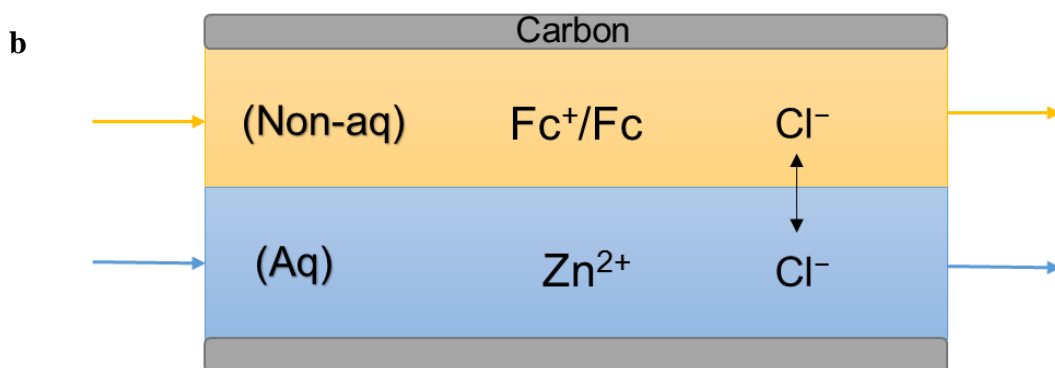


Figure 4.1 (a) Schematic of a membrane-less RFB based on immiscible organic-inorganic electrolytes. (b) Design of the membrane-less zinc-ferrocene RFB.

4.2 Experiment and Method

Chemical reagents. Chemicals were used as-received from different vendors: zinc chloride (ZnCl_2 , Sigma-Aldrich, 99%), Aliquat[®] 336 (Sigma-Aldrich, 99%), butyl acetate (99%, Sigma-Aldrich), ferrocene (MP Biomedicals), ferrocenium tetrafluoroborate (technical grade, Sigma-Aldrich), copper foil (thickness 0.25 mm, 99.98%, Sigma-Aldrich).

Solubility test. Six samples of 20 ml solution with different mole ratios of butyl acetate over Aliquat[®] 336 were prepared. Ferrocene was added into each sample every 0.10 g until precipitate was observed that did not dissolve within 24 hours. The solution was continuously stirred during the test.

Conductivity test. Seven samples of 20 ml solution with different mole ratios of butyl acetate over Aliquat[®] 336 were prepared. Conductivities were then directly measured by a conductivity meter (Fisher Scientific, AB100).

Cyclic voltammetry test. Cyclic voltammetry (CV) was conducted with a three-electrode configuration in a three-neck flask. A glassy carbon disk (3 mm dia.),

platinum wire, and silver wire were used as the working, counter and reference electrodes, respectively. CV testing was carried out by a multichannel potentiostat (VMP2, Princeton Applied Research).

Cell setup and cycle test. The cell was set up as shown in Figure 4.2. The electrolyte was pumped into the cell through the flow channel inside the upper PTFE block (not shown in figure). The cell was placed horizontally during testing. Cycle testing was carried out by a battery test station (Arbin, BT2000).

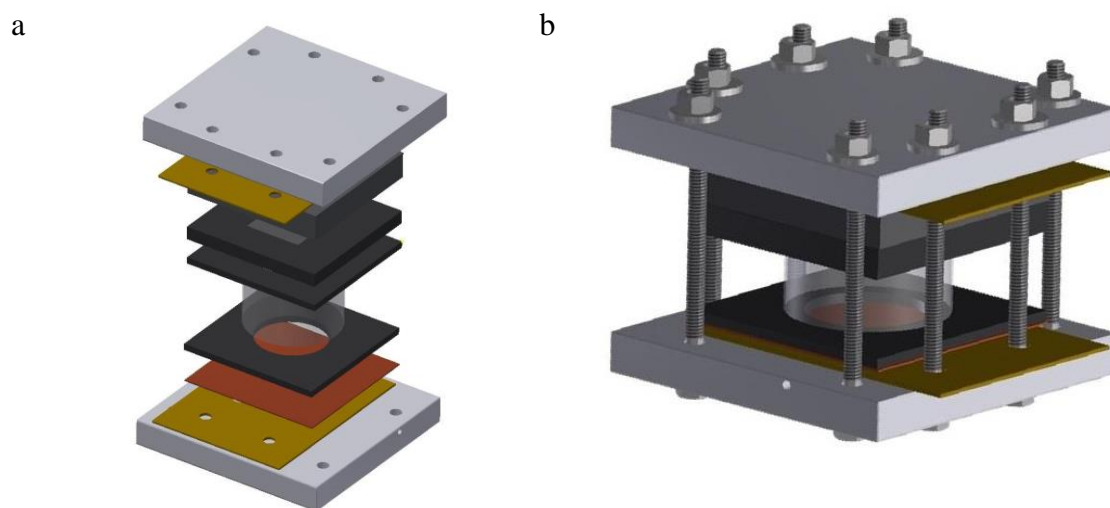


Figure 4.2 (a) Schematic of a cylindrical cell. From top to bottom: PTFE block, gold plate electrode, copper plate electrode, EPDM rubber gasket, polypropylene cylinder, EPDM rubber gasket, carbon foam electrode, fluorosilicone rubber gasket, carbon paper electrode, carbon block, gold plate electrode, and PTFE block. (b) Schematic of an assembled cylindrical cell.

4.3 Results and Discussion

Zinc electrolytes have been studied extensively in aqueous zinc-based battery applications. Therefore, in this work, we mainly focused on the study of the organic

electrolyte to optimize Zn-Fc RFB performance; our aims were to maximize ferrocene solubility as well as electrolyte conductivity. To achieve higher energy density, the solubility of ferrocene in organic electrolyte should be kept high. The solubility of ferrocene in pure butyl acetate has been measured to be 0.46 M^[170], but it is altered after the addition of Aliquat[®] 336 into butyl acetate, as shown in Figure 4.3a. The increase of Aliquat[®] 336 decreases ferrocene solubility and a linear relationship between molar concentration of butyl acetate was found. The solubility study suggests lower concentration of Aliquat[®] 336 should be used when possible. Another important issue for organic electrolytes is their low conductivities compared to those of aqueous electrolytes, whose consequence is substantially large internal resistance of the cell. Figure 4.3b shows the conductivity of organic electrolytes as a function of mole percent butyl acetate. The conductivity peaks at 70 mol % butyl acetate mole percent. The subsequent decrease of conductivity at higher mole percentages is attributed to the increase of electrolyte viscosity, due to the high viscosity of Aliquat[®] 336 ($\mu=1500$ mPa·s^[171]). Considering even the peak conductivity only reaches about 110 μ S/cm, 70 mol % butyl acetate is chosen for future tests to maximize system conductivity.

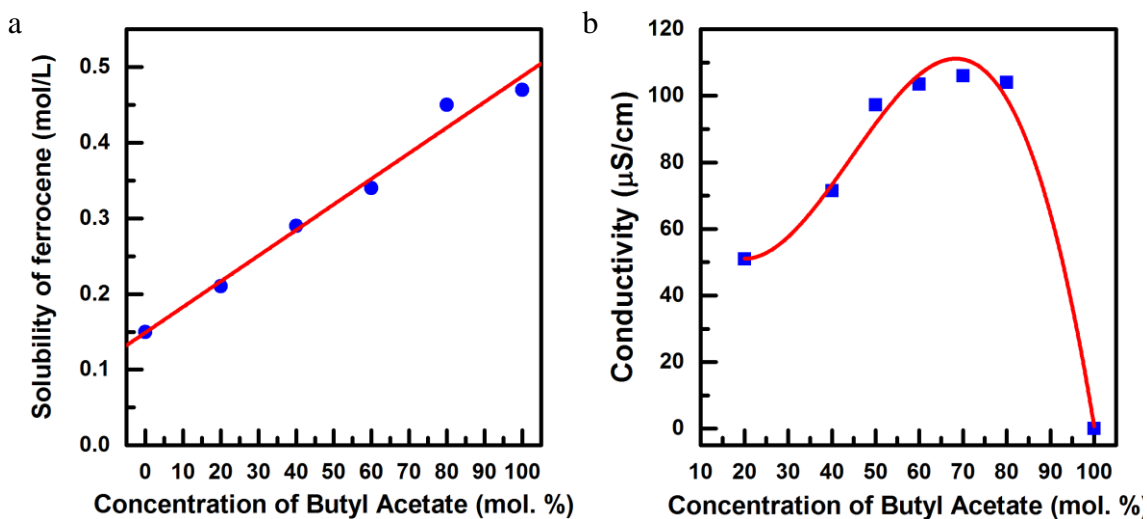


Figure 4.3 (a). Solubility of ferrocene along with mole percentage of butyl acetate in organic electrolyte. (b). Conductivity of organic electrolyte versus mole ratio of butyl acetate.

The kinetics of ferrocene redox pair is known to be facile in many non-aqueous systems^[172]. Cyclic voltammetry was carried out in butyl acetate electrolyte with 30% mole Aliquat[®] 336 as the supporting salt. As shown in Figure 4.4a, the background electrolyte does not incur any redox peak, indicating the stability of butyl acetate and Aliquat[®] 336 in the redox-active region of the ferrocene redox pair. CVs at different scan rates were performed to calculate the kinetic constant and diffusion coefficients of ferrocenium ion and ferrocene, as shown in Figure 4.4b. The results are listed in Table 4.1. The diffusion coefficients for both ferrocenium and ferrocene are smaller than those typical for ions in an aqueous electrolyte ($\sim 10^{-9}$ cm²/s), mostly as a result of the increased viscosity from adding Aliquat[®] 336. The kinetics of the ferrocene

redox pair on a carbon electrode is already facile compared with many other aqueous redox pairs, *e.g.*, $k_0(\text{VO}_2^+/\text{VO}^{2+}) = 3 \times 10^{-7} \text{ cm/s}$ ^[173]; therefore, it requires no catalyst in the cell setup.

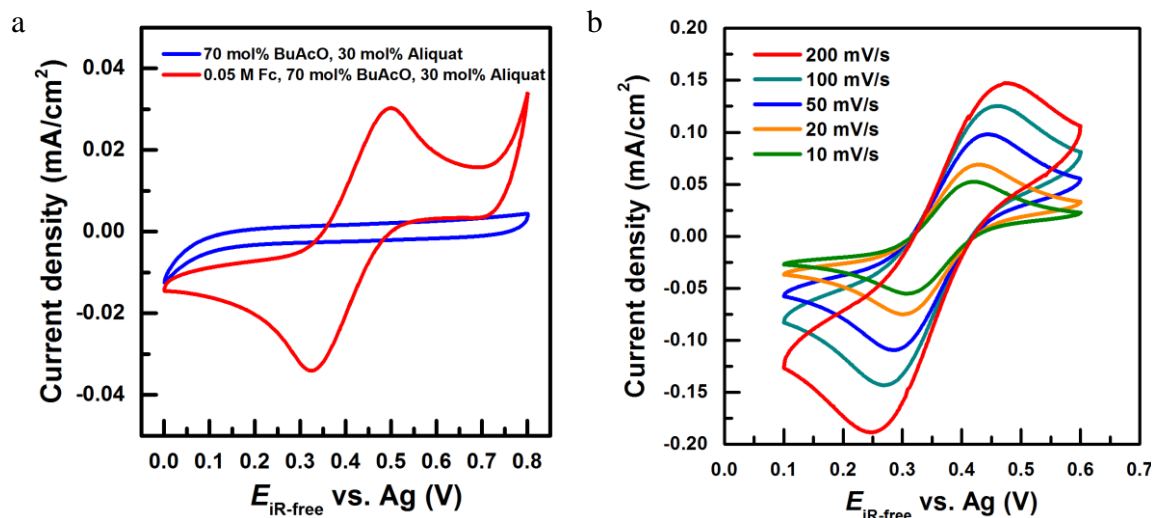


Figure 4.4 (a) Cyclic voltammogram of blank electrolyte (70 mol% Butyl Acetate, 30 mol% Aliquat[®] 336) and ferrocene solution (0.05 M Fc in 70 mol% Butyl Acetate, 30 mol% Aliquat[®] 336) on a glassy carbon electrode. (b) CV of ferrocene electrolyte (0.05 M Fc, 0.05 M FcBF₄ in 70 mol% Butyl Acetate, 30 mol% Aliquat[®] 336) at different scan rates on glassy carbon electrode.

Table 4.1 Diffusion coefficients of ferrocenium (D_O) and ferrocene (D_R), and the kinetic constant (k^0) of Fc⁺/Fc redox pair. The kinetic constant is calculated based on the method of Nicholson^[174].

D_O (cm ² /s)	D_R (cm ² /s)	k^0 (cm/s)
8.1×10^{-10}	4.3×10^{-10}	1.2×10^{-5}

A stationary cell was set up to prove the feasibility of the Zn-Fc RFB. A 20-cycle test was carried out at constant current density of 0.1 mA/cm^2 and cut-off voltages of 1.35 V for charge and 0 V for discharge (Figure 4.5a). The corresponding coulombic efficiency (CE), voltage efficiency (VE), energy efficiency (EE) and capacity are shown in Figure 4.5b. Both efficiency and capacity remain constant over the 20-cycle test, which confirms the stability of this system. Average CE, VE and EE are 82%, 62% and 51%, respectively.

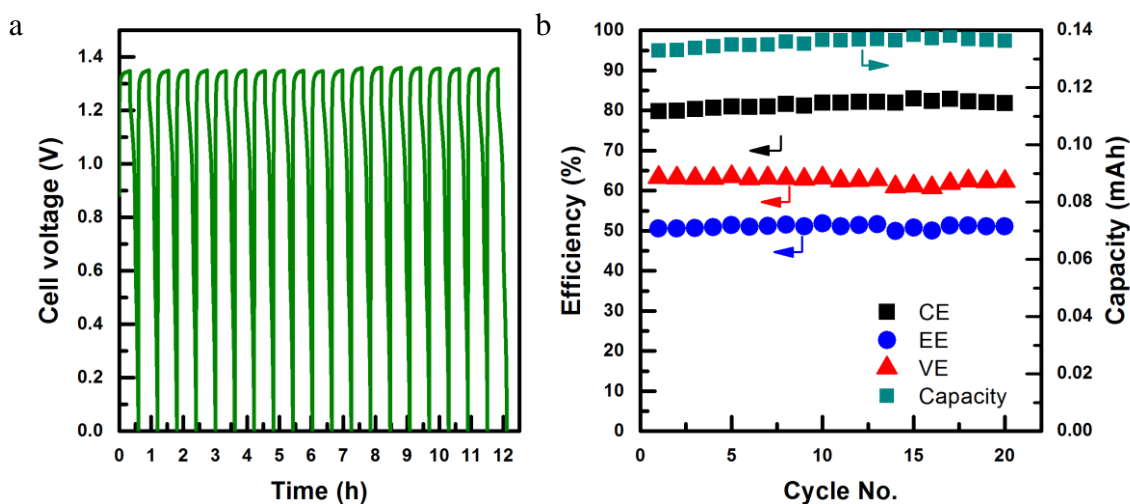


Figure 4.5 (a) A 20-cycle test of Zn-Fc membrane-less RFB. The cut-off voltage was set at 1.35 V for charge and 0 V for discharge. (b) Coulombic, voltage, and energy efficiencies and capacity for each cycle in 20-cycle test.

Coulombic efficiency is not very high compared to the state-of-art aqueous RFBs, possibly due to the small amount of solubility of ferrocenium in water. Ferrocenium generated at the positive electrode gradually transported from the organic phase into the aqueous phase, reacting with zinc and causing coulombic efficiency

loss. The voltage efficiency loss was mostly attributed to the large internal resistance of the cell: area-specific resistance of the cell was measured to be $810 \Omega \cdot \text{cm}^2$ (Figure 4.6). Considering the large thickness of the organic electrolyte layer (1 cm) in current design and its low conductivity, high internal resistance is not surprising. Internal resistance could be slashed by reducing the thickness of the organic electrolyte layer and choosing a highly-conductive supporting salt. Such changes require detailed engineering work and lie beyond the scope of this proof-of-concept work.

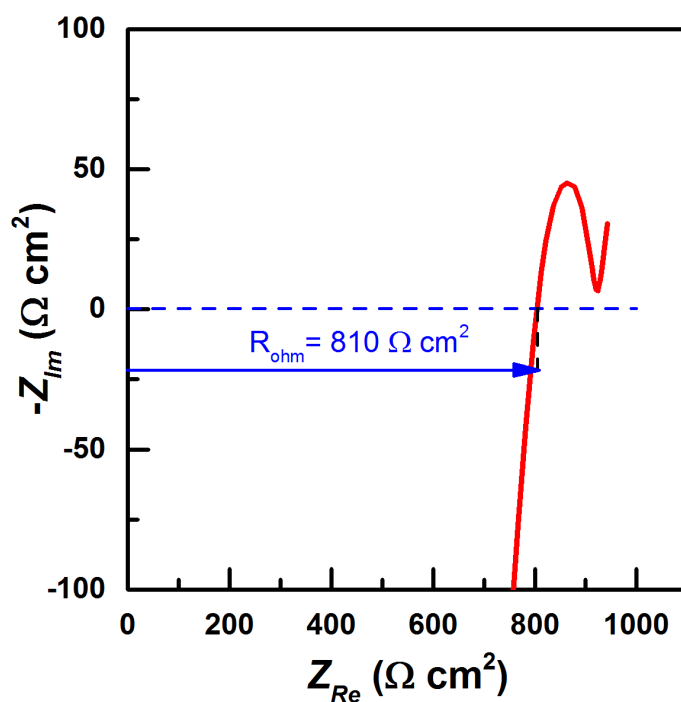


Figure 4.6 Nyquist plot of Zn-Fc RFB in an impedance test. Ohmic resistance is measured to be $810 \Omega \cdot \text{cm}^2$. Large internal resistance is due to the large thickness and low conductivity of the organic electrolyte.

4.4 Concluding Remarks

In this proof-of-concept study, we have demonstrated a membrane-less RFB design based on immiscible non-aqueous and aqueous electrolytes. The hydrophobic organic electrolyte is thermodynamically immiscible with the aqueous solution, such that the system requires no membrane. We chose Zn^{2+}/Zn in an aqueous phase and Fc^+/Fc in a butyl acetate phase to construct a Zn-Fc RFB as an example and successfully demonstrated its feasibility. Though much engineering is still needed to improve cell performance, this preliminary work adds to the methods for separating redox pairs in rechargeable battery and presents a new membrane-less construct for RFB design.

Chapter 5

CONCLUSIONS AND PERSPECTIVES

5.1 Summary of Conclusions

Three different RFB configurations have been explored in this dissertation: double-membrane, single-membrane and membrane-less structures.

The double-membrane RFB aims to solve the limitations of the single-membrane design and to improve the versatility of RFBs in incorporating more redox pairs and supporting electrolytes. A high-voltage Zn-Ce RFB was the initial trial. In this example, an unprecedented high cell voltage of 3.08 V was demonstrated by combining the redox pair with the lowest possible electrode potential in base and that with the highest possible electrode potential in acid. The Zn-Ce RFB shows stable open-circuit voltage and expected charge-discharge performance. However, the stability of the AEM in the highly oxidative cerium electrolyte was identified as the primary challenge for long-term durability. An alternative S-Fe RFB with lower cell voltage but extremely inexpensive redox materials was proposed and developed. The S-Fe RFB showed significantly improved durability compared with Zn-Ce RFB. However, its relatively low cell voltage (1.2 V) brings large penalties in cell efficiency and operation current density. After careful scrutiny of the Zn-Ce and S-Fe RFBs, Zn-Fe RFB emerged as a way to combine the advantages in the Zn-Ce and S-Fe RFBs and therefore provide the best balance between high cell voltage and low electrolyte cost. Study of the Zn-Fe RFB mainly focused on reducing the high internal resistance from

two membranes and an additional electrolyte compared with traditional RFBs. Specifically, engineering factors, such as middle electrolyte thickness, flow rate and operating current density, were studied and correlated with the internal resistance. The results suggest that a small middle electrolyte thickness, sufficiently high flow rate, and appropriate operating current density are required to successfully suppress concentration-polarization resistance and maintain the total resistance under a low level. The low internal resistance is a key enabler of high power density: the Zn-Fe RFB delivers high peak power density at 676 mW/cm^2 , the third highest among all RFBs, after all-V and H-Br RFB. The Zn-Fe RFB also shows good cycle performance, with high CE, VE, EE and low capacity loss. Its high performance and low-cost materials directly translate into low capital cost. An existing RFB cost model was adapted and extended to compare the costs of several notable RFBs. Indeed, the Zn-Fe RFB shows the lowest cost, which could reach the target set by U.S. Department of Energy for the 2023 term ($\$150/\text{kWh}$). Such a low cost would make Zn-Fe RFB very attractive for future commercial implementation. However, one important challenge remains for the Zn-Fe RFB and other double-membrane RFBs that use distinctive pHs on positive and negative sides. Namely, there is an inevitable crossover of acid and base through the respective membranes. The crossover of acid/base causes pH changes of the positive and negative electrolytes, the precipitation of redox materials, and the eventual failure of the double-membrane RFB. The crossover rates of acid and base through several commercial membranes have been measured. The results suggest that the state-of-the-art membranes cannot ensure both good performance and durability for double-membrane RFB simultaneously. The double-membrane RFB may require

another breakthrough in separator innovation to mitigate the acid/base crossover issue for further pilot testing and commercial practice.

A single-membrane RFB based on iron coordination chemistry was developed as an all-soluble all-iron RFB. It was demonstrated as the first RFB that takes advantage of the same element but different complexing agents on the positive (cyanide, CN) and negative (triethanolamine, TEOA) sides. The most attractive feature is that it is built on the same element, iron, and that both redox pairs being soluble. The use of the same element, iron, precludes the cross-contamination of metal ions, and guarantees the low element cost. Electrochemistry testing showed that both redox pairs have excellent kinetics, indicating negligible overpotential in the charge-discharge process. The all-soluble all-iron RFB shows good functionality and durability. A 110-cycle test has been successfully carried out with low performance loss. However, a relatively low coulombic efficiency (~90%) and unexpectedly high cell resistance ($>2.7 \Omega \cdot \text{cm}^2$) were observed in the charge-discharge cycle test and polarization test. Detailed studies were carried out to reveal the reason for high coulombic efficiency loss and internal resistance. It is found that the crossover of the complexing agent, TEOA, to the positive side is responsible for the coulombic efficiency loss, as TEOA could be oxidized on the positive side both chemically by ferricyanide species or electrochemically on the positive electrode. TEOA is also found to contaminate Nafion membrane and significantly increase the total internal resistance of the cell. To further improve the performance, the contamination of the complexing agent must be mitigated and solved. Nonetheless, we believe the all-soluble all-Fe RFB could serve as a good example to inspire more innovations in metal-organic based RFBs.

The membrane-less RFB was developed using immiscible organic-inorganic electrolytes. The membrane-less idea was inspired by the naturally separating oil/water system which requires no physical separator. Zinc (Zn^{2+}/Zn) in an aqueous phase and ferrocene (Fc^+/Fc) in a butyl acetate phase were chosen as the negative and positive redox pairs, and a proof-of-concept study was demonstrated based on the Zn-Fc RFB. The organic electrolyte was optimized for maximum conductivity and good solubility of ferrocene species. The charge-discharge test validated the membrane-less design and functionality of Zn-Fc RFB. The major challenges for Zn-Fc RFB is the large internal resistance ($>800 \Omega \cdot \text{cm}^2$), which is due to the thick organic layer and very low conductivity of organic electrolyte ($110 \mu\text{S}/\text{cm}$). The resistance could be further reduced by decreasing the thickness of the organic layer. Though much engineering work is still needed in order to improve cell performance, we believe this preliminary work broadens the methods available to separate redox pairs in rechargeable batteries and generates a new membrane-less construct for RFB design.

New designs and new chemistries are the main focus in this dissertation work. The double-membrane and membrane-less RFB designs could serve as two novel foundations for new redox chemistries and are not limited by the examples demonstrated in this dissertation work. The single-membrane based all-iron all-soluble RFB also provides a good example of the synergy between organic and inorganic chemistries in RFB. Though traditional RFBs, such as the all-V and Zn-Br RFBs, have led the way in maturity and commercialization, new design and chemistries like these are necessary catalysts for the continued evolution of RFBs.

5.2 Perspectives and Future Work

For all the RFBs explored in this dissertation, the Zn-Fe RFB is the one that holds the most promise for future development, if more advanced separators could be invented to prevent or significantly hinder the crossover of acid and base. An alternative route has been explored preliminarily, which uses a ceramic membrane, NaSICON, that solely conducts Na^+ and excludes all other ions by design. The acid/base crossover test shows no acid/base leak over a one-week test period. The NASICON membrane also demonstrated excellent stability: a 100-cycle test was accomplished with NASICON for the Zn-Ce RFB without large efficiency changes (Figure 5.1a).

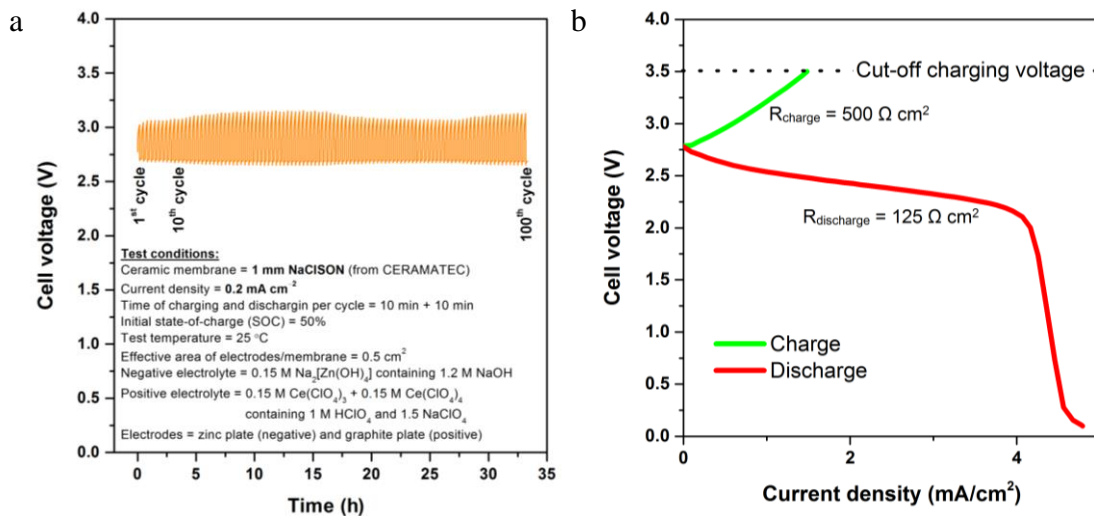


Figure 5.1 (a) Cycling test of NASICON-membrane-based Zn-Ce RFB. An initial SOC of 50% and a current density of 0.2 mA/cm^2 were used for both charging and discharging. Every cycle included the same time of 10 min for both charging and discharge operation. Energy efficiency of each cycle in the 100-cycle test is 90% on average. Coulombic efficiency was constant at 100%, due to the fixed time and current for both charging and discharging operation. Voltage efficiency is therefore equal to energy efficiency. (b) Polarization curve of Zn-Ce RFB during the initial state. Detailed experimental conditions are the same as those for (a).

Due to the large internal resistance, however, Zn-Ce RFB was only operated at 0.2 mA/cm^2 , much lower than the state-of-art operating current densities for RFB. In addition, an asymmetry in resistance was observed for both RFBs; the charge resistance is several times larger than discharge resistance, as shown in Figure 5.1b. Although preliminary data suggests good durability and acid/base blocking properties with a NaSICON membrane, numerous challenges are still awaiting ahead. Future work should focus on developing more advanced NaSICON separators with reduced resistances and symmetrical resistance behavior in acid-base hybrid RFBs.

REFERENCES

- [1] T. Ackermann, L. Soder. Wind energy technology and current status: a review. *Renewable & Sustainable Energy Reviews* **2000**, *4*, 315-374.
- [2] P. Nema, R. K. Nema, S. Rangnekar. A current and future state of art development of hybrid energy system using wind and PV-solar: A review. *Renewable & Sustainable Energy Reviews* **2009**, *13*, 2096-2103.
- [3] Solar energy perspectives: International Energy Agency; 2011.
- [4] The world wind energy association 2014 half-year report: American Wind Energy Association; 2014.
- [5] B. Dunn, H. Kamath, J. M. Tarascon. Electrical Energy Storage for the Grid: A Battery of Choices. *Science* **2011**, *334*, 928-935.
- [6] Z. G. Yang, J. L. Zhang, M. C. W. Kintner-Meyer, X. C. Lu, D. W. Choi, *et al.* Electrochemical Energy Storage for Green Grid. *Chemical Reviews* **2011**, *111*, 3577-3613.
- [7] M. Baumann, B. Zimmermann, H. Dura, B. Simon, M. Weil. A comparative probabilistic economic analysis of selected stationary battery systems for grid applications. *2013 4th International Conference on Clean Electrical Power (Iccpe): Renewable Energy Resources Impact* **2013**, 87-92.
- [8] H. Ibrahim, A. Ilinca, J. Perron. Energy storage systems - Characteristics and comparisons. *Renewable & Sustainable Energy Reviews* **2008**, *12*, 1221-1250.
- [9] D. Rastler. Electricity energy storage technology options: Electric Power Research Institute; 2010.
- [10] R. F. Service. Tanks for the Batteries. *Science* **2014**, *344*, 352-354.
- [11] C. P. de Leon, A. Frias-Ferrer, J. Gonzalez-Garcia, D. A. Szanto, F. C. Walsh. Redox flow cells for energy conversion. *Journal of Power Sources* **2006**, *160*, 716-732.

- [12] M. Skyllas-Kazacos, M. H. Chakrabarti, S. A. Hajimolana, F. S. Mjalli, M. Saleem. Progress in Flow Battery Research and Development. *Journal of the Electrochemical Society* **2011**, *158*, R55-R79.
- [13] P. Leung, X. H. Li, C. P. de Leon, L. Berlouis, C. T. J. Low, *et al.* Progress in redox flow batteries, remaining challenges and their applications in energy storage. *Rsc Advances* **2012**, *2*, 10125-10156.
- [14] W. Wang, Q. T. Luo, B. Li, X. L. Wei, L. Y. Li, *et al.* Recent Progress in Redox Flow Battery Research and Development. *Advanced Functional Materials* **2013**, *23*, 970-986.
- [15] A. Z. Weber, M. M. Mench, J. P. Meyers, P. N. Ross, J. T. Gostick, *et al.* Redox flow batteries: a review. *Journal of Applied Electrochemistry* **2011**, *41*, 1137-1164.
- [16] G. L. Soloveichik. Battery Technologies for Large-Scale Stationary Energy Storage. *Annual Review of Chemical and Biomolecular Engineering, Vol 2* **2011**, *2*, 503-527.
- [17] G. L. Soloveichik. Flow Batteries: Current Status and Trends. *Chemical Reviews* **2015**, *115*, 11533-11558.
- [18] L. H. Thaller. Electrically rechargeable redox flow cells. *The 9th Intersociety Energy Conversion Engineering Conference Proceedings* **1974**, 924-928.
- [19] M. Bartolozzi. Development of Redox Flow Batteries - a Historical Bibliography. *Journal of Power Sources* **1989**, *27*, 219-234.
- [20] M. Skyllas-Kazacos. Novel vanadium chloride/polyhalide redox flow battery. *Journal of Power Sources* **2003**, *124*, 299-302.
- [21] L. Q. Zhang, Q. Z. Lai, J. L. Zhang, H. M. Zhang. A High-Energy-Density Redox Flow Battery based on Zinc/Polyhalide Chemistry. *Chemsuschem* **2012**, *5*, 867-869.
- [22] H. S. Lim, A. M. Lackner, R. C. Knechtli. Zinc-Bromine Secondary Battery. *Journal of the Electrochemical Society* **1977**, *124*, 1154-1157.
- [23] R. J. Remick, P. G. P. Ang, inventors; Electrically rechargeable anionically active reduction-oxidation electrical storage-supply system. USA patent 4485154. 1984.

- [24] K. Hiroko, N. Takeshi, inventors; Redox Battery. Japan patent 57009072. 1982.
- [25] Y. H. Wen, H. M. Zhang, P. Qian, H. T. Zhou, P. Zhao, *et al.* Studies on iron (Fe³⁺/Fe²⁺)-complex/bromine (Br⁻²/Br⁻) redox flow cell in sodium acetate solution. *Journal of the Electrochemical Society* **2006**, *153*, A929-A934.
- [26] G. B. Adams, R. P. Hollandsworth, E. L. Littauer. *Proceedings of the 16th Intersociety Energy Conversion Engineering Conference* **1981**, 812-816.
- [27] C. H. Bae, E. P. L. Roberts, R. A. W. Dryfe. Chromium redox couples for application to redox flow batteries. *Electrochimica Acta* **2002**, *48*, 279-287.
- [28] T. P. Dirkse. The Nature of the Zinc-Containing Ion in Strongly Alkaline Solutions. *Journal of the Electrochemical Society* **1954**, *101*, 328-331.
- [29] R. L. Clarke, B. J. Dougherty, S. Harrison, J. P. Millington, S. Mohanta, inventors; Battery with bifunctional electrolyte. USA patent 6986966. 2006.
- [30] E. Wadsworth, F. R. Duke, C. A. Goetz. Present Status of Cerium(IV)-Cerium(III) Potentials. *Analytical Chemistry* **1957**, *29*, 1824-1825.
- [31] R. L. Clarke, B. Dougherty, S. Harrison, P. J. Millington, S. Mohanta, inventors; Cerium batteries. USA patent 7625663. 2004.
- [32] B. Fang, S. Iwasa, Y. Wei, T. Arai, M. Kumagai. Study of the Ce(III)/Ce(IV) redox couple for redox flow battery application. *Electrochimica Acta* **2002**, *47*, 3971-3976.
- [33] F. Q. Xue, Y. L. Wang, W. H. Wang, X. D. Wang. Investigation on the electrode process of the Mn(II)/Mn(III) couple in redox flow battery. *Electrochimica Acta* **2008**, *53*, 6636-6642.
- [34] T. Yamamura, N. Watanabe, T. Yano, Y. Shiokawa. Electron-transfer kinetics of Np³⁺/Np⁴⁺, NpO₂⁺/NpO₂²⁺, V²⁺/V³⁺, and VO₂⁺/VO₂⁺ at carbon electrodes. *Journal of the Electrochemical Society* **2005**, *152*, A830-A836.
- [35] M. Skyllas-Kazacos, M. Rychcik, R. G. Robins, A. G. Fane, M. A. Green. New All-Vanadium Redox Flow Cell. *Journal of the Electrochemical Society* **1986**, *133*, 1057-1058.
- [36] C. Tang, D. B. Zhou. Methanesulfonic acid solution as supporting electrolyte for zinc-vanadium redox battery. *Electrochimica Acta* **2012**, *65*, 179-184.

- [37] D. G. Oei. Chemically Regenerative Redox Fuel-Cells. *Journal of Applied Electrochemistry* **1982**, *12*, 41-51.
- [38] L. W. Hruska, R. F. Savinell. Investigation of Factors Affecting Performance of the Iron-Redox Battery. *Journal of the Electrochemical Society* **1981**, *128*, 18-25.
- [39] W. Wang, S. Kim, B. Chen, Z. Nie, J. Zhang, *et al.* A new redox flow battery using Fe/V redox couples in chloride supporting electrolyte. *Energy & Environmental Science* **2011**, *4*, 4068-4073.
- [40] J. Doria, M. C. D. Andres, C. Armenta. *NTERSOL 85: Proceedings of the Ninth Biennial Congress of the International Solar Energy Society* **1985**, 1500.
- [41] Y. Xu, Y. H. Wen, J. Cheng, G. P. Cao, Y. S. Yang. Study on a single flow acid Cd-chloranil battery. *Electrochemistry Communications* **2009**, *11*, 1422-1424.
- [42] R. F. Savinell, D. A. Polaski. *Proceedings of the 16th Intersociety Energy Conversion Engineering Conference* **1981**, *1*, 817.
- [43] E. Gileadi, S. Srinivasan, F. J. Salzano, C. Braun, A. Beaufriere, *et al.* An electrochemically regenerative hydrogen—chlorine energy storage system for electric utilities. *Journal of Power Sources* **1977**, *2*, 191-200.
- [44] Y. Masami, D. Akira, K. Zenji, inventors; Secondary Battery Device. Japan patent 60227364. 1985.
- [45] R. S. Yeo, D. T. Chin. Hydrogen-Bromine Cell for Energy-Storage Applications. *Journal of the Electrochemical Society* **1980**, *127*, 549-555.
- [46] C. Menictas, M. Skyllas-Kazacos. Performance of vanadium-oxygen redox fuel cell. *Journal of Applied Electrochemistry* **2011**, *41*, 1223-1232.
- [47] D. R. Lide. *CRC Handbook of Chemistry and Physics*, 87th edn. CRC Press: Bora Raton, FL, 2007.
- [48] V. E. Mironov, N. P. Lastovkina. Thermodynamics of trihalide ions. *Russian Journal of Physical Chemistry* **1967**, *41*, 991.
- [49] J. A. Dean. *Lange's Handbook of Chemistry*. McGraw, 1998.
- [50] J. L. Pierre, I. Gautier-Luneau. Iron and citric acid: A fuzzy chemistry of ubiquitous biological relevance. *Biometals* **2000**, *13*, 91-96.

- [51] L. H. Thaller, inventor Electrically rechargeable REDOX flow cell patent US3996064 A. 1975.
- [52] N. H. Hagedorn. NASA redox storage system development project final report: National Aeronautics and Space Administration, Lewis Research Center; 1984.
- [53] J. Giner, L. Swette, K. Cahill. Screening of redox couples and electrode materials: NASA - Lewis Research Center; 1976.
- [54] R. B. Hodgdon, W. A. Waite, S. S. Alexander. Anion permselective membrane: NASA - Lewis Research Center; 1984.
- [55] V. Jalan, H. Stark, J. Giner. Requirements for optimization of electrodes and electrolyte for the iron/chromium redox flow cell: NASA - Lewis Research Center; 1981.
- [56] R. F. Gahn, N. H. Hagedorn, J. S. Ling. Single cell performance studies on the Fe/Cr redox energy storage system using mixed reactant solutions at elevated temperature: NASA - Lewic Research Center; 1983.
- [57] C. Dyer. *Encyclopedia of Electrochemical Power Sources*, 1st Edition edn, vol. 3. Elsevier, 2009.
- [58] B. Li, Z. M. Nie, M. Vijayakumar, G. S. Li, J. Liu, *et al.* Ambipolar zinc-polyiodide electrolyte for a high-energy density aqueous redox flow battery. *Nature Communications* **2015**, *6*.
- [59] R. J. Remick, P. G. P. Ang, inventors; Electrically rechargeable anionically active reduction-oxidation electrical storage-supply system patent US4485154 A. 1984.
- [60] D. P. Scamman, G. W. Reade, E. P. L. Roberts. Numerical modelling of a bromide-polysulphide redox flow battery Part 1: Modelling approach and validation for a pilot-scale system. *Journal of Power Sources* **2009**, *189*, 1220-1230.
- [61] P. Zhao, H. M. Zhang, H. T. Zhou, B. L. Yi. Nickel foam and carbon felt applications for sodium poly sulfide/bromine redox flow battery electrodes. *Electrochimica Acta* **2005**, *51*, 1091-1098.
- [62] H. T. Zhou, H. M. Zhang, P. Zhao, B. L. Yi. A comparative study of carbon felt and activated carbon based electrodes for sodium polysulfide/bromine redox flow battery. *Electrochimica Acta* **2006**, *51*, 6304-6312.

- [63] H. T. Zhou, H. M. Zhang, P. Zhao, B. L. Yi. Novel cobalt coated carbon felt as high performance negative electrode in sodium polysulfide/bromine redox flow battery. *Electrochemistry* **2006**, *74*, 296-298.
- [64] C. Ding, H. M. Zhang, X. F. Li, T. Liu, F. Xing. Vanadium Flow Battery for Energy Storage: Prospects and Challenges. *Journal of Physical Chemistry Letters* **2013**, *4*, 1281-1294.
- [65] X. F. Li, H. M. Zhang, Z. S. Mai, H. Z. Zhang, I. Vankelecom. Ion exchange membranes for vanadium redox flow battery (VRB) applications. *Energy & Environmental Science* **2011**, *4*, 1147-1160.
- [66] M. Skyllas-Kazacos, M. Rychick, R. Robins, inventors; All-vanadium redox battery patent US4786567 A. 1984.
- [67] M. Rychcik, M. Skyllaskazacos. Characteristics of a New All-Vanadium Redox Flow Battery. *Journal of Power Sources* **1988**, *22*, 59-67.
- [68] B. Schwenzer, J. L. Zhang, S. Kim, L. Y. Li, J. Liu, *et al.* Membrane Development for Vanadium Redox Flow Batteries. *Chemsuschem* **2011**, *4*, 1388-1406.
- [69] J. Liu, J. G. Zhang, Z. G. Yang, J. P. Lemmon, C. Imhoff, *et al.* Materials Science and Materials Chemistry for Large Scale Electrochemical Energy Storage: From Transportation to Electrical Grid. *Advanced Functional Materials* **2013**, *23*, 929-946.
- [70] L. Y. Li, S. Kim, W. Wang, M. Vijayakumar, Z. M. Nie, *et al.* A Stable Vanadium Redox-Flow Battery with High Energy Density for Large-Scale Energy Storage. *Advanced Energy Materials* **2011**, *1*, 394-400.
- [71] M. Vijayakumar, W. Wang, Z. M. Nie, V. Sprenkle, J. Z. Hu. Elucidating the higher stability of vanadium(V) cations in mixed acid based redox flow battery electrolytes. *Journal of Power Sources* **2013**, *241*, 173-177.
- [72] D. S. Aaron, Q. Liu, Z. Tang, G. M. Grim, A. B. Papandrew, *et al.* Dramatic performance gains in vanadium redox flow batteries through modified cell architecture. *Journal of Power Sources* **2012**, *206*, 450-453.
- [73] Q. H. Liu, G. M. Grim, A. B. Papandrew, A. Turhan, T. A. Zawodzinski, *et al.* High Performance Vanadium Redox Flow Batteries with Optimized Electrode Configuration and Membrane Selection. *Journal of the Electrochemical Society* **2012**, *159*, A1246-A1252.

- [74] M. L. Perry, R. M. Darling, R. Zaffou. High Power Density Redox Flow Battery Cells. *Stationary and Large Scale Electrical Energy Storage 2* **2013**, 53, 7-16.
- [75] P. Singh. Application of Non-Aqueous Solvents to Batteries. *Journal of Power Sources* **1984**, 11, 135-142.
- [76] K. Gong, Q. Fang, S. Gu, S. F. Y. Li, Y. Yan. Nonaqueous redox-flow batteries: organic solvents, supporting electrolytes, and redox pairs. *Energy & Environmental Science* **2015**.
- [77] Y. Matsuda, K. Tanaka, M. Okada, Y. Takasu, M. Morita, *et al.* A Rechargeable Redox Battery Utilizing Ruthenium Complexes with Non-Aqueous Organic Electrolyte. *Journal of Applied Electrochemistry* **1988**, 18, 909-914.
- [78] M. H. Chakrabarti, R. A. W. Dryfe, E. P. L. Roberts. Evaluation of electrolytes for redox flow battery applications. *Electrochimica Acta* **2007**, 52, 2189-2195.
- [79] M. H. Chakrabarti, E. P. L. Roberts, M. Saleem. Charge-Discharge Performance of a Novel Undivided Redox Flow Battery for Renewable Energy Storage. *International Journal of Green Energy* **2010**, 7, 445-460.
- [80] M. H. Chakrabarti, E. P. L. Roberts, C. Bae, M. Saleem. Ruthenium based redox flow battery for solar energy storage. *Energy Conversion and Management* **2011**, 52, 2501-2508.
- [81] J. H. Kim, K. J. Kim, M. S. Park, N. J. Lee, U. Hwang, *et al.* Development of metal-based electrodes for non-aqueous redox flow batteries. *Electrochemistry Communications* **2011**, 13, 997-1000.
- [82] J. Mun, M. J. Lee, J. W. Park, D. J. Oh, D. Y. Lee, *et al.* Non-Aqueous Redox Flow Batteries with Nickel and Iron Tris(2,2'-bipyridine) Complex Electrolyte. *Electrochemical and Solid State Letters* **2012**, 15, A80-A82.
- [83] T. Yamamura, Y. Shiokawa, H. Yamana, H. Moriyama. Electrochemical investigation of uranium beta-diketonates for all-uranium redox flow battery. *Electrochimica Acta* **2002**, 48, 43-50.
- [84] T. Yamamura, K. Shirasaki, Y. Shiokawa, Y. Nakamura, S. Y. Kim. Characterization of tetraketone ligands for active materials of all-uranium redox flow battery. *Journal of Alloys and Compounds* **2004**, 374, 349-353.

- [85] Q. Sun, Q. Wang, Y. Shiokawa, Y. Kawazoe. Interactions of uranium atom with tetraketone complexes. *Chemical Physics Letters* **2005**, *415*, 243-245.
- [86] K. Shirasaki, T. Yamamura, T. Herai, Y. Shiokawa. Electrodeposition of uranium in dimethyl sulfoxide and its inhibition by acetylacetonate as studied by EQCM. *Journal of Alloys and Compounds* **2006**, *418*, 217-221.
- [87] T. Yamamura, K. Shirasaki, D. X. Li, Y. Shiokawa. Electrochemical and spectroscopic investigations of uranium(III) with N,N,N',N'-tetramethylmalonamide in DMF. *Journal of Alloys and Compounds* **2006**, *418*, 139-144.
- [88] K. Shirasaki, T. Yamamura, Y. Shiokawa. Electrolytic preparation, redox titration and stability of pentavalent state of uranyl tetracetate in dimethyl sulfoxide. *Journal of Alloys and Compounds* **2006**, *408*, 1296-1301.
- [89] T. Yamamura, K. Shirasaki, H. Sato, Y. Nakamura, H. Tomiyasu, *et al.* Enhancements in the electron-transfer kinetics of uranium-based redox couples induced by tetraketone ligands with potential chelate effect. *Journal of Physical Chemistry C* **2007**, *111*, 18812-18820.
- [90] Q. H. Liu, A. E. S. Sleightholme, A. A. Shinkle, Y. D. Li, L. T. Thompson. Non-aqueous vanadium acetylacetonate electrolyte for redox flow batteries. *Electrochemistry Communications* **2009**, *11*, 2312-2315.
- [91] A. A. Shinkle, A. E. S. Sleightholme, L. T. Thompson, C. W. Monroe. Electrode kinetics in non-aqueous vanadium acetylacetonate redox flow batteries. *Journal of Applied Electrochemistry* **2011**, *41*, 1191-1199.
- [92] T. Herr, J. Noack, P. Fischer, J. Tubke. 1,3-Dioxolane, tetrahydrofuran, acetylacetonate and dimethyl sulfoxide as solvents for non-aqueous vanadium acetylacetonate redox-flow-batteries. *Electrochimica Acta* **2013**, *113*, 127-133.
- [93] D. P. Zhang, Q. H. Liu, X. S. Shi, Y. D. Li. Tetrabutylammonium hexafluorophosphate and 1-ethyl-3-methyl imidazolium hexafluorophosphate ionic liquids as supporting electrolytes for non-aqueous vanadium redox flow batteries. *Journal of Power Sources* **2012**, *203*, 201-205.
- [94] P. J. Cappillino, H. D. Pratt, N. S. Hudak, N. C. Tomson, T. M. Anderson, *et al.* Application of Redox Non-Innocent Ligands to Non-Aqueous Flow Battery Electrolytes. *Advanced Energy Materials* **2014**, *4*.

- [95] A. A. Shinkle, T. J. Pomaville, A. E. S. Sleightholme, L. T. Thompson, C. W. Monroe. Solvents and supporting electrolytes for vanadium acetylacetonate flow batteries. *Journal of Power Sources* **2014**, *248*, 1299-1305.
- [96] Q. H. Liu, A. A. Shinkle, Y. D. Li, C. W. Monroe, L. T. Thompson, *et al.* Non-aqueous chromium acetylacetonate electrolyte for redox flow batteries. *Electrochemistry Communications* **2010**, *12*, 1634-1637.
- [97] A. E. S. Sleightholme, A. A. Shinkle, Q. H. Liu, Y. D. Li, C. W. Monroe, *et al.* Non-aqueous manganese acetylacetonate electrolyte for redox flow batteries. *Journal of Power Sources* **2011**, *196*, 5742-5745.
- [98] D. P. Zhang, H. J. Lan, Y. D. Li. The application of a non-aqueous bis(acetylacetonate)ethylenediamine cobalt electrolyte in redox flow battery. *Journal of Power Sources* **2012**, *217*, 199-203.
- [99] N. G. Connelly, W. E. Geiger. Chemical redox agents for organometallic chemistry. *Chemical Reviews* **1996**, *96*, 877-910.
- [100] D. H. Evans. Solution Electron-Transfer Reactions in Organic and Organometallic Electrochemistry. *Chemical Reviews* **1990**, *90*, 739-751.
- [101] D. H. Evans. One-electron and two-electron transfers in electrochemistry and homogeneous solution reactions. *Chemical Reviews* **2008**, *108*, 2113-2144.
- [102] H. D. Pratt, N. S. Hudak, X. K. Fang, T. M. Anderson. A polyoxometalate flow battery. *Journal of Power Sources* **2013**, *236*, 259-264.
- [103] M. H. Chakrabarti, R. A. W. Dryfe, E. P. L. Roberts. Organic electrolytes for redox flow batteries. *Journal of the Chemical Society of Pakistan* **2007**, *29*, 294-300.
- [104] A. R. Forrester, R. H. Thomson. Stable Nitroxide Radicals. *Nature* **1964**, *203*, 74-&.
- [105] Z. Li, S. Li, S. Q. Liu, K. L. Huang, D. Fang, *et al.* Electrochemical Properties of an All-Organic Redox Flow Battery Using 2,2,6,6-Tetramethyl-1-Piperidinyloxy and N-Methylphthalimide. *Electrochemical and Solid State Letters* **2011**, *14*, A171-A173.
- [106] W. Wang, W. Xu, L. Cosimbescu, D. W. Choi, L. Y. Li, *et al.* Anthraquinone with tailored structure for a nonaqueous metal-organic redox flow battery. *Chemical Communications* **2012**, *48*, 6669-6671.

- [107] F. R. Brushett, J. T. Vaughey, A. N. Jansen. An All-Organic Non-aqueous Lithium-Ion Redox Flow Battery. *Advanced Energy Materials* **2012**, 2, 1390-1396.
- [108] Z. P. Song, H. Zhan, Y. H. Zhou. Anthraquinone based polymer as high performance cathode material for rechargeable lithium batteries. *Chemical Communications* **2009**, 448-450.
- [109] L. Zhang, Z. C. Zhang, P. C. Redfern, L. A. Curtiss, K. Amine. Molecular engineering towards safer lithium-ion batteries: a highly stable and compatible redox shuttle for overcharge protection. *Energy & Environmental Science* **2012**, 5, 8204-8207.
- [110] M. Morita, Y. Tanaka, K. Tanaka, Y. Matsuda, T. Matsumurainoue. Electrochemical Oxidation of Ruthenium and Iron Complexes at Rotating-Disk Electrode in Acetonitrile Solution. *Bulletin of the Chemical Society of Japan* **1988**, 61, 2711-2714.
- [111] T. Saji, T. Yamada, S. Aoyagui. Electron-Transfer Kinetics of Transition-Metal Complexes in Lower Oxidation-States .3. Electrochemical Rate Constants for Fe(II)-Fe(I) Redox Systems. *Bulletin of the Chemical Society of Japan* **1975**, 48, 1641-1642.
- [112] T. Suga, Y. J. Pu, K. Oyaizu, H. Nishide. Electron-transfer kinetics of nitroxide radicals as an electrode-active material. *Bulletin of the Chemical Society of Japan* **2004**, 77, 2203-2204.
- [113] K. Oyaizu, A. Hatemata, W. Choi, H. Nishide. Redox-active polyimide/carbon nanocomposite electrodes for reversible charge storage at negative potentials: expanding the functional horizon of polyimides. *Journal of Materials Chemistry* **2010**, 20, 5404-5410.
- [114] R. M. Darling, K. G. Gallagher, J. A. Kowalski, S. Ha, F. R. Brushett. Pathways to low-cost electrochemical energy storage: a comparison of aqueous and nonaqueous flow batteries. *Energy & Environmental Science* **2014**, 7, 3459-3477.
- [115] R. Ferrigno, A. D. Stroock, T. D. Clark, M. Mayer, G. M. Whitesides. Membraneless vanadium redox fuel cell using laminar flow. *Journal of the American Chemical Society* **2002**, 124, 12930-12931.
- [116] K. S. Salloum, J. D. Posner. A membraneless microfluidic fuel cell stack. *Journal of Power Sources* **2011**, 196, 1229-1234.

- [117] W. A. Braff, M. Z. Bazant, C. R. Buie. Membrane-less hydrogen bromine flow battery. *Nature Communications* **2013**, *4*.
- [118] W. A. Braff, C. R. Buie, M. Z. Bazant. Boundary Layer Analysis of Membraneless Electrochemical Cells. *Journal of the Electrochemical Society* **2013**, *160*, A2056-A2063.
- [119] W. A. Braff, C. R. Buie, M. Z. Bazant. Numerical and Analytical Modeling of a Membraneless Hydrogen Bromine Laminar Flow Battery. *Stationary and Large Scale Electrical Energy Storage 2* **2013**, *53*, 51-62.
- [120] B. Huskinson, M. P. Marshak, C. Suh, S. Er, M. R. Gerhardt, *et al.* A metal-free organic-inorganic aqueous flow battery. *Nature* **2014**, *505*, 195-+.
- [121] B. Yang, L. Hooper-Burkhardt, F. Wang, G. K. S. Prakash, S. R. Narayanan. An Inexpensive Aqueous Flow Battery for Large-Scale Electrical Energy Storage Based on Water-Soluble Organic Redox Couples. *Journal of the Electrochemical Society* **2014**, *161*, A1371-A1380.
- [122] K. X. Lin, Q. Chen, M. R. Gerhardt, L. C. Tong, S. B. Kim, *et al.* Alkaline quinone flow battery. *Science* **2015**, *349*, 1529-1532.
- [123] C. H. Bae, E. P. L. Roberts, M. H. Chakrabarti, M. Saleem. All-Chromium Redox Flow Battery for Renewable Energy Storage. *International Journal of Green Energy* **2011**, *8*, 248-264.
- [124] H. Vafiadis, M. Skyllas-Kazacos. Evaluation of membranes for the novel vanadium bromine redox flow cell. *Journal of Membrane Science* **2006**, *279*, 394-402.
- [125] G. M. Weng, C. Y. V. Li, K. Y. Chan. Study of the Electrochemical Behaviour of High Voltage Vanadium-Metal Hydride Semi-Flow Battery. *ECS Transactions* **2013**, *53*, 39-50.
- [126] G. M. Weng, C. Y. V. Li, K. Y. Chan. High Voltage Vanadium-Metal Hydride Rechargeable Semi-Flow Battery. *Journal of the Electrochemical Society* **2013**, *160*, A1384-A1389.
- [127] H. Strathmann, J. J. Krol, H. J. Rapp, G. Eigenberger. Limiting current density and water dissociation in bipolar membranes. *Journal of Membrane Science* **1997**, *125*, 123-142.

- [128] J. J. Krol, M. Jansink, M. Wessling, H. Strathmann. Behaviour of bipolar membranes at high current density Water diffusion limitation. *Separation and Purification Technology* **1998**, *14*, 41-52.
- [129] T. Aritomi, T. vandenBoomgaard, H. Strathmann. Current-voltage curve of a bipolar membrane at high current density. *Desalination* **1996**, *104*, 13-18.
- [130] H. Q. Li, G. M. Weng, C. Y. V. Li, K. Y. Chan. Three electrolyte high voltage acid-alkaline hybrid rechargeable battery. *Electrochimica Acta* **2011**, *56*, 9420-9425.
- [131] K. Y. Chan, S. A. Cheng, inventors; High Voltage Dual Electrolyte Electrochemical Power Cells. USA patent 7,344,801. 2008.
- [132] K. Y. Chan, S. A. Cheng. High Voltage Dual Electrolyte Electrochemical Power Sources. *ECS Transactions* **2010**, *25*, 213-219.
- [133] P. Murray. *Electrodialysis and Electrodialysis Reversal*. American Water Works Assn, 1995.
- [134] G. M. Weng, C. Y. V. Li, K. Y. Chan. Lead Acid-NiMH Hybrid Battery System Using Gel Electrolyte. *ECS Transactions* **2012**, *41*, 133-143.
- [135] S. Gu, K. Gong, E. Z. Yan, Y. S. Yan. A multiple ion-exchange membrane design for redox flow batteries. *Energy & Environmental Science* **2014**, *7*, 2986-2998.
- [136] S. Licht. An Energetic Medium for Electrochemical Storage Utilizing the High Aqueous Solubility of Potassium Polysulfide. *Journal of the Electrochemical Society* **1987**, *134*, 2137-2141.
- [137] M. C. Tucker, V. Srinivasan, P. N. Ross, A. Z. Weber. Performance and cycling of the iron-ion/hydrogen redox flow cell with various catholyte salts. *Journal of Applied Electrochemistry* **2013**, *43*, 637-644.
- [138] J. Y. Xi, Z. H. Wu, X. P. Qiu, L. Q. Chen. Nafion/SiO₂ hybrid membrane for vanadium redox flow battery. *Journal of Power Sources* **2007**, *166*, 531-536.
- [139] Q. T. Luo, L. Y. Li, W. Wang, Z. M. Nie, X. L. Wei, *et al.* Capacity Decay and Remediation of Nafion-based All-Vanadium Redox Flow Batteries. *Chemsuschem* **2013**, *6*, 268-274.

- [140] B. Li, Q. T. Luo, X. L. Wei, Z. M. Nie, E. Thomsen, *et al.* Capacity Decay Mechanism of Microporous Separator-Based All-Vanadium Redox Flow Batteries and its Recovery. *Chemsuschem* **2014**, 7, 577-584.
- [141] J. Cheng, L. Zhang, Y. S. Yang, Y. H. Wen, G. P. Cao, *et al.* Preliminary study of single flow zinc-nickel battery. *Electrochemistry Communications* **2007**, 9, 2639-2642.
- [142] L. H. Thaller. Electrically rechargeable redox flow cells. *9th Intersociety Energy Conversion Engineering Conference Proceedings* **1974**, 924-928.
- [143] L. Zhang, J. Cheng, Y. S. Yang, Y. H. Wen, X. D. Wang, *et al.* Study of zinc electrodes for single flow zinc/nickel battery application. *Journal of Power Sources* **2008**, 179, 381-387.
- [144] M. C. Tucker, K. T. Cho, A. Z. Weber. Optimization of the iron-ion/hydrogen redox flow cell with iron chloride catholyte salt. *Journal of Power Sources* **2014**, 245, 691-697.
- [145] K. Gong, X. Ma, K. M. Conforti, K. J. Kuttler, J. B. Grunewald, *et al.* A zinc-iron redox-flow battery under \$100 per kW h of system capital cost. *Energy & Environmental Science* **2015**, 8, 2941-2945.
- [146] R. Holze. *Landolt-Börnstein: Numerical Data and Functional Relationships in Science and Technology, Electrochemical Thermodynamics and Kinetics*, vol. Subvolume A. Springer.
- [147] A. Shah, R. Tangirala, R. Singh, R. Wills, F. Walsh. A dynamic unit cell model for the all-vanadium flow battery. *Journal of the Electrochemical Society* **2011**, 158, A671-A677.
- [148] D. Stephenson, S. Kim, F. Chen, E. Thomsen, V. Viswanathan, *et al.* Electrochemical Model of the Fe/V Redox Flow Battery. *Journal of the Electrochemical Society* **2012**, 159, A1993-A2000.
- [149] V. Viswanathan, A. Crawford, D. Stephenson, S. Kim, W. Wang, *et al.* Cost and performance model for redox flow batteries. *Journal of Power Sources* **2014**, 247, 1040-1051.
- [150] R. D. Patel, K.-C. Lang, I. F. Miller. Polarization in Ion-Exchange Membrane Electrodialysis. *Industrial & Engineering Chemistry Fundamentals* **1977**, 16, 340-348.

- [151] Y. Tanaka. Concentration polarization in ion-exchange membrane electro dialysis—the events arising in a flowing solution in a desalting cell. *Journal of Membrane Science* **2003**, 216, 149-164.
- [152] L. Zhang, H. Zhang, Q. Lai, X. Li, Y. Cheng. Development of carbon coated membrane for zinc/bromine flow battery with high power density. *Journal of Power Sources* **2013**, 227, 41-47.
- [153] B. Huskinson, M. P. Marshak, C. Suh, S. Er, M. R. Gerhardt, *et al.* A metal-free organic-inorganic aqueous flow battery. *Nature* **2014**, 505, 195-198.
- [154] K. T. Cho, P. Albertus, V. Battaglia, A. Kojic, V. Srinivasan, *et al.* Optimization and Analysis of High-Power Hydrogen/Bromine-Flow Batteries for Grid-Scale Energy Storage. *Energy Technology* **2013**, 1, 596-608.
- [155] Y. H. Wen, H. M. Zhang, P. Qian, H. T. Zhou, P. Zhao, *et al.* A study of the Fe(III)/Fe(II)-triethanolamine complex redox couple for redox flow battery application. *Electrochimica Acta* **2006**, 51, 3769-3775.
- [156] L. Sanz, D. Lloyd, E. Magdalena, J. Palma, K. Kontturi. Description and performance of a novel aqueous all-copper redox flow battery. *Journal of Power Sources* **2014**, 268, 121-128.
- [157] P. Peljo, D. Lloyd, D. Nguyet, M. Majaneva, K. Kontturi. Towards a thermally regenerative all-copper redox flow battery. *Physical Chemistry Chemical Physics* **2014**, 16, 2831-2835.
- [158] N. Arroyo-Curras, J. W. Hall, J. E. Dick, R. A. Jones, A. J. Bard. An Alkaline Flow Battery Based on the Coordination Chemistry of Iron and Cobalt. *Journal of the Electrochemical Society* **2015**, 162, A378-A383.
- [159] Y. W. D. Chen, K. S. V. Santhanam, A. J. Bard. Solution Redox Couples for Electrochemical Energy-Storage .1. Iron-(Iii)-Iron-(Ii) Complexes with O-Phenanthroline and Related Ligands. *Journal of the Electrochemical Society* **1981**, 128, 1460-1467.
- [160] A. S. N. Murthy, T. Srivastava. Fe(Iii)/Fe(Ii) Ligand Systems for Use as Negative Half-Cells in Redox-Flow Cells. *Journal of Power Sources* **1989**, 27, 119-126.
- [161] Rechargeable alkaline zinc/ferro-ferricyanide hybrid redox battery. *Journal of Power Sources* **1980**, 5, 384-385.

- [162] K. L. Hawthorne, J. S. Wainright, R. F. Savinell. Studies of Iron-Ligand Complexes for an All-Iron Flow Battery Application. *Journal of the Electrochemical Society* **2014**, *161*, A1662-A1671.
- [163] R. Holze. *Numerical Data and Functional Relationships in Science and Technology-Electrochemistry-Electrochemical Thermodynamics and Kinetics*, vol. 9. Springer, 2007.
- [164] F. Hilbert, Y. Miyoshi, G. Eichkorn, W. J. Lorenz. Correlations between the Kinetics of Electrolytic Dissolution and Deposition of Iron: I . The Anodic Dissolution of Iron. *Journal of the Electrochemical Society* **1971**, *118*, 1919-1926.
- [165] I. M. Kolthoff, W. J. Tomsicek. The Oxidation Potential of the System Potassium Ferrocyanide–Potassium Ferricyanide at Various Ionic Strengths. *The Journal of Physical Chemistry* **1934**, *39*, 945-954.
- [166] L. R. F. Allen J. Bard. *Electrochemical Methods: Fundamentals and Applications*. Wiley, 2000.
- [167] L. C. Chang, T. Lin, M. H. Li. Mutual diffusion coefficients of some aqueous alkanolamines solutions. *Journal of Chemical and Engineering Data* **2005**, *50*, 77-84.
- [168] T. Yamaguchi, L. M. Boetje, C. A. Koval, R. D. Noble, C. N. Bowman. Transport-Properties of Carbon-Dioxide through Amine Functionalized Carrier Membranes. *Industrial & Engineering Chemistry Research* **1995**, *34*, 4071-4077.
- [169] T. Yamaguchi, C. A. Koval, R. D. Noble, C. N. Bowman. Transport mechanism of carbon dioxide through perfluorosulfonate ionomer membranes containing an amine carrier. *Chemical Engineering Science* **1996**, *51*, 4781-4789.
- [170] W. R. May. Solubility of ferrocene in organic solvents: SFA International, Inc.; 2009.
- [171] Technical information of Aliquat 336: BASF; 2013.
- [172] R. R. Gagne, C. A. Koval, G. C. Lisensky. Ferrocene as an Internal Standard for Electrochemical Measurements. *Inorganic Chemistry* **1980**, *19*, 2854-2855.

- [173] M. Gattrell, J. Park, B. MacDougall, J. Apte, S. McCarthy, *et al.* Study of the mechanism of the vanadium 4+/5+ redox reaction in acidic solutions. *Journal of the Electrochemical Society* **2004**, *151*, A123-A130.
- [174] R. S. Nicholson. Theory and Application of Cyclic Voltammetry for Measurement of Electrode Reaction Kinetics. *Analytical Chemistry* **1965**, *37*, 1351-1355.
- [175] Vanadium redox flow batteries, an in-depth analysis: Electric power research institute; 2007.

Appendix A

CALCULATION METHODS

A.1 Theoretical calculation of R_{cp}

Assuming electrolyte electroneutrality stands, R_{cp} can be calculated by the following equation:

$$R_{cp} = (\Delta\Psi_N + \Delta\Psi_D)/I \quad \text{Eq. 1}$$

where, $\Delta\Psi_N$ is the sum of all potential differences established through each Nernst boundary layer in the electrolyte adjacent to an ion-exchange membrane; and $\Delta\Psi_D$ is the sum of all Donnan potential differences built across each ion-exchange membrane between two different electrolytes; and I is current density.

Specifically, there are four Nernst boundary layers in the double-membrane cell: 1) in negative electrolyte adjacent to the CEM ($\Delta\psi_{n-c}$), 2) in middle electrolyte adjacent to the CEM ($\Delta\psi_{m-c}$), 3) in middle electrolyte adjacent to the AEM ($\Delta\psi_{m-a}$), and 4) in positive electrolyte adjacent to the AEM ($\Delta\psi_{p-a}$). As such, $\Delta\Psi_N = \Delta\psi_{n-c} + \Delta\psi_{m-c} + \Delta\psi_{p-a} + \Delta\psi_{m-a}$.

There are two Donnan potential differences built in the double-membrane cell: 1) across CEM between negative electrolyte and middle electrolyte ($\Delta\psi_{CEM}$); and 2) across AEM between middle electrolyte and positive electrolyte ($\Delta\psi_{AEM}$). Then, $\Delta\Psi_D = \Delta\psi_{CEM} + \Delta\psi_{AEM}$.

The detailed calculation of each component is described in the following part. The calculation was performed in MATLAB and the corresponding code is attached.

(1) Calculation of the potential difference through Nernst boundary layer

Eq. 2 below shows the dependence of the voltage loss across the middle electrolyte channel on the concentration polarization at each membrane (first term on right hand side) and the resistivity of the middle channel electrolyte (ρ_x). The concentration polarization term is adapted from a boundary layer analysis performed by Braff et. al.^[117, 118]. The fluid flow is in the positive y-direction with current passing perpendicular to fluid flow.

$$\Delta\psi_{middle} = -2 \frac{RT}{z_e F} \ln \left(1 - \frac{i(\tilde{y})}{i_{lim}(\tilde{y})} \right) + \rho_x d \cdot j(\tilde{y}) \quad \text{Eq. 2}$$

where $\Delta\psi_{middle}$ stands for voltage loss across the middle electrolyte channel; $\tilde{y} = y/w$, w is the height of middle electrolyte; ρ_x is the resistivity of the middle channel electrolyte; d is the thickness of the middle electrolyte; R is the ideal gas constant; T is temperature; z_e is the charge of the ionic species; F is Faraday's constant; i is current density; i_{lim} is limiting current density given for Poiseuille flow in the middle electrolyte.

$$i_{lim}(\tilde{y}) = \sqrt[3]{\left(\frac{18Pe}{\tilde{y}\beta} \right) \frac{C_{NaCl} z_e D_{NaCl} F}{d \cdot \Gamma(1/3)}} \quad \text{Eq. 3}$$

where D_{NaCl} is the effective diffusion coefficient of sodium chloride:

$$D_{NaCl} = \frac{2D_{Na^+} D_{Cl^-}}{D_{Na^+} + D_{Cl^-}}; \beta = w/d; w \text{ and } d \text{ are the width and thickness of}$$

middle electrolyte, respectively; $Pe = v \cdot w / D_{NaCl}$; v is the mean velocity of the parabolic velocity profile; C_{NaCl} is the bulk NaCl concentration;

Eq. 2 was solved along \tilde{y} in MATLAB by discretizing in the y direction. The mesh was refined until the solution was insensitive to the mesh size ($n=100$). $i(\tilde{y})$ was first solved such that the total potential drop was constant for all \tilde{y} and the total current matched experiments. Next, the concentration polarization term through Nernst boundary layer was tabulated (at each y position) to find its contribution to the total potential drop at various middle channel conditions, based on Eq. 4.

$$\Delta\psi_N(\tilde{y}) = -2 \frac{RT}{z_e F} \ln \left(1 - \frac{i(\tilde{y})}{i_{\text{lim}}(\tilde{y})} \right) \quad \text{Eq. 4}$$

The concentration polarization term through the Nernst boundary layer was then integrated along \tilde{y} to obtain $\Delta\psi_N$. The variable ASR_{cpN} was used to stand for this Nernst potential difference in terms of area-specific resistance in Matlab code.

(2) Calculation of the Donnan potential differences across ion-exchange membrane

The Donnan potential difference across an ion-exchange membrane from electrolyte α to electrolyte β is described as follow:

$$\Delta\psi_D = -\frac{RT}{z_e F} \ln \left(\frac{C_0^\beta + \Delta C^\beta}{C_0^\alpha - \Delta C^\alpha} \right) - \frac{RT}{z_e F} \ln \left(\frac{C_0^\beta}{C_0^\alpha} \right) \quad \text{Eq. 5}$$

where $\Delta\psi_D$ stands for each of $\Delta\psi_{\text{CEM}}$ and $\Delta\psi_{\text{AEM}}$; R is ideal gas constant; T is temperature; z_e is the charge of ionic species; F is faraday constant; C^α and C^β are the concentration of selecting ion in the vicinity of ion-exchange membrane in electrolyte α and β , respectively; C_0^α and C_0^β are concentration at open circuit state in

electrolyte α and β , respectively; ΔC^β and ΔC^α are the concentration change in Nernst boundary layer in electrolyte α and β , respectively.

The second term in the equation is to offset static Donnan potential which does not contribute to the concentration-overpotential here.

The concentration change in Nernst boundary layer can be calculated by

$$\Delta C = \frac{i}{\bar{i}_{lim}} C_0 \quad \text{Eq. 6}$$

Where i is the current density, \bar{i}_{lim} is averaged limiting current density, C_0 is the concentration at open circuit state.

Each Donnan potential difference across ion-exchange membrane can be calculated and the variable `ASRcpD` was used to stand for this Donnan potential difference in terms of area-specific resistance in Matlab code.

A.2 Development of cost model.

The RFB cost model is designed for a large scale RFB system (1 MW and 8 WMh). The costs of materials used for calculating costs of redox pairs, and electrolytes, and stacks are listed in supplementary tables. The algorithm to calculate V_{eff} , C_e and C_p is shown as a flow chart in Figure A1.^[147, 148] The modeling GUI was written in software Qt/C++. The application was compiled with MinGW 4.9.1 for the Windows build and Clang 3.6 for the Mac build; Qt 5.4 libraries were used for both.

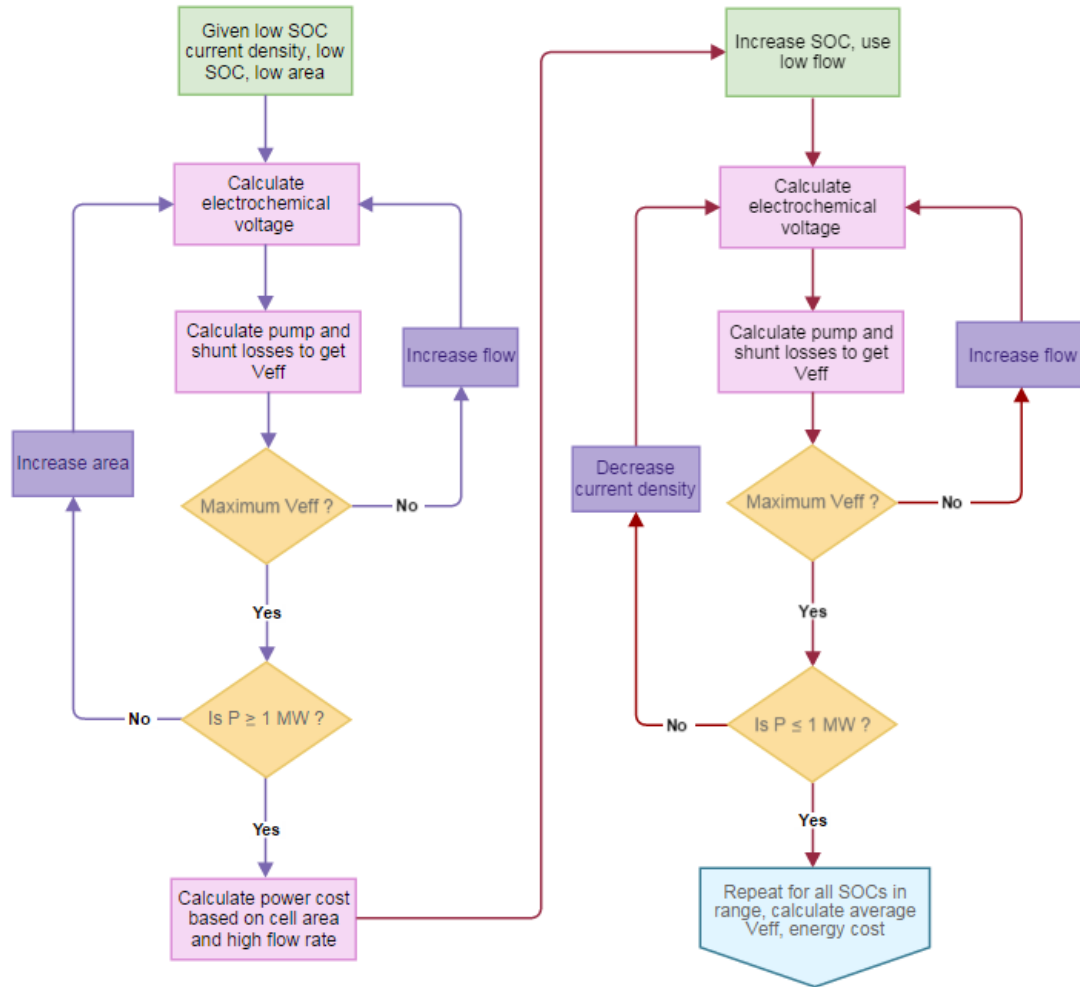


Figure A1 Flow chart of simulation model algorithm. Reprinted from *J Power Sources* **247**, 1040-1051, with permission from Elsevier.

(1) Calculation of the unit electrolyte cost (U_e).

The following equation was used to calculate the electrolyte cost, and the results are listed in **Table B1**.

$$U_e = U_r + U_{se} = (u_{r,n} + u_{r,p}) + (u_{se,n} + u_{se,p} + u_{se,m})$$

Where U_e is the electrolyte cost; U_r is the cost of redox pair; U_{se} is the cost of supporting electrolyte (salt/acid/base); $u_{r,n}$ and $u_{r,p}$ are the cost of negative redox pair and the cost of positive redox pair, respectively; $u_{se,n}$, $u_{se,p}$, and $u_{se,m}$ are the cost of negative supporting base, the cost of positive supporting acid, and the cost of middle supporting salt.

For each electrolyte (negative, positive, and middle), u_r and u_{se} are calculated by the following two equations correspondingly.

$$u_r = P/(n \cdot F \cdot W); \text{ and } u_{se} = P/(n \cdot F \cdot W \cdot \gamma)$$

where P is the chemical price, W is the molecular weight of chemical, and n is the number of working electrons/charges per molecule, F is Faraday's constant, γ is the ratio of the concentration of redox pair to the concentration of corresponding supporting salt/acid/base.

(2) Calculation of the unit stack cost (U_s).

The stack cost was calculated by the following equation, and the results are listed in **Table B2**.

$$U_s = U_{em} + U_m + U_b$$

where U_s is the stack cost, U_{em} is the cost of electrode materials, U_m is the membrane cost, and U_b is the cost of bipolar plate.

Appendix B

SUPPLEMENTARY TABLES

Table B1 Results of electrolyte cost for both Zn-Fe RFB and all-V RFB

RFB	U_r (\$/Ah) ^[a]	U_{ss} (\$/Ah) ^[b]	U_e (\$/Ah)
Zn-Fe RFB	0.33	0.40	0.73
All-VRFB	3.99	0.05	4.05

[a] The pricing information and detailed calculation is shown in **Table B3**

[b] The pricing information and detailed calculation is shown in **Table B4**

Table B2 Results of stack cost for both Zn-Fe RFB and all-V RFB

RFB	U_{em} (\$/m ²) ^[a]	U_m (\$/m ²) ^[a]	U_b (\$/m ²) ^[b]	U_s (\$/m ²)
Zn-Fe RFB	118	345	55	518
All-V RFB	140	500	55	695

[a] Detailed calculation is shown in **Table B5 and Table B6**.

[b] From reference¹.

Table B3 Prices of redox compounds

Compound	Molecular weight (W) (g/mol)	Price (P) (\$/kg)	n	u_r (ϕ /Ah)
----------	-------------------------------------	--------------------------	-----	------------------------

FeCl ₃	162.5	0.215 ^a	1	0.13
ZnO	81.0	1.3 ^b	2	0.20
V ₂ O ₅	182.0	13.2 ^c	2	3.99

[a] Quoted from [Henan Allrich Chemical Co., Ltd.](#)
[b] Quoted from [Henan Premtec Enterprise Co.](#)
[c] From reference^[149]

Table B4 Prices of supporting salt/acid/base

Chemical	Molecular weight (W) (g/mol)	Price (P) (\$/kg)	n	γ	u_{ss} (ϕ /Ah)
HCl (33%)	36.5	0.18 ^a	1	1	0.074
NaOH	40	0.4 ^b	2	0.1	0.30
NaCl	58.5	0.05 ^c	1	0.33	0.03
H ₂ SO ₄	98	0.075 ^d	2	0.3	0.05

[a] Quoted from [A.I.K International Exports](#)
[b] Quoted from [Henan Fengbai Commercial Co., Ltd.](#)
[c] Quoted from [Weifang Dabang Chemical Industry Co., Ltd.](#)
[d] From the reference^[149]

Table B5 Prices of electrode materials

Electrode materials	Price
Carbon felt, 3.1mm thickness (\$ m ⁻²)	70 ^a
Copper mesh, 0.5 mm thickness and 30×30 grid per square inch (\$ m ⁻²)	48 ^b

[a] From reference ^[149]
[b] Quoted from [TWP, Inc.](#)

Table B6 Prices of membrane materials

Membranes	Price
Nafion 212 cation-exchange membrane ($\$ \text{ m}^{-2}$)	225 ^a
Nafion 117 cation-exchange membrane ($\$ \text{ m}^{-2}$)	500 ^b
FAA3 anion-exchange membrane, 50 μm thickness ($\$ \text{ m}^{-2}$)	120 ^c
[a] From reference ^[175]	
[b] From reference ^[149]	
[c] Quoted from Fuma-Tech, GmbH .	

Table B7 Prices of other materials/handling

Materials and handling	Price ^a
Heat Exchanger ($\$ \text{ kW}^{-1}$)	84
Valves ($\$$ per unit)	150
Pipes ($\$ \text{ m}^{-1}$)	8
Bolts ($\$$ per unit)	15
Gaskets ($\$$ per unit)	2.5
Collector plates ($\$$ per unit)	150
Aluminum end plates ($\$$ per unit)	193
6" PVC ball valve ($\$$ per unit)	285
1" PVC ball valve ($\$$ per unit)	8.6
PVC pipe 1" ($\$ \text{ ft}^{-1}$)	0.87
PVC pipe 6" ($\$ \text{ ft}^{-1}$)	12.49
PVC frame ($\$ \text{ m}^{-2}$)	16.56
Power conditioning system ($\$ \text{ kW}^{-1}$)	210
Labor for electrolyte preparation ($\$ \text{ kWh}^{-1}$)	1
Tank ($\$ \text{ gal}^{-1}$)	0.41
Tank freight ($\$ \text{ gal}^{-1}\text{mile}^{-1}$)	0.00011
[a] All prices are from reference ^[149]	

Appendix C

REPRINT PERMISSIONS

Material published by the Royal Society of Chemistry and other publishers is subject to all applicable copyright, database protection, and other rights. Therefore, for any publication, whether printed or electronic, permission must be obtained to use material for which the author(s) does not already own the copyright. This material may be, for example, a figure, diagram, table, photo or some other image.

Author reusing their own work published by the Royal Society of Chemistry

You do not need to request permission to reuse your own figures, diagrams, etc, that were originally published in a Royal Society of Chemistry publication. However, permission should be requested for use of the whole article or chapter except if reusing it in a thesis. If you are including an article or book chapter published by us in your thesis please ensure that your co-authors are aware of this.

Reuse of material that was published originally by the Royal Society of Chemistry must be accompanied by the appropriate acknowledgement of the publication. The form of the acknowledgement is dependent on the journal in which it was published originally, as detailed in 'Acknowledgements'.

The following papers were reproduced in this dissertation by the permission of the Royal Society of Chemistry:

- K. Gong, Q. Fang, S. Gu, S. F. Y. Li, and Y. S. Yan, “Nonaqueous redox-flow batteries: organic solvents, supporting electrolytes and redox pairs”, *Energy & Environmental Science*, 2015, DOI: 10.1039/C5EE02341F

- K. Gong, X. Ma, K. M. Conforti, K. J. Kuttler, J. B. Grunewald, K. L. Yeager, M. Z. Bazant, S. Gu, and Y. S. Yan, “A zinc-iron redox-flow battery under \$100 per kW h of system capital cost”, *Energy & Environmental Science*, **2015**, DOI: 10.1039/C5EE02315G
- S. Gu, K. Gong, E. Z. Yan and Y. S. Yan, “A multiple ion-exchange membrane design for redox flow batteries”, *Energy & Environmental Science*, **2014**, volume 7, issue 9, 2986-2998

ELSEVIER LICENSE TERMS AND CONDITIONS

Jan 22, 2016

This is a License Agreement between Ke Gong ("You") and Elsevier ("Elsevier") provided by Copyright Clearance Center ("CCC"). The license consists of your order details, the terms and conditions provided by Elsevier, and the payment terms and conditions.

All payments must be made in full to CCC. For payment instructions, please see information listed at the bottom of this form.

Supplier	Elsevier Limited The Boulevard, Langford Lane Kidlington, Oxford, OX5 1GB, UK
Registered Company Number	1982084
Customer name	Ke Gong
Customer address	221 Academy St NEWARK, DE 19711
License number	3794360803702
License date	Jan 22, 2016
Licensed content publisher	Elsevier
Licensed content publication	Journal of Power Sources
Licensed content title	Cost and performance model for redox flow batteries
Licensed content author	Vilayanur Viswanathan, Alasdair Crawford, David Stephenson, Soowhan Kim, Wei Wang, Bin Li, Greg Coffey, Ed Thomsen, Gordon Graff, Patrick Balducci, Michael Kintner-Meyer, Vincent Sprenkle
Licensed content date	1 February 2014
Licensed content volume number	247
Licensed content issue number	n/a
Number of pages	12
Start Page	1040
End Page	1051

Type of Use	reuse in a thesis/dissertation
Portion	figures/tables/illustrations
Number of figures/tables/illustrations	3
Format	both print and electronic
Are you the author of this Elsevier article?	No
Will you be translating?	No
Title of your thesis/dissertation	Study of novel redox flow batteries based on double-membrane, single-membrane, and membrane-less cell configurations
Expected completion date	Jan 2016
Estimated size (number of pages)	148
Elsevier VAT number	GB 494 6272 12
Permissions price	0.00 USD
VAT/Local Sales Tax	0.00 USD / 0.00 GBP
Total	0.00 USD
Terms and Conditions	

INTRODUCTION

1. The publisher for this copyrighted material is Elsevier. By clicking "accept" in connection with completing this licensing transaction, you agree that the following terms and conditions apply to this transaction (along with the Billing and Payment terms and conditions established by Copyright Clearance Center, Inc. ("CCC"), at the time that you opened your Rightslink account and that are available at any time at <http://myaccount.copyright.com>).

GENERAL TERMS

2. Elsevier hereby grants you permission to reproduce the aforementioned material subject to the terms and conditions indicated.
3. Acknowledgement: If any part of the material to be used (for example, figures) has appeared in our publication with credit or acknowledgement to another source, permission must also be sought from that source. If such permission is not obtained then that material may not be included in your publication/copies. Suitable acknowledgement to the source must be made, either as a footnote or in a reference list at the end of your publication, as follows:
 "Reprinted from Publication title, Vol /edition number, Author(s), Title of article / title of chapter, Pages No., Copyright (Year), with permission from Elsevier [OR APPLICABLE SOCIETY COPYRIGHT OWNER]."

Also Lancet special credit - "Reprinted from The Lancet, Vol. number, Author(s), Title of article, Pages No., Copyright (Year), with permission from Elsevier."

4. Reproduction of this material is confined to the purpose and/or media for which permission is hereby given.

5. Altering/Modifying Material: Not Permitted. However figures and illustrations may be altered/adapted minimally to serve your work. Any other abbreviations, additions, deletions and/or any other alterations shall be made only with prior written authorization of Elsevier Ltd. (Please contact Elsevier at permissions@elsevier.com)

6. If the permission fee for the requested use of our material is waived in this instance, please be advised that your future requests for Elsevier materials may attract a fee.

7. Reservation of Rights: Publisher reserves all rights not specifically granted in the combination of (i) the license details provided by you and accepted in the course of this licensing transaction, (ii) these terms and conditions and (iii) CCC's Billing and Payment terms and conditions.

8. License Contingent Upon Payment: While you may exercise the rights licensed immediately upon issuance of the license at the end of the licensing process for the transaction, provided that you have disclosed complete and accurate details of your proposed use, no license is finally effective unless and until full payment is received from you (either by publisher or by CCC) as provided in CCC's Billing and Payment terms and conditions. If full payment is not received on a timely basis, then any license preliminarily granted shall be deemed automatically revoked and shall be void as if never granted. Further, in the event that you breach any of these terms and conditions or any of CCC's Billing and Payment terms and conditions, the license is automatically revoked and shall be void as if never granted. Use of materials as described in a revoked license, as well as any use of the materials beyond the scope of an unrevoked license, may constitute copyright infringement and publisher reserves the right to take any and all action to protect its copyright in the materials.

9. Warranties: Publisher makes no representations or warranties with respect to the licensed material.

10. Indemnity: You hereby indemnify and agree to hold harmless publisher and CCC, and their respective officers, directors, employees and agents, from and against any and all claims arising out of your use of the licensed material other than as specifically authorized pursuant to this license.

11. No Transfer of License: This license is personal to you and may not be sublicensed, assigned, or transferred by you to any other person

without publisher's written permission.

12. **No Amendment Except in Writing:** This license may not be amended except in a writing signed by both parties (or, in the case of publisher, by CCC on publisher's behalf).

13. **Objection to Contrary Terms:** Publisher hereby objects to any terms contained in any purchase order, acknowledgment, check endorsement or other writing prepared by you, which terms are inconsistent with these terms and conditions or CCC's Billing and Payment terms and conditions. These terms and conditions, together with CCC's Billing and Payment terms and conditions (which are incorporated herein), comprise the entire agreement between you and publisher (and CCC) concerning this licensing transaction. In the event of any conflict between your obligations established by these terms and conditions and those established by CCC's Billing and Payment terms and conditions, these terms and conditions shall control.

14. **Revocation:** Elsevier or Copyright Clearance Center may deny the permissions described in this License at their sole discretion, for any reason or no reason, with a full refund payable to you. Notice of such denial will be made using the contact information provided by you. Failure to receive such notice will not alter or invalidate the denial. In no event will Elsevier or Copyright Clearance Center be responsible or liable for any costs, expenses or damage incurred by you as a result of a denial of your permission request, other than a refund of the amount(s) paid by you to Elsevier and/or Copyright Clearance Center for denied permissions.

LIMITED LICENSE

The following terms and conditions apply only to specific license types:

15. **Translation:** This permission is granted for non-exclusive world **English** rights only unless your license was granted for translation rights. If you licensed translation rights you may only translate this content into the languages you requested. A professional translator must perform all translations and reproduce the content word for word preserving the integrity of the article.

16. **Posting licensed content on any Website:** The following terms and conditions apply as follows: Licensing material from an Elsevier journal: All content posted to the web site must maintain the copyright information line on the bottom of each image; A hyper-text must be included to the Homepage of the journal from which you are licensing at <http://www.sciencedirect.com/science/journal/xxxxx> or the Elsevier homepage for books at <http://www.elsevier.com>; Central Storage: This license does not include permission for a scanned version of the material to be stored in a central repository such as that provided by

Heron/XanEdu.

Licensing material from an Elsevier book: A hyper-text link must be included to the Elsevier homepage at <http://www.elsevier.com>. All content posted to the web site must maintain the copyright information line on the bottom of each image.

Posting licensed content on Electronic reserve: In addition to the above the following clauses are applicable: The web site must be password-protected and made available only to bona fide students registered on a relevant course. This permission is granted for 1 year only. You may obtain a new license for future website posting.

17. For journal authors: the following clauses are applicable in addition to the above:

Preprints:

A preprint is an author's own write-up of research results and analysis, it has not been peer-reviewed, nor has it had any other value added to it by a publisher (such as formatting, copyright, technical enhancement etc.). Authors can share their preprints anywhere at any time. Preprints should not be added to or enhanced in any way in order to appear more like, or to substitute for, the final versions of articles however authors can update their preprints on arXiv or RePEc with their Accepted Author Manuscript (see below).

If accepted for publication, we encourage authors to link from the preprint to their formal publication via its DOI. Millions of researchers have access to the formal publications on ScienceDirect, and so links will help users to find, access, cite and use the best available version. Please note that Cell Press, The Lancet and some society-owned have different preprint policies. Information on these policies is available on the journal homepage.

Accepted Author Manuscripts: An accepted author manuscript is the manuscript of an article that has been accepted for publication and which typically includes author-incorporated changes suggested during submission, peer review and editor-author communications.

Authors can share their accepted author manuscript:

- – immediately
 - via their non-commercial person homepage or blog
 - by updating a preprint in arXiv or RePEc with the accepted manuscript
 - via their research institute or institutional repository for internal institutional uses or as part of an invitation-only research collaboration work-

- group
 - directly by providing copies to their students or to research collaborators for their personal use
 - for private scholarly sharing as part of an invitation-only work group on commercial sites with which Elsevier has an agreement
- – after the embargo period
 - via non-commercial hosting platforms such as their institutional repository
 - via commercial sites with which Elsevier has an agreement

In all cases accepted manuscripts should:

- – link to the formal publication via its DOI
- – bear a CC-BY-NC-ND license - this is easy to do
- – if aggregated with other manuscripts, for example in a repository or other site, be shared in alignment with our hosting policy not be added to or enhanced in any way to appear more like, or to substitute for, the published journal article.

Published journal article (JPA): A published journal article (PJA) is the definitive final record of published research that appears or will appear in the journal and embodies all value-adding publishing activities including peer review co-ordination, copy-editing, formatting, (if relevant) pagination and online enrichment.

Policies for sharing publishing journal articles differ for subscription and gold open access articles:

Subscription Articles: If you are an author, please share a link to your article rather than the full-text. Millions of researchers have access to the formal publications on ScienceDirect, and so links will help your users to find, access, cite, and use the best available version.

Theses and dissertations which contain embedded PJAs as part of the formal submission can be posted publicly by the awarding institution with DOI links back to the formal publications on ScienceDirect.

If you are affiliated with a library that subscribes to ScienceDirect you have additional private sharing rights for others' research accessed under that agreement. This includes use for classroom teaching and internal training at the institution (including use in course packs and courseware programs), and inclusion of the article for grant funding purposes.

Gold Open Access Articles: May be shared according to the author-selected end-user license and should contain a [CrossMark logo](#), the end user license, and a DOI link to the formal publication on ScienceDirect.

Please refer to Elsevier's [posting policy](#) for further information.

18. **For book authors** the following clauses are applicable in addition to

the above: Authors are permitted to place a brief summary of their work online only. You are not allowed to download and post the published electronic version of your chapter, nor may you scan the printed edition to create an electronic version. **Posting to a repository:** Authors are permitted to post a summary of their chapter only in their institution's repository.

19. **Thesis/Dissertation:** If your license is for use in a thesis/dissertation your thesis may be submitted to your institution in either print or electronic form. Should your thesis be published commercially, please reapply for permission. These requirements include permission for the Library and Archives of Canada to supply single copies, on demand, of the complete thesis and include permission for Proquest/UMI to supply single copies, on demand, of the complete thesis. Should your thesis be published commercially, please reapply for permission. Theses and dissertations which contain embedded PJAs as part of the formal submission can be posted publicly by the awarding institution with DOI links back to the formal publications on ScienceDirect.

Elsevier Open Access Terms and Conditions

You can publish open access with Elsevier in hundreds of open access journals or in nearly 2000 established subscription journals that support open access publishing. Permitted third party re-use of these open access articles is defined by the author's choice of Creative Commons user license. See our [open access license policy](#) for more information.

Terms & Conditions applicable to all Open Access articles published with Elsevier:

Any reuse of the article must not represent the author as endorsing the adaptation of the article nor should the article be modified in such a way as to damage the author's honour or reputation. If any changes have been made, such changes must be clearly indicated.

The author(s) must be appropriately credited and we ask that you include the end user license and a DOI link to the formal publication on ScienceDirect.

If any part of the material to be used (for example, figures) has appeared in our publication with credit or acknowledgement to another source it is the responsibility of the user to ensure their reuse complies with the terms and conditions determined by the rights holder.

Additional Terms & Conditions applicable to each Creative Commons user license:

CC BY: The CC-BY license allows users to copy, to create extracts, abstracts and new works from the Article, to alter and revise the Article and to make commercial use of the Article (including reuse and/or resale

of the Article by commercial entities), provided the user gives appropriate credit (with a link to the formal publication through the relevant DOI), provides a link to the license, indicates if changes were made and the licensor is not represented as endorsing the use made of the work. The full details of the license are available at <http://creativecommons.org/licenses/by/4.0>.

CC BY NC SA: The CC BY-NC-SA license allows users to copy, to create extracts, abstracts and new works from the Article, to alter and revise the Article, provided this is not done for commercial purposes, and that the user gives appropriate credit (with a link to the formal publication through the relevant DOI), provides a link to the license, indicates if changes were made and the licensor is not represented as endorsing the use made of the work. Further, any new works must be made available on the same conditions. The full details of the license are available at <http://creativecommons.org/licenses/by-nc-sa/4.0>.

CC BY NC ND: The CC BY-NC-ND license allows users to copy and distribute the Article, provided this is not done for commercial purposes and further does not permit distribution of the Article if it is changed or edited in any way, and provided the user gives appropriate credit (with a link to the formal publication through the relevant DOI), provides a link to the license, and that the licensor is not represented as endorsing the use made of the work. The full details of the license are available at <http://creativecommons.org/licenses/by-nc-nd/4.0>. Any commercial reuse of Open Access articles published with a CC BY NC SA or CC BY NC ND license requires permission from Elsevier and will be subject to a fee.

Commercial reuse includes:

- – Associating advertising with the full text of the Article
- – Charging fees for document delivery or access
- – Article aggregation
- – Systematic distribution via e-mail lists or share buttons

Posting or linking by commercial companies for use by customers of those companies.

20. Other Conditions:

v1.8

Questions? customer@copyright.com or +1-855-239-3415 (toll free in the US) or +1-978-646-2777.